Diss. ETH No. 24558

LATTICE BOLTZMANN SIMULATIONS OF FLUID-SOLID MOMENTUM AND HEAT TRANSFER IN GAS-SOLID FLOWS COMPRISING CUBIC PARTICLES

A thesis submitted to attain the degree of

DOCTOR OF SCIENCES OF ETH ZURICH
(Dr. sc. ETH Zurich)

Presented by
YONG CHEN
M.Eng. in Fluid Mechanics, Zhejiang University, China

Born on 17.07.1985
Citizen of P. R. China

accepted on the recommendation of

Prof. Christoph Müller, examiner

Prof. Antonio Acosta-Iborra, co-examiner

Dr. Christopher Boyce, co-examiner

2017

Dedicated in memory of my father

Abstract

Gas-solid systems comprising non-spherical particles are frequently encountered in industry and are the basis of various reactor concepts, e.g. gas-fluidized and packed beds or rotary kilns. However, our fundamental understanding of these systems is still rather limited which is, at least partially, due to the very complex particle-fluid interactions. Thus, an improved understanding of particle-fluid interactions (i.e. momentum, heat and mass transfer) is essential to predict more accurately the dynamics of these systems.

In this work, cubic particles are represented using two different approaches: (1) Construction from individual, identical spheres; (2) Representation by a continuous function, i.e. the super-quadric equation.

Firstly, we developed a drag force correlation for assemblies of approximately cubic particles that were constructed from eight identical spheres for $\mathrm{Re} \leq 200$ and $\phi \leq 0.45$. A comparison with drag force correlations proposed for assemblies of spheres (derived also numerically) demonstrated that the drag force acting on assemblies of approximately cubic particles is much larger than that acting on assemblies of equal volume spheres. Subsequently, the method was extended to determine the drag force acting on assemblies of super-quadric cubes. The simulation data were compared with empirical (experimentally derived) and numerically derived correlations. It was shown that a general empirical drag force correlation for assemblies of non-spherical particles or a drag force correlation derived from a coarse level representation of non-spherical particles (e.g. constructed by several identical spheres) is currently associated with a large error. Hence, a drag force correlation for assemblies of super-quadric cubes was proposed based on the simulation data.

In addition to correlations for the drag force acting on cubic particles, the heat transfer in assemblies of spheres and super-quadric cubes was studied using a thermal lattice Boltzmann method. To model the heat transfer between the gas and the particles, a Dirichlet boundary condition to impose a constant temperature at the surface of the particle was proposed for the thermal lattice Boltzmann method. The thermal lattice Boltzmann method was used subsequently to compute the average Nusselt number for assemblies of spheres for $\mathrm{Re} \leq 100$ and $\phi \leq 0.5$. Based on the simulation data, a new Nusselt number correlation was proposed which was obtained from thermally fully-developed flows. Subsequently, the fluid-particle heat transfer in random assemblies of super-quadric cubes was calculated for $\phi \leq 0.45$. Defining the Reynolds number based on the hydraulic diameter of the packing (Re_h), the newly proposed Nusselt number correlation for assemblies of spheres was transformed into a modified form that is a function of Re_h. The new Nusselt number correlation was shown to be able to predict the Nusselt number for assemblies of super-quadric cubes if the Sauter diameter was chosen as the characteristic size of the cube. The new drag force and Nusselt number correlations proposed in this work are expected to improve the accuracy of Euler-Euler and Euler-Lagrangian simulations of non-isothermal flows comprising cubic particles.

Zusammenfassung

In der Industrie finden man häufig Gas-Feststoff-Systeme vor, die aus nicht-kugelförmigen Teilchen bestehen und wesentlicher Bestandteil verschiedener Reaktorkonzepte sind, z.B. Wirbelschichten, Festbettreaktoren und Drehrohröfen. Unser grundlegendes Verständnis solcher Systeme ist nach wie vor recht begrenzt, was zumindest teilweise auf die sehr komplexen Wechselwirkungen von Partikeln und Fluid zurückzuführen ist. Ein verbessertes Verständnis der Partikel-Fluid-Wechselwirkungen (sprich, Impuls, Wärme- und Stofftransport) ist deshalb zwingend erforderlich um die Dynamiken solcher Systeme besser voraussagen zu können.

In dieser Dissertation werden nicht-kugelförmige Partikel (z.B. kubische Partikel) durch zwei unterschiedliche Ansätze modelliert: (1) Zusammensetzung aus individuellen, identischen Kugeln; (2) Darstellung durch eine kontinuierliche Funktion, die Super-Quadrik Gleichung.

In dieser Arbeit wird zuerst eine Korrelation für die Widerstandskraft von Gruppen von annähernd kubischen Teilchen, die sich aus acht identischen Kugeln zusammensetzen, für den Bereich $Re \leq 200$ und $\phi \leq 0.45$ entwickelt. Beim Vergleich mit Widerstandskraftkorrelationen für Gruppen bestehend aus Kugeln (ebenfalls numerisch bestimmt) konnte gezeigt werden, dass die Widerstandskraft, die auf Gruppen annähernd kubischer Partikeln wirkt, viel grösser ist als die Widerstandskraft die auf Gruppen bestehend aus Kugeln gleichen Volumens wirkt. Die Methode wurde danach erweitert um die Widerstandskraft, die auf Gruppen von Super-Quadrik Würfeln wirkt, zu bestimmen. Die Ergebnisse der Computersimulationen wurden mit Korrelationen verglichen, die empirisch (in Experimenten bestimmt) und numerisch hergeleitet wurden. Es konnte aufgezeigt werden, dass eine allgemeine empirische Widerstandskraftkorrelation für Gruppen nicht-kugelförmiger Partikel und eine Widerstandskraftkorrelation, die aus einer groben Abbildung nicht-kugelförmiger Partikeln (z.B. zusammengestellt aus einer Vielzahl identischer Kugeln) abgeleitet wurde, derzeit mit einer grossen Ungenauigkeit behaftet ist. Auf Grundlage der Ergebnisse der Computersimulationen wurde deshalb vorgeschlagen, eine Widerstandskraftkorrelation für Gruppen von Super-Quadrik Würfeln zu verwenden.

Zusätzlich zu den Korrelationen für die Widerstandskraft, die auf nicht-kugelförmige Partikeln wirkt, wurde der Wärmetransport in Gruppen von Kugeln und Super-Quadrik Würfeln mittels einer thermischen Lattice-Boltzmann-Methode untersucht. Um den Wärmetransport zwischen Gas und Partikeln zu modellieren, wurde eine Dirichlet Randbedingung für die thermische Lattice-Boltzmann-Methode vorgeschlagen, um die Temperatur auf der Oberfläche des Partikels konstant zu halten. Die thermische Lattice-Boltzmann-Methode wurde anschliessend verwendet um die durchschnittliche Nusselt-Zahl für Gruppen von Kugeln für den Bereich $Re \leq 100$ und $\phi \leq 0.5$ zu berechnen. Auf Grundlage der Ergebnisse der Simulationen für thermisch vollständig entwickelte Strömungen wurde eine neue Korrelation für die Nusselt-Zahl entwickelt. Für $\phi \leq 0.45$ wurde daraufhin der Fluid-Partikel Wärmetransport von zufälligen Gruppen von Super-Quadrik

Würfeln berechnet. Die neue Korrelation für die Nusselt-Zahl wurde in eine modifizierte Form überführt, so dass sie als Funktion von Re_h, der Reynolds-Zahl basierend auf dem hydraulischen Durchmesser der Packung der Gruppe von Super-Quadrik Würfeln, dargestellt werden kann. Es wurde gezeigt, dass die neue Korrelation die Nusselt-Zahl für Gruppen bestehend aus Super-Quadrik Würfeln genau vorhersagen kann, wenn der Sauterdurchmesser als charakteristische Grösse der Würfel verwendet wird. Es ist davon auszugehen, dass die neuen Korrelationen für die Widerstandskraft und Nusselt-Zahl, die in dieser Dissertation bestimmt wurden, die Genauigkeit von Simulationen von nicht-isothermische Strömungen welche auf Euler-Euler oder Euler-Lagrange Modellen basieren erheblich verbessern werden.

Nomenclature

V	volume of the computational domain
∇P	pressure gradient cross the volume V
$\vec{F}_{tot}$	total average fluid particle interaction force
$\vec{F}'_{tot}$	total fluid particle interaction force acting on a particle
N	number of particles in the volume V
$\vec{F}'_d$	average drag force acting on a particle
F_d	normalized average drag force acting on a particle
d_p	diameter of the sphere
$\vec{U}, \vec{u}_s$	superficial velocity
$\vec{u}_p$	particle velocity
Re	Reynolds number
Re_V	Reynolds number based on volume equivalent diameter
Re_h	Reynolds number based on Sauter diameter
d_V	volume equivalent sphere diameter
d_A	projected area equivalent sphere diameter
d_N	surface area equivalent sphere diameter
d_h	hydraulic diameter
d_s	Sauter diameter
V_p	volume of the particle
A_p	projected area of the particle in its direction of motion
P_p	projected perimeter of the particle in its direction of motion
c_r	circularity of the particle
c_d	drag coefficient
f_i	discrete density distribution function
f_i^{eq}	discrete equilibrium density distribution function
g_i	discrete energy distribution function
g_i^{eq}	discrete equilibrium energy distribution function
$\vec{e}_i$	lattice direction vector
c	lattice constant
Δx	physical length between two neighbouring lattice nodes
Δt	physical time corresponding to each time step
t	physical time
$\vec{x}$	physical coordinates of the lattice node
$\vec{u}_f$	velocity of fluid in lattice unit
w_i	weighting factor for equilibrium distribution

B_v, B_c weighting function
r_h hydraulic radius
Nu Nusselt number for spherical particle
Nu_V Nusselt number based on particle volume equivalent diameter of the cube
Nu_s Nusselt number based on particle Sauter diameter of the cube
Pr Prandtl number
D thermal diffusivity of the fluid
c_{pf} specific heat capacity
k_f thermal conductivity of the fluid
T_f fluid temperature
h heat transfer coefficient
$\dot{q}_i$ particle heat transfer rate

$\bar{T}_f$ average fluid temperature around a particle

T_s particle temperature
$\vec{n}$ unit vector in the normal direction of the particle surface
L the size of the computational domain

Greek letters

ϕ solid volume fraction
μ_f dynamic viscosity
Φ sphericity
$\Phi_\parallel$ lengthwise sphericity
$\Phi_\perp$ crosswise sphericity
ρ_f fluid density
τ_v, τ_c relaxation time
ν kinematic viscosity

$\Omega_{i,v}^p, \Omega_{i,c}^p$ additional collision term

α form-drag coefficient
φ energy of the fluid
ϕ_x local solid volume fraction of a lattice that is covered by the solid particles
ε bed voidage
φ_s particle temperature

Abbreviations

CFD   computational fluid dynamics
DEM   discrete element method
TFM   two-fluid model
LBM   lattice Boltzmann method
IBM   immersed boundary method

LBE   lattice Boltzmann equation
DNS   direct numerical simulation

Content

1 General Introduction

1.1 Introduction

Gas-solid, non-isothermal flows are encountered frequently in industry, e.g. gas-fluidized and packed bed reactors. In particular gas-fluidized beds have attracted significant attention due to their favourable characteristics which include rapid mixing, fairly uniform temperature distribution and good gas-solid contacting. However, despite their wide-spread use in industry, the fundamentals of fluidized beds e.g. the formation of bubbles at orifices or the coalescence and splitting of bubbles, are still only poorly understood. Hence, improving our understanding of the complicated interaction between fluid mechanical and thermal effects is essential to improve further their design and, hence, improve their efficiency. Over the past decades, computational fluid dynamics (CFD) has been applied extensively to compute the fluid flow, heat transfer and chemical reactions in gas-fluidized beds. However, in gas-fluidized systems the flow structure spans over a wide range of length scales, e.g. from (sub-) millimeter (particle level) to (sub-) meter (large bubbles or slugs). In this context, a multiscale modeling strategy was proposed by van der Hoef et al. (2008). At the most detailed level, direct numerical simulations (DNS) fully resolve the fluid flow around individual particles by imposing appropriate boundary conditions on the particle surface. Such a modelling approach allows for example the momentum and heat transfer between the fluid and particles to be calculated directly (and accurately). Additionally, DNS simulation data can be used to derive closure relationships such as a drag force correlation and heat transfer coefficient that are required for less-resolved modelling approaches such as computational fluid dynamics coupled to a discrete element method (CFD-DEM) or the two-fluid model (TFM). However, due to the requirement of a very fine discretization of the domain in DNS, a routine simulation of say laboratory scale gas-fluidized beds is currently out of reach. This gap is closed by higher-level modelling approaches such as CFD-DEM or the two-fluid model. In CFD-DEM, the particles are tracked individually and the fluid is modelled using the volume averaged Navier-Stokes equation that are solved on a comparatively large grid size, typically about three times the particle diameter. The fluid particle interaction(s) can be modeled using experimentally or numerically derived closure relationships (e.g. drag force correlation). The particle-particle and particle-wall interactions are described by appropriate models for the contact mechanics (typically a soft sphere approach is considered). Similar as for the DNS model, the CFD-DEM simulations can be used to derive closures required to describe particle-particle interactions in the two fluid model (e.g. particle energy loss due to collisions). The two-fluid model requires a series of closure relationships to describe appropriately the particle-particle (Lun et al, 1984) and particle-fluid (e.g. Gidaspow, 1994) interactions. At the current state, only the two-fluid model is applicable to simulate industrial-sized gas-fluidized beds.

Turning to closure relationships, currently empirical correlations (experimentally derived) for the momentum and heat transfer are implemented in the numerical models described above (Ergun, 1952; Wen & Yu, 1966; Gunn, 1978; Wakao et al., 1979). However, it is under debate whether these correlations can be used for the wide range of solid volume fractions that are typically encountered in gas fluidized beds (Gidaspow, 1994). For example, Tavassoli (2014) argued that the commonly applied Nusselt number correlation of Gunn (1978) is valid only for solid volume fractions $\phi < 0.3$. Due to the inherent difficulty to perform temporally and spatially resolved experiments in gas-solid systems (Müller et al., 2006; Holland et al., 2008; Müller et al., 2011), direct numerical simulations (DNS) have been employed to improve the accuracy (and the parameter space) of drag force and Nusselt number correlations (e.g. Hill et al., 2001b; Beetstra et al., 2007; Tavassoli et al., 2015; Sun et al., 2015).

It is worth noting that the correlations listed above have been developed for spherical particles. Indeed, very few efforts have been reported for developing drag force and Nusselt number correlations for assemblies of non-spherical particles. Hilton et al. (2010) modified Di Felice's drag force correlation (1994) (originally derived for assemblies of spheres) by simply replacing the drag coefficient correlation for individual spheres with the drag coefficient correlation for single non-spherical particles (Hölzer et al., 2008). The correlation proposed by Hilton et al. (2010) has been employed to simulate a gas-fluidized bed containing non-spherical particles (e.g. cubes, spheroids). The particles used in these simulations (e.g. Hilton et al., 2010) were represented by the super-quadric equation. The advantage of the super-quadric equation is that the surface normal of the particle can be computed readily (Lu et al., 2015). A different approach to model non-spherical particles was followed by Zhong et al. (2009) who simulated a 3D gas-fluidized bed containing cylindrical particles that were constructed from identical spheres using CFD-DEM. The fluid-particle drag force was calculated using the drag force correlation proposed by Tran-Cong et al. (2004), originally derived for a single, non-spherical particle. Zhong et al. (2009) reported that the simulation results agreed well with the experimental data of gas-fluidized beds containing cylindrical particles. Ren et al. (2011) proposed a drag force correlation for single cylindrical particles by measuring their settling velocity in a uniform gas flow. The correlation developed was used subsequently (Ren et al., 2014) to model a spouted bed of cylindrical particles that were constructed from identical spheres. When compared to experimental measurements, the CFD-DEM simulations were found to predict the pressure drop well at different bed positions.

The simulation of heat transfer in gas-solid flows containing non-spherical particles has been studied so far rather sparsely. In one of the few reports, Richter and Nikrityuk (2012) calculated the Nusselt number for single non-spherical particles in uniform flows (e.g. cubes, spheroids) and proposed a Nusselt number correlation which takes into account particle shape (i.e. sphericity) and orientation (crosswise sphericity, i.e. the ratio of the projected area of the particle to the cross section area of

the volume equivalent sphere). Yang et al. (2010) calculated the Nusselt number for ordered packings of ellipsoids (face centred cubic packings of ellipsoids) and proposed a Nusselt number correlation by modifying the equation of Wakao (Wakao et al., 1979). Tavassoli et al. (2015) simulated the heat transfer between the fluid and particles in an assembly of equal-sized spherocylinders for $Re \leq 100$ and $\phi \leq 0.6$. It was reported that the Nusselt number correlation proposed by Tavassoli et al. (2015) for assemblies of spheres can be applied to predict the Nusselt number for spherocylinders if the diameter of the spherocylinder was chosen as the characteristic size of the particle.

Considering the lack of suitable drag force and Nusselt number correlations for assemblies of non-spherical particles, we model here the fluid flow over assemblies of cubes using a lattice Boltzmann method as a DNS technique. These simulations are used subsequently to develop drag force and Nusselt number correlations that are applicable for Euler-Euler and Euler-Lagrangian simulations. The cubic particles are represented using two different approaches: (1) constructed from eight identical spheres (Figure 1.1(a)) and (2) continuous function representation, i.e. the super-quadric equation (Figure 1.1(b)).

(a)   (b)
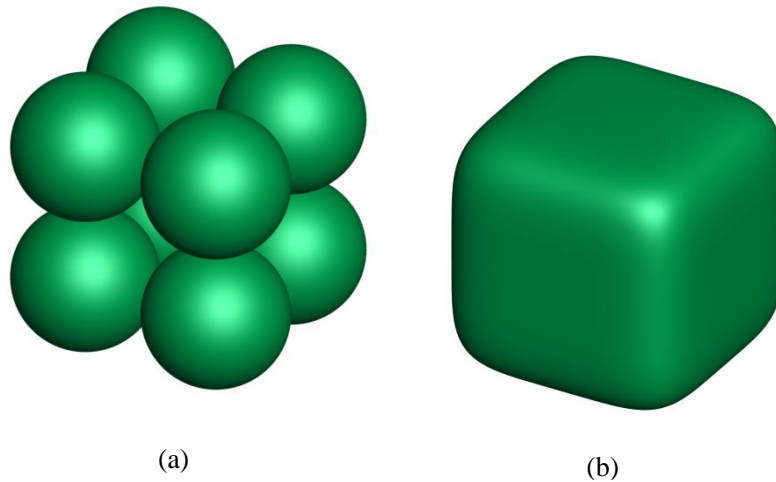
Figure 1.1. Different representations of cubic particles: (a) a cube constructed from eight identical spheres; (b) super-quadric cube.

Turning now to different discretization/modelling approaches, the lattice Boltzmann method provides an interesting alternative to conventional approaches (e.g. finite volume solver) to solve the Navier-Stokes equation to model fluid flow. When compared to "conventional" approaches , the lattice Boltzmann method has several advantages: (1) the convective and collisional operators are linear; (2) the fluid pressure can be calculated simply by an equation of state; (3) complex boundaries are relatively easy to implement and (4) ease of parallelization as computations are local (Chen & Doolen, 1998). The thermal lattice Boltzmann equations for the momentum and energy equations are as follows:

$$f_i(\vec{x}+\vec{e}_i\Delta t, t+\Delta t) = f_i(\vec{x},t) - \frac{\Delta t}{\tau_v}[f_i(\vec{x},t) - f_i^{eq}(\vec{x},t)] \tag{1.1}$$

$$g_i(x+\vec{e}_i\Delta t, t+\Delta t) = g_i(x,t) - \frac{\Delta t}{\tau_c}[g_i(x,t) - g_i^{eq}(x,t)] \tag{1.2}$$

Where f_i, g_i are the density and energy distribution functions at position $\vec{x}$ and time t with velocity $\vec{e}_i$. The superscript 'eq' denotes the equilibrium state, τ_v and τ_c are the single relaxation times related to the viscosity and thermal diffusivity, respectively and Δt is the time step applied. The numerical implementation of the thermal lattice Boltzmann equation involves two steps:

1. Collision

$$f_i^{'}(\vec{x},t) = f_i(\vec{x},t) - \frac{\Delta t}{\tau_v}[f_i(\vec{x},t) - f_i^{eq}(\vec{x},t)] \tag{1.3}$$

$$g_i^{'}(x,t) = g_i(x,t) - \frac{\Delta t}{\tau_c}[g_i(x,t) - g_i^{eq}(x,t)] \tag{1.4}$$

2. Streaming

$$f_i(\vec{x}+\vec{e}_i\Delta t, t+\Delta t) = f_i^{'}(\vec{x},t) \tag{1.5}$$

$$g_i(x+\vec{e}_i\Delta t, t+\Delta t) = g_i^{'}(x,t) \tag{1.6}$$

The D3Q19 and D3Q7 lattice (Figure 1.2) for the density and energy distributions are given as follows:

$$\vec{e}_i = \begin{cases} (0,0,0), & i=0 \\ (\pm1,0,0)c, (0,\pm1,0)c, (0,0,\pm1)c, & i=1...6 \\ (\pm1,\pm1,0)c, (\pm1,0,\pm1)c, (0,\pm1,\pm1)c, & i=7...18 \end{cases} \tag{1.7}$$

with c being the ratio of Δx and Δt. The discrete equilibrium density function is expressed as:

$$f_i^{eq} = w_{i,v}\rho_f[1+3\frac{\vec{e}_i\cdot\vec{u}_f}{c^2} + \frac{9}{2}\frac{(\vec{e}_i\cdot\vec{u}_f)^2}{c^4} - \frac{3}{2}\frac{\vec{u}_f^2}{c^2}]$$

$$w_{i,v} = \begin{cases} \dfrac{1}{3}, & i=0 \\ \dfrac{1}{18}, & i=1...6 \\ \dfrac{1}{36}, & i=7...18 \end{cases} \tag{1.8}$$

where ρ_f and $\vec{u}_f$ are the fluid density and velocity. The discrete energy distribution function is

4

$$g_i^{eq} = w_{i,c}\varphi(1 + 4 \cdot \frac{\vec{e}_i \cdot \vec{u}_f}{c^2})$$

$$w_{i,c} = \begin{cases} \dfrac{1}{4}, & i = 0 \\ \dfrac{1}{8}, & i = 1...6 \end{cases} \tag{1.9}$$

(a)

(b)
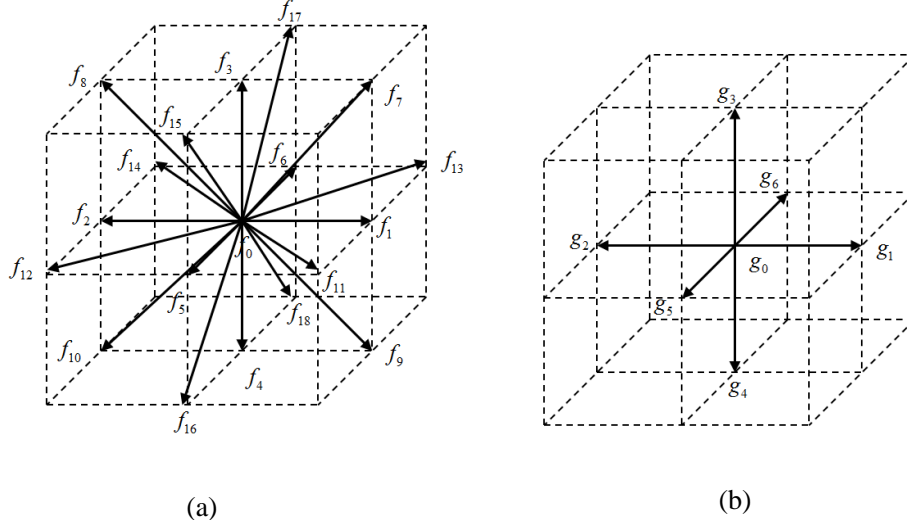
Figure 1.2. Lattice structures for the (a) D3Q19 and (b) D3Q7 lattices

The density, momentum and energy of the fluid can be calculated as:

$$\rho_f = \sum_i f_i, \quad \rho_f \vec{u}_f = \sum_i f_i \vec{e}_i, \quad \varphi = \sum_i g_i \tag{1.10}$$

The kinematical viscosity and thermal diffusivity of the fluid are calculated as:

$$v = \frac{1}{3}c^2(\tau_v - \frac{\Delta t}{2})$$

$$D = \frac{1}{4}c^2(\tau_c - \frac{\Delta t}{2}) \tag{1.11}$$

The lattice Boltzmann method has been used extensively to model isothermal (Ladd, 1994; Aidun et al., 1998; Beetstra et al., 2007; Third et al., 2016) and thermal flows (Yoshida & Nagaoka, 2010; Li et al., 2013; Wang et al., 2016). As a consequence, various non-slip hydrodynamic boundary conditions (Ladd, 1994; Zou and He, 1997; Noble and Torczynski, 1998; Guo et al., 2002; Feng et al., 2004) and thermal boundary conditions (Ginzburg, 2005; Li et al., 2013; Wang et al., 2016) have been developed. Among these boundary conditions, the half-way bounce back scheme for solid boundaries is the easiest to implement. The density ($f_i(x_f, t + \Delta t)$) and energy

$(g_i(x_f, t + \Delta t))$ distribution functions at fluid nodes x_f are unknown during the streaming step since the distribution functions at the wall nodes x_w are undefined (Figure 1.3). The bounce back scheme for the unknown distributions $f_i(x_f, t + \Delta t)$ (Eq. (1.12), Figure 1.3a) and $g_i(x_f, t + \Delta t)$ (Eq. (1.13), Figure 1.3b) can be described as:

$$f_i(x_f, t + \Delta t) = f_{-i}(x_f, t) + 6\rho_f w_{i,v} \vec{u}_w \vec{e}_i c \tag{1.12}$$

$$g_i(x_f, t + \Delta t) = -g_{-i}(x_f, t) + \frac{1}{4} T_w \tag{1.13}$$

In Eqs. (1.12) and (1.13) $-i$ denotes the opposite direction of i and $\vec{u}_w$ and T_w are the wall velocity and energy (or temperature), respectively. If the wall is located in the middle of a fluid node and a wall node, the half-way bounce back scheme is second order accurate. However, in fluidized beds, curved solid boundaries are encountered often. Therefore, employing more accurate solid boundary conditions is essential to predict accurately the fluid-particle interactions in gas-fluidized beds.
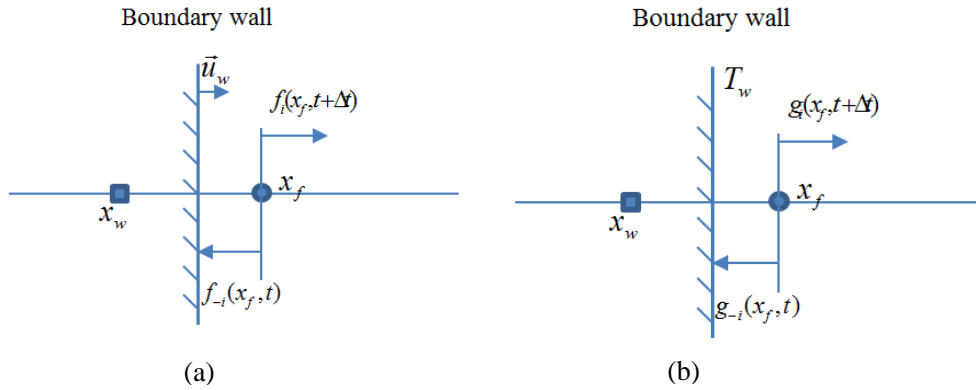
Figure 1.3. Half-way bounce back scheme for (a) non-slip hydrodynamic boundary condition and (b) thermal boundary condition (i.e. Dirichlet boundary condition)

Hence, in this work, a new Dirichlet boundary condition for a thermal lattice Boltzmann method was developed which can be considered as an extension of the non-slip hydrodynamic boundary condition proposed by Noble and Torczynski (1998).

1.2 Outline of the thesis

In chapter 2, the drag force acting on assemblies of approximately cubic particles that were constructed from eight identical spheres is calculated using a lattice Boltzmann method. The results are compared with the predictions of numerically and

experimentally derived correlations for assemblies of spheres. Based on the simulation data, a new drag force correlation for assemblies of approximately cubic particles is presented.

In Chapter 3, a drag force correlation for assemblies of cubes is developed. The cubic particles are represented using the super-quadric equation, a popular approach in DEM simulations. The correlation is compared with drag force correlations for assemblies of non-spherical particles that are available in the literature.

Chapter 4 introduces a Dirichlet boundary condition for the thermal lattice Boltzmann method. Asymptotic analysis of the boundary condition confirms that it is of second order accuracy. The method is then used to simulate heat transfer between the fluid and individual particles. The simulation results are compared with previous direct numerical simulations.

In Chapter 5, the Nusselt number for assemblies of spheres is calculated using a thermal lattice Boltzmann method. The simulation data are compared with experimentally and numerically derived Nusselt number correlations for assemblies of spheres. Based on the simulation data, a new Nusselt number correlation for assemblies of spheres is developed.

Chapter 6 focuses on the use of the thermal lattice Boltzmann method to simulate the heat transfer in an assembly of super-quadric cubes. A Reynolds number that is based on the hydraulic diameter of the packing (Re_h), is hereby used to develop a correlation for the Nusselt number. The new correlation obtained is able to predict the Nusselt number for assemblies of super-quadric cubes if the Sauter diameter of the cubes is chosen as their characteristic length.

Finally, the last Chapter summarizes the results presented in the thesis and provides an outlook for future work.

2

A drag force correlation for approximately cubic particles constructed from identical particles

2.1   Abstract

The lattice Boltzmann method has been used to compute the drag force acting on assemblies of approximately cubic particles constructed from 8 spheres for a wide range of Reynolds numbers. Based on the simulation data we propose a new drag force correlation for assemblies of approximately cubic particles. We have compared the drag force obtained with that predicted by the correlation proposed by Beetstra et al. (2007), originally proposed for spheres, by considering either the drag acting on individual spheres, or the drag acting on an approximately cubic particle composed of 8 spheres. The comparisons showed that Beetstra's correlation cannot predict the system well. The correlation proposed in this paper enables Euler-Euler and Euler-Lagrangian simulations of approximately cubic particles, allowing the influence of the solid volume fraction in these models to be assessed.

2.2   Introduction

Gas-solid systems are of significant industrial importance and are the basis of various reactor concepts, e.g. gas-fluidized and packed beds or rotary kilns. However, with regards to numerical modelling of these systems, very little is known about the force exerted on the individual particles when a fluid flows through an assembly of particles, i.e. the drag force. A good understanding of particle-fluid interactions is essential to predict more accurately the dynamics of these systems. In previous studies, it was found that the pattern formation in gas fluidized beds was significantly affected by the momentum exchange between the gas phase and the solid phase (Li & Kuipers, 2003). A theoretical solution for the drag acting on an isolated sphere in unbounded flow was derived only for the zero Reynolds number limit (Batchelor, 1967). Hinch (1977) calculated the drag force for random assemblies of spheres in dilute limit suspensions by taking into account of the presence of neighboring particles. Kim et al. (1985) extended the work of Hinch (1977), and proposed a drag force correlation for volume fractions up to 0.5, but only the first few terms ($O(\phi^2)$) can be evaluated analytically. For large volume fractions, the drag force can be estimated from the Carman equation (1937). However, the practical value of these theories is rather limited since they are only valid for very low Reynolds numbers. The interaction of particles with a fluid can also be modelled using Stokesian Dynamics (Brady & Bossis, 1998). However, this method is also restricted to low Reynolds numbers. For this reason, empirical correlations obtained from pressure drop measurement or terminal velocities measurement of sedimenting particles for higher Reynolds numbers and volume

fractions are commonly used in engineering practice, i.e. correlations of Ergun (1952) and Wen & Yu (1966). In recent years, drag laws generated from direct numerical simulations have become available. Koch (Koch et al., 1999; Hill et al., 2001a, b) was the first to develop a drag force correlation based on lattice Boltzmann simulations. Van der Hoef and Beetstra (van der Hoef et al., 2004; Beetstra et al., 2007) extended the work of Hill et al. (2001a, b), establishing new drag force correlations for mono- and bi-disperse arrays of spheres. In these simulations the flow field around a random array of spheres was computed using the lattice Boltzmann method with a lattice spacing that was sufficiently small to allow the detailed flow around the spheres to be modelled. Coupled computational fluid dynamics-discrete element method (CFD-DEM) simulations (Bokkers et al., 2004) performed using the drag model proposed by Hill et al. (2001b) showed better agreement with experimental measurements than those performed using the traditional Ergun and Wen & Yu correlations.

In most practical applications of gas-fluidised beds, the particles are not spherical and the drag force is affected by solid volume fraction and particle orientation. Due to a lack of drag force correlations for assemblies of non-spherical particles, numerical simulations of gas-fluidized beds have largely been restricted to beds containing spherical particles. The effect of particle shape on the drag force has been investigated for isolated particles. For example, Tran-Cong et al. (2004) measured the drag force coefficients for isolated non-spherical particles constructed from several identical spheres. Beetstra et al. (2006) performed LBM simulations of individual non-spherical particles constructed from spheres. Excellent agreement was reported between the LBM data and the experimental results given by Tran-Cong et al. (2004). Hölzer et al. (2008), using experimental data and numerical simulations, correlated the drag force acting on single non-spherical particles with particle orientation and Reynolds number. However, these correlations cannot be applied directly to simulate gas-fluidized beds since they do not account for the influence of the solids volume fraction on the drag coefficient. In this paper, we use the lattice Boltzmann method to develop a drag force correlation for an assembly of approximately cubic particles that are constructed from 8 identical spheres, a common approach in the DEM. The approximately cubic particles constructed this way are unbreakable and undeformable. The effect of the solid volume fraction and the Reynolds number on the drag force is studied in detail. The new drag force correlation proposed here is suitable for Euler-Euler and Euler-Lagrangian simulations of gas-fluidized beds comprised of approximately cubic particles.

2.3 Drag force correlations for mono-disperse spheres

The total average fluid-particle interaction force acting on each particle within a volume V is usually expressed as:

$$\vec{F}_{tot} = \frac{-\phi V}{N} \nabla P + \vec{F}_d^{'} \qquad (2.1)$$

where ∇P is the pressure gradient across the volume, ϕ is the solid volume fraction, N is the number of particles in the volume, $\vec{F}_d'$ is the average drag force due to fluid solid friction at the surface of sphere. The total average force $\vec{F}_{tot}$ is determined as $\frac{1}{N}\sum_N \vec{F}_{tot}'$, where $\vec{F}_{tot}'$ is the total force acting on each particle in the computational domain calculated by equation (2.24). From a force balance over volume V, we obtain $-V\nabla P = N\vec{F}_{tot}$. Substituting $-V\nabla P = N\vec{F}_{tot}$ into equation (2.1) gives an expression to calculate $\vec{F}_d'$, with $\vec{F}_d' = (1-\phi)\vec{F}_{tot}$. In this paper, we define F_d ($F_d = \vec{F}_d'/3\pi\mu_f\vec{U}d_p$, $\vec{U}$ is the superficial velocity, d_p is the diameter of the particle, μ_f is the dynamic viscosity) as the normalized drag force, which is the common choice in chemical engineering (Di Felice, 1995).

Ergun (1952) derived a correlation from pressure drop measurements for a packed bed:

$$F_d = \frac{150}{18}\frac{\phi}{(1-\phi)^2} + \frac{1.75}{18}\frac{\text{Re}}{(1-\phi)^2} \tag{2.2}$$

It should be noted that Ergun carried out the experiment with a small range of porosities (0.43-0.54), therefore, the correlation is typically valid for low porosity systems. Wen & Yu (1966) proposed a different type of correlation obtained from measurement of terminal velocity in sedimentations.

$$F_d = \begin{cases} (1+0.15\,\text{Re}^{0.687})(1-\phi)^{-3.65} \\ \dfrac{0.44\,\text{Re}}{24}(1-\phi)^{-3.65} \end{cases} \tag{2.3}$$

Currently, these two drag force correlations are widely used in CFD simulations. However, it is still unclear whether the correlations can be used for all the volume fractions and Reynolds numbers. With the development of computing power, direct numerical simulations (DNS) can be employed to derive the drag force for random assemblies of spheres for a wide range of volume fractions and Reynolds numbers, one such approach is the lattice Boltzmann method (LBM). DNS methods give high resolution at the surface of the particles, and the flow around the particles can be modeled in detail. Hill et al. (2001a, b) proposed the drag force correlation for random assemblies of spheres using LBM simulations:

$$F_d = F_0 + F_3\,\text{Re} \tag{2.4}$$

with

$$F_0 = \begin{cases} \dfrac{(1-\phi)(1+3/\sqrt{2}\,\phi^{1/2}+135/64\,\phi\ln\phi+16.14\phi)}{1+0.681\phi-8.48\phi^2+8.16\phi^3}, & \phi < 0.4 \\[2ex] 10\dfrac{\phi}{(1-\phi)^2}, & \phi > 0.4 \end{cases} \tag{2.5}$$

And $F_3 = 0.03365(1-\phi) + 0.106(1-\phi)\phi + 0.0116/(1-\phi)^4$. Beetstra et al. (2007) modified the Ergun equation in order to account for the effect of moderate fluid inertia on the particles. They proposed the following correlation for the drag force:

$$F_d(\phi,\mathrm{Re}) = 10\frac{\phi}{(1-\phi)^2} + (1-\phi)^2(1+1.5\sqrt{\phi}) + \frac{0.413\,\mathrm{Re}}{24(1-\phi)^2}\left[\frac{(1-\phi)^{-1}+3\phi(1-\phi)+8.4\,\mathrm{Re}^{-0.343}}{1+10^{3\phi}\,\mathrm{Re}^{-(1+4\phi)/2}}\right] \tag{2.6}$$

2.4 Previous studies of non-spherical particles

2.4.1 Shape factors for non-spherical particle

So far, nearly all the simulations for gas-solid flows are restricted to perfect spheres, since it is very simple to implement (Müller et al., 2008 and 2009). However, in most engineering applications the particles are non-spherical, which makes them more complicated to analyse. In order to describe the deviation from spherical shape, the sphericity factor Φ is introduced. Wadell (1934) defined the sphericity factor as the ratio of the surface area of a sphere with the same volume as the non-spherical particle to the surface area of the non-spherical particle. In engineering handbooks (Crowe, 2010) drag correlations for non-spherical particles are developed from correlations for spherical particles with corrections in terms of sphericity factor. However, this single characteristic value cannot differentiate the flow behavior, since differently shaped particles could have the same sphericity factor. Thus, various shape factors have been defined to classify non-spherical particles (Clift et al. 1978; Torobin et al. 1960). For example, the volume equivalent sphere diameter is defined as follows:

$$d_V = \sqrt[3]{6V_p/\pi} \tag{2.7}$$

where V_p is the particle volume. The projected area equivalent sphere diameter d_A is equal to:

$$d_A = \sqrt{4A_p/\pi} \tag{2.8}$$

where A_p is the projected area of the particle. The circularity of the particle is defined as follows:

$$c_r = \pi d_A/P_p \tag{2.9}$$

where P_p is the projected perimeter of the particle in its direction of motion.

2.4.2   Drag force for non-spherical particles

For non-spherical particles, the drag force is often expressed in terms of drag coefficient, defined as: $c_d = 8|\vec{F}_d'|/\rho\pi d_p^2 \vec{U}^2$. In the Stokes region Leith (1987) proposed the following equation for the drag coefficient c_d:

$$c_d = \frac{8}{\text{Re}}\frac{d_A}{d_V} + \frac{16}{\text{Re}}\frac{d_N}{d_V} \tag{2.10}$$

where d_N is the surface area equivalent diameter. Ganser (1993) gave a correlation for the Newton region (2000<Re<300000):

$$c_d = 0.42 \times 10^{1.8148(-\log\Phi)^{0.5743}} \tag{2.11}$$

with Leith's equation for the Stokes region. Tran-Cong et al. (2004) correlated the data from settling experiments with agglomerates of spheres and proposed the following correlation for the drag coefficient:

$$c_d = \frac{24}{\text{Re}}\frac{d_A}{d_V}\left[1 + \frac{0.15}{\sqrt{c_r}}(\frac{d_A}{d_V}\text{Re})^{0.687}\right] + \frac{0.42(\frac{d_A}{d_V})^2}{\sqrt{c_r}\left[1 + 4.25\times10^4(\frac{d_A}{d_V}\text{Re})^{-1.16}\right]} \tag{2.12}$$

On the basis of experimental data and numerical study, Hölzer et al. (2008) gave the following correlation for the drag coefficient:

$$c_d = \frac{8}{\text{Re}}\frac{1}{\sqrt{\Phi_{\parallel}}} + \frac{16}{\text{Re}}\frac{1}{\sqrt{\Phi}} + \frac{3}{\sqrt{\text{Re}}}\frac{1}{\Phi^{\frac{3}{4}}} + 0.42\cdot10^{0.4(-\log\Phi)^{0.2}}\frac{1}{\Phi_{\perp}} \tag{2.13}$$

where $\Phi_{\parallel}$ and $\Phi_{\perp}$ are the lengthwise and crosswise sphericity, respectively. It is worth noting that all these correlations are for single, isolated particles. Thus, they cannot be applied to gas-fluidized beds directly, since they do not take into account the solid volume fraction.

2.5   Approach

2.5.1   Lattice Boltzmann Method

The lattice Boltzmann method (Succi, 2001) provides an alternative approach to solve the Navier-Stokes equation. A detailed description of the method can be found in Ladd (1994a, b). The lattice Boltzmann equation (LBE) is a finite difference form of the Boltzmann equation (He and Luo, 1997). The LBE with single relaxation time used in the present work is as follows:

$$f_i(\vec{x} + \vec{e}_i\Delta t, t + \Delta t) = f_i(\vec{x},t) - \frac{\Delta t}{\tau}[f_i(\vec{x},t) - f_i^{eq}(\vec{x},t)] \tag{2.14}$$

where f_i is the single particle distribution function with velocity $\vec{e}_i$ at the position

$\vec{x}$ and time t, f_i^{eq} is the discrete equilibrium distribution and τ is the relaxation time.

$$\vec{e}_i = \begin{cases} (0,0,0), & i=0 \\ (\pm 1,0,0)c,(0,\pm 1,0)c,(0,0,\pm 1)c, & i=1...6 \\ (\pm 1,\pm 1,0)c,(\pm 1,0,\pm 1)c,(0,\pm 1,\pm 1)c, & i=7...18 \end{cases} \quad (2.15)$$

with c being the ratio of Δx and Δt. The LBE can be implemented by two steps, namely the collision step:

$$f_i(\vec{x},t_+) = f_i(\vec{x},t) - \frac{\Delta t}{\tau}[f_i(\vec{x},t) - f_i^{eq}(\vec{x},t)] \quad (2.16)$$

and the streaming step:

$$f_i(\vec{x}+\vec{e}_i\Delta t,t+\Delta t) = f_i(\vec{x},t_+) \quad (2.17)$$

In the D3Q19 model, the discrete equilibrium distribution function is

$$f_i^{eq} = w_i\rho_f(\vec{x},t)[1+3\frac{\vec{e}_i\cdot\vec{u}_f(\vec{x},t)}{c^2}+\frac{9}{2}\frac{(\vec{e}_i\cdot\vec{u}_f(\vec{x},t))^2}{c^4}-\frac{3}{2}\frac{\vec{u}_f^2(\vec{x},t)}{c^2}] \quad (2.18)$$

$$w_i = \begin{cases} \dfrac{1}{3}, & i=0 \\ \dfrac{1}{18}, & i=1...6 \\ \dfrac{1}{36}, & i=7...18 \end{cases} \quad (2.19)$$

where $\vec{u}_f(\vec{x},t)$ is the velocity of the fluid. The macroscopic properties of the fluid are obtained through the following equations:

$$\rho_f(\vec{x},t) = \sum_i f_i(\vec{x},t)$$

$$\rho_f(\vec{x},t)\vec{u}_f(\vec{x},t) = \sum_i f_i(\vec{x},t)\vec{e}_i \quad (2.20)$$

The viscosity is given by:

$$v = \frac{1}{6}c^2(2\tau - \Delta t) \quad (2.21)$$

2.5.2 Boundary condition for immersed particles

In this study, we employ an immersed moving boundary condition (Noble and Torczynski, 1998) for the solid phase which allows solid particles to overlap the lattice Boltzmann (LB) lattice. The LB equation is modified to enforce the non-slip condition, that is,

$$f_i(\vec{x}+\vec{e}_i\Delta t, t+\Delta t) = f_i(\vec{x},t) - \frac{\Delta t}{\tau}(1-B)[f_i(\vec{x},t) - f_i^{eq}(\vec{x},t)] + B\Omega_i^p \qquad (2.22)$$

Where B is a weighting function that depends on the local solid volume fraction and relaxation time:

$$B(\phi_x, \tau) = \frac{\phi_x(\frac{\tau}{\Delta t} - \frac{1}{2})}{(1-\phi_x) + (\frac{\tau}{\Delta t} - \frac{1}{2})} \qquad (2.23)$$

Ω_i^p is an additional collision term that bounces back the non-equilibrium part of the distribution

$$\Omega_i^p = f_{-i}(\vec{x},t) - f_i(\vec{x},t) + f_i^{eq}(\rho_f(\vec{x},t), \vec{u}_p(\vec{x},t)) - f_{-i}^{eq}(\rho_f(\vec{x},t), \vec{u}_f(\vec{x},t)) \qquad (2.24)$$

where $\vec{u}_p(\vec{x},t)$ is the particle velocity at time t, and $-i$ denotes the distribution component which has the opposite direction to i. Compared with the bounce back boundary condition, this method shifts the boundary smoothly at the solid-fluid interface. It allows sub grid resolution of moving boundaries. The total hydrodynamic force exerted on the particle can be calculated by summing up the momentum transfer that occurs over the n nodes covered by the particle as

$$\vec{F}'_{tot} = \frac{\Delta x^2}{\Delta t} \sum_n B_n \sum_i \Omega_i^p \vec{e}_i \qquad (2.25)$$

2.6   Validation of the LBM code

The LBM code was validated by comparing the drag coefficient calculated from simulations of the flow past an isolated sphere with the empirical equation from Bird et al. (2007). Since it is difficult to validate simulations of dense suspensions that use periodic boundary conditions with experiments, we compare our results with previous numerical investigations.

2.6.1   Drag force acting on a single sphere in an unbounded flow

The drag force acting on an isolated sphere in an unbounded flow is a well-studied problem which has an analytical solution for low Reynolds numbers and many experimental data covering a wide range of Reynolds numbers (here the Reynolds number is defined as: $Re = |\vec{U}|d_p/\upsilon$, where $\vec{U}$ was equal to the undisturbed field velocity far from the sphere). The drag coefficient of the sphere is defined as:

$$c_d = \frac{8|\vec{F}'_d|}{\rho\pi d_p^2 \vec{U}^2} \qquad (2.26)$$

To verify the 3D flow past a single sphere, the drag coefficient as a function of Re was calculated. For low Reynolds numbers (Re $\leq$ 1), a relatively large box dimension

$(10d_p \times 10d_p \times 10d_p)$ is required to obtain highly accurate values for drag force (equation (2.26)). On the other hand a smaller domain size $(5d_p \times 5d_p \times 5d_p)$ is sufficient for $Re > 1$, thus, the solid volume fraction of the system was 0.00052 and 0.0042, respectively. The value of d_p was 10 lattice units for $Re \leq 150$, and greater than 10 lattice units for $Re > 150$, reaching 30 lattice units at $Re = 200$. The center of the sphere was located at the center of the domain. At the inlet, a constant velocity boundary condition was used. At the outlet boundary, a stress free condition was specified, periodic boundary conditions were applied to the other two directions. Figure 2.1 shows a comparison between the LBM data, the empirical equation of Bird et al. (2007) and the Stokes solution. The LBM results lie slightly above the empirical equation and the Stokes solution for low Reynolds numbers. This is due to the finite computational domain used in the simulations. In contrast the empirical equation and Stokes solution were developed for a single particle in an infinite medium.
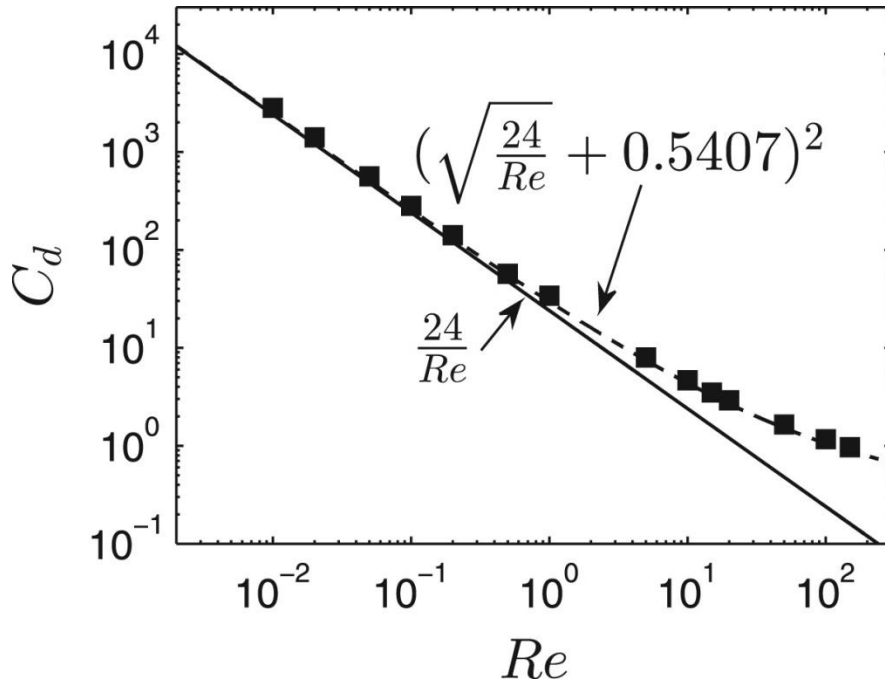
Figure 2.1. Drag coefficient for a single sphere as a function of Reynolds number. The black squares show data obtained from the LBM simulations reported here. The solid line is the Stokes solution, the dashed line is the empirical equation of Bird et al. (2007).

2.6.2 Stokes flow past a sphere in body centred cubic lattice

Hasimoto (1959) calculated the total force on spheres in dilute simple cubic, body-centered cubic and face-centered cubic arrays by use of Fourier series. For simple cubic arrays the total force is given by

$$\frac{3\pi\mu_f d_p \vec{U}}{\vec{F}_{tot}} = 1 - 1.7601\phi^{\frac{1}{3}} + \phi - 1.5593\phi^2 + O(\phi^{\frac{8}{3}}) \tag{2.27}$$

where μ_f is the dynamic viscosity. The first term on the right-hand side is the Stokes

result for an isolated sphere in unbounded flow; the next three terms are due to the finite domain size. For a given volume fraction ($\phi = 0.0024$, domain size $6d_p \times 6d_p \times 6d_p$), we use the LBM to simulate the flow and measure the drag acting on the sphere. Figure 2.2 plots the normalized total force as a function of the diameter. The simulation agreed well with the analytical solution if the diameter was larger than 7 lattice units.
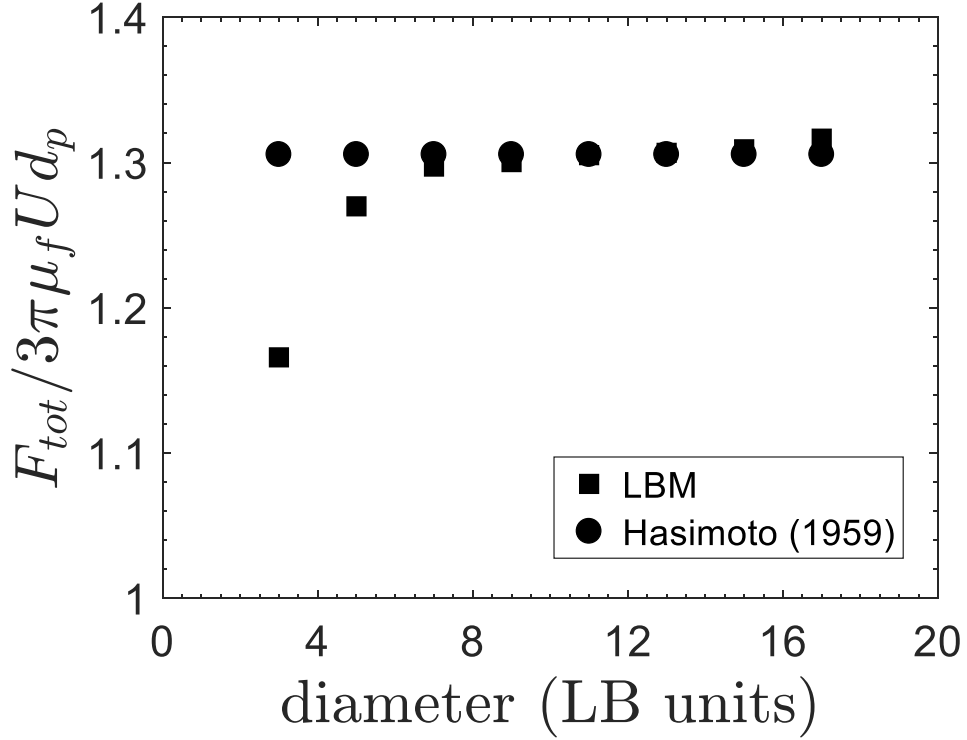

Figure 2.2. Total force acting on spheres arranged in a body centred cubic lattice (i.e. periodic boundary condition). The solid volume fraction is $\phi = 0.0024$ and Re is 0.01.

2.6.3   Drag force on random assemblies of spheres

Stokes flow past random assemblies of spheres has been studied in detail by several researchers (Hill et al., 2001a; van der Hoef et al., 2005). In Fig. 2.3 we compare the drag force obtained from LBM simulations with the result of van der Hoef et al. (2005). The diameters of the spheres lie in range 17.5-30. The dynamic viscosity is $\mu_f = 0.01$ (lattice units: distance between neighbouring nodes). Due to the finite resolution of the flow field, the drag force may deviate from the result of infinite resolution. To assess the influence of the grid resolution on the drag force, we have performed a set of simulations using different grid resolutions for the identical configuration. In these simulations, the particle size and Reynolds number were kept constant. An estimate for the resolution between particles is given by the hydraulic radius $r_h = d_p(1 - \phi)/6\phi$. From Fig. 2.4 we can see that the drag force is a function of $1/r_h^2$ for assemblies of spheres. From Fig. 2.5 we observe the same linear dependence of F_d on $1/r_h^2$ for assemblies of approximately cubic particles.

Therefore, simulations with four different values of r_h were performed for each system. The final drag force was obtained by extrapolating to $1/r_h^2 = 0$, which corresponds to the case of infinite resolution. For a $\text{Re} \geq 100$ ($\text{Re} = |\vec{U}|d_p/\nu$) the drag force is not a linear function of $1/r_h^2$ for assemblies of approximately cubic particles, i.e. Fig. 2.6. For high Reynolds numbers the values of F_d obtained for different values of r_h were averaged to obtain F_d for each configuration. Table 2.1 summarizes the drag force acting on assemblies of spheres for different volume fractions ($R_e = 104.9$ and 209.9) using different drag force correlations (Here HKL and BHK refer to Hill et al. (2001a, b) and Beetstra et al. (2007), respectively). The data summarized in Table 2.1 demonstrate that our LBM simulations are in excellent agreement with the results of BHK. The validation tests described in this section indicate that our LBM simulations are capable to be applied in our studies.
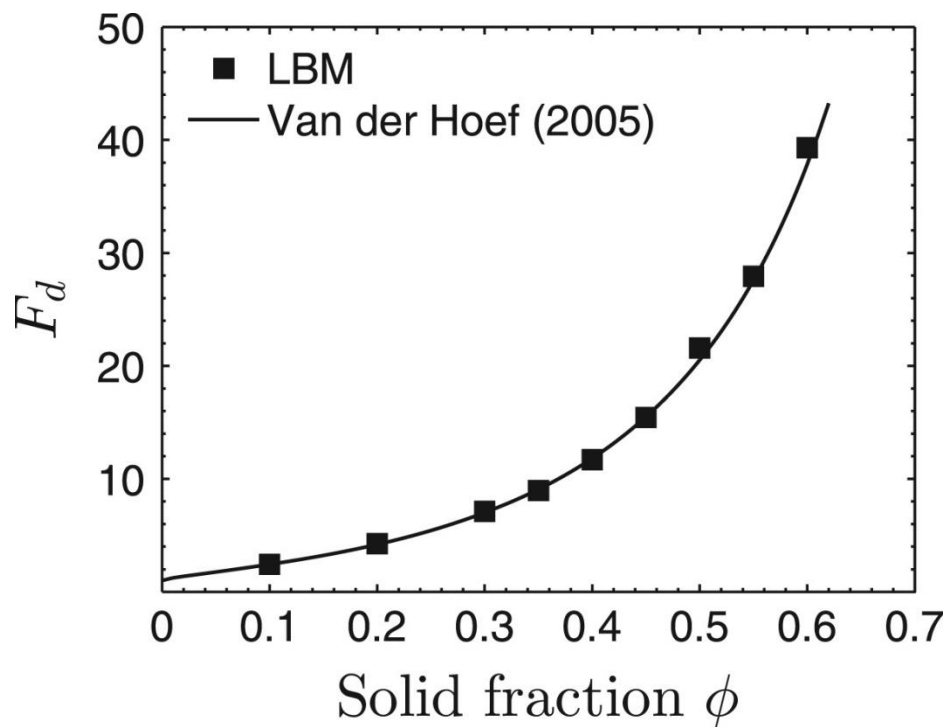
Figure 2.3. Drag force acting on a random assembly of spheres. The Reynolds number is 0.01 and $\nu = 0.01$.
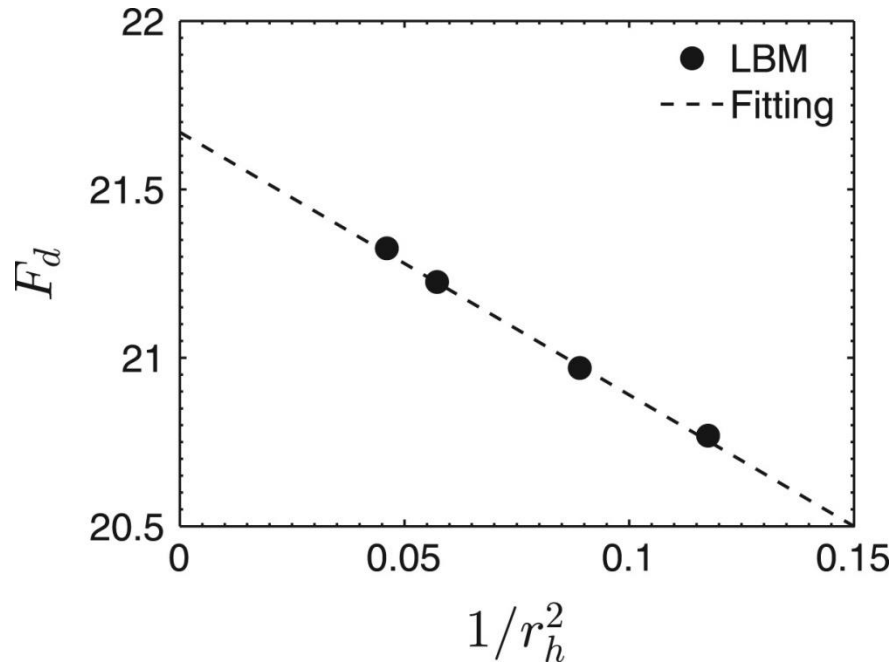
Figure 2.4. Normalized drag force as a function of $1/r_h^2$ (lattice units) for a low Reynolds number (Re = 0.01) using random assemblies of spheres. The solid volume fraction is 0.5 and the dynamic viscosity is 0.01.
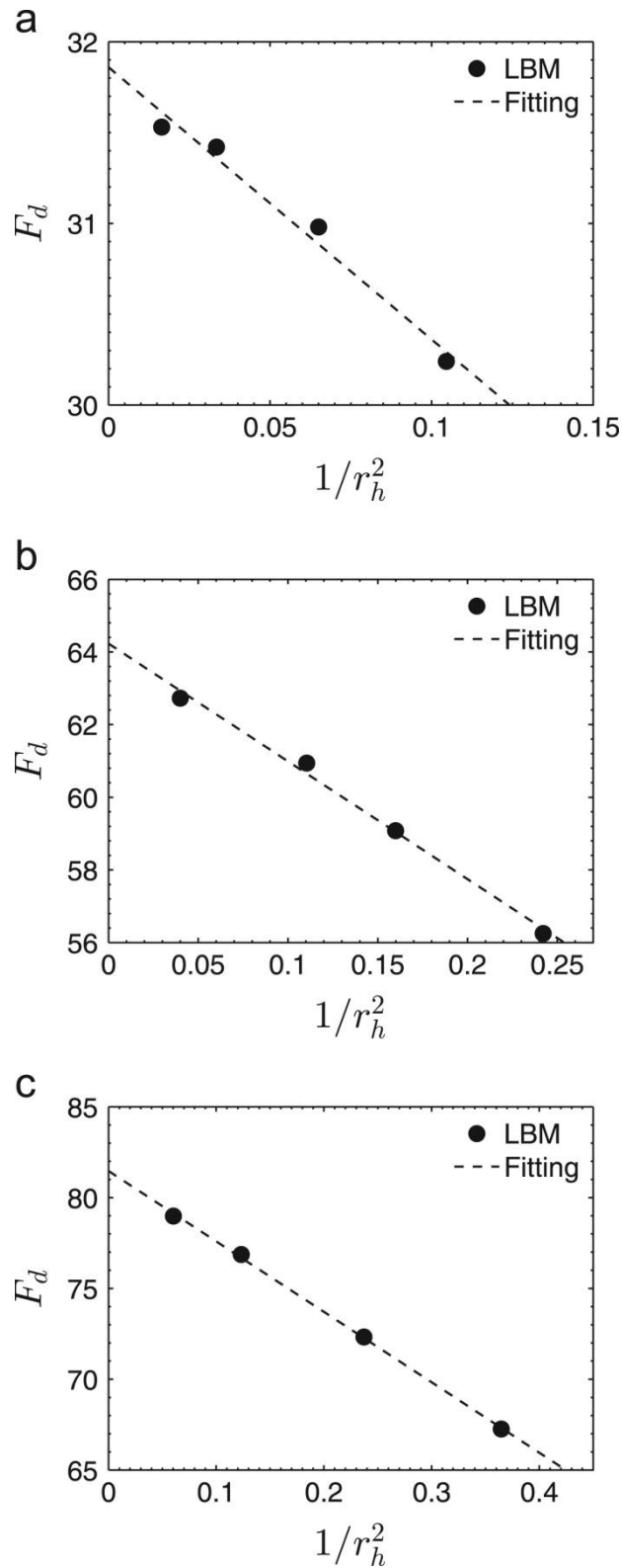
Figure 2.5. Normalized drag force as a function of $1/r_h^2$ for $Re = 50$ for random assemblies of approximately cubic particles. The viscosity is $\nu = 0.01$. (a) $\phi = 0.3$, (b) $\phi = 0.4$, (c) $\phi = 0.45$.

Figure 2.6. Normalized drag force as a function of $1/r_h^2$ for $Re = 100$ and random assemblies of approximately cubic particles. The dashed line is the average value of F_d using four different values of $1/r_h^2$. The viscosity is $\nu = 0.00427$.

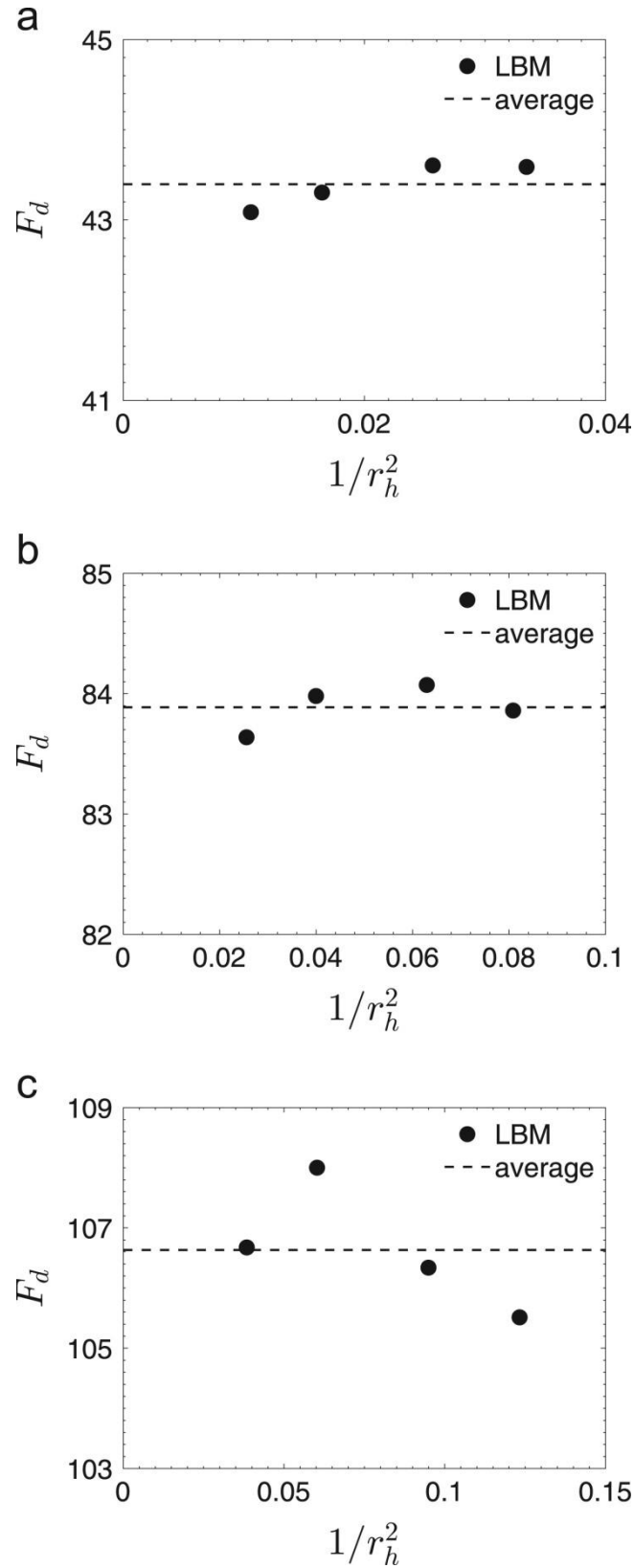| φ	Re	LBM	HKL	BHK	Ergun	Wen & Yu
0.3	104.9	19.43	16.48	20.70	25.92	17.13
	209.9	29.65	26.36	32.72	16.75	25.39
0.4	104.9	31.20	25.17	31.92	37.59	30.11
	209.9	47.87	39.36	49.54	65.95	44.56
0.5	104.9	48.56	44.01	48.70	57.46	58.59
	209.9	75.09	68.05	74.81	98.29	86.70

Table 2.1. Drag force acting on random assemblies of spheres for Re = 104.9 and 209.9. The simulations performed here (LBM) are compared with the results of Hill et al. (2001a, b) (HKL) and Beetstra et al. (2007) (BHK). Furthermore, predictions using the correlations of Ergun (1952) and We & Yu (1966) are also given.

2.7 Simulation and Results

We began our simulations by randomly distributing approximately cubic particles in cubic, periodic domains. There is no clear definition of a random system for this type of particles, however, it is assumed that the configurations generated by this Monte Carlo method are sufficiently random for this work. The particles considered here are constructed from 8 identical spheres, each with a diameter of d_p. The surface of adjacent spheres is in contact but the spheres do not overlap. This configuration is shown in Fig. 2.7a. There are several methods to generate packings for spheres. One approach used in the literature is to drop spheres into a box sequentially, the packing is obtained when the spheres come to a stable rest state (Lebon et al., 1996). Another method uses a granular dynamics simulation based on the DEM (Rong et al., 2013). In this paper we use a Monte Carlo method to generate the packing (Frenkel and Smit, 1996). All the approximately cubic particles are placed initially in an ordered configuration. Subsequently, each particle is moved and rotated randomly. If there is no overlap with other particles at new position, the orientation and coordinates of the approximately cubic particles are updated, otherwise the move is rejected. A sample configuration produced by this method is shown in Fig. 2.7b.

(a)

(b)
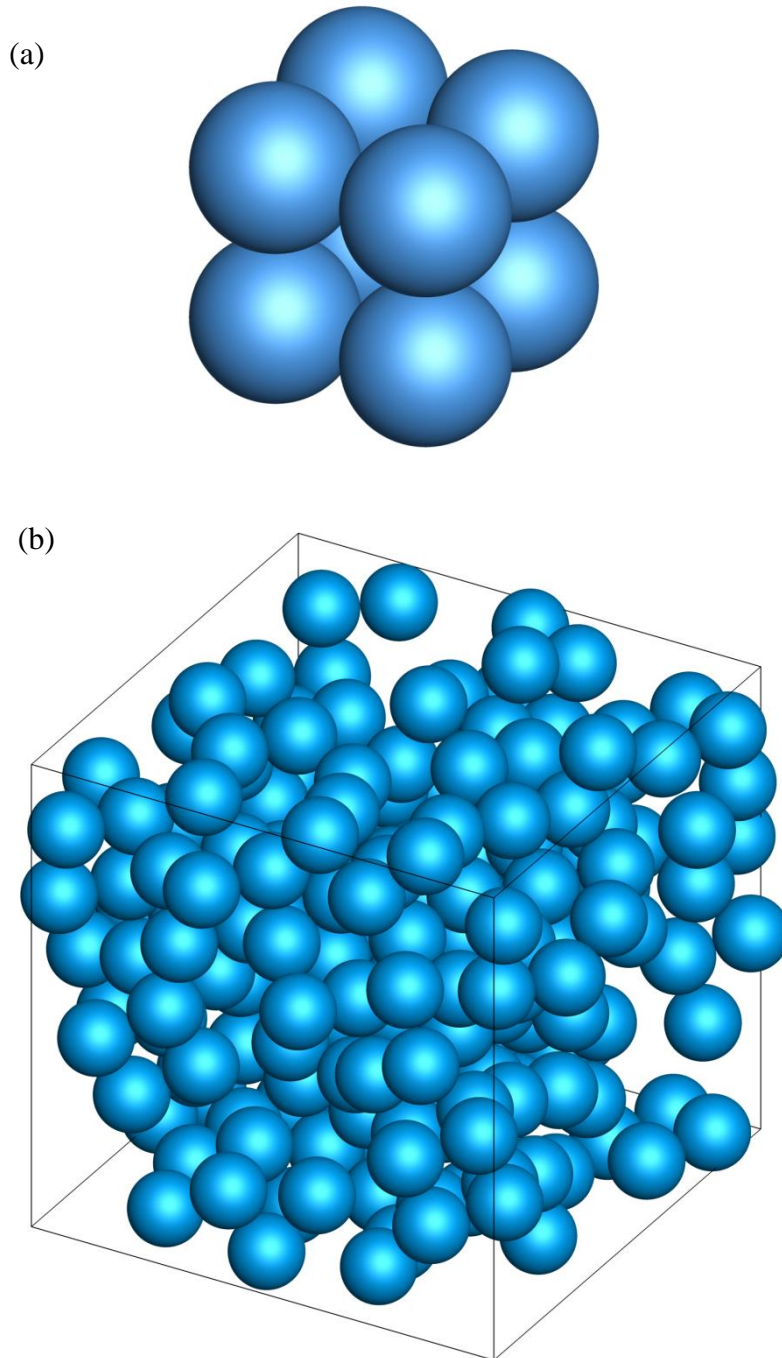
Figure 2.7. (a) Configuration of 8 identical spheres; (b) Random array of approximately cubic particles constructed from 8 identical spheres, $N = 25$, $\phi = 0.3$.

All quantities used in the simulations are defined in lattice Boltzmann units (l. u.). In the simulations, $N = 25$ approximately cubic particles are arranged randomly in a cubic box via a Monte Carlo procedure, where d_p has a value in the range 7 to 32.5 lattice spaces. To access a range of Re, various fluid viscosity values ($\mu_f = 0.01$ and $\mu_f = 0.00427$ [l. u.]) were used. The fluid velocity is very low (< 0.01 [l. u.]) in order to ensure numerical stability. Periodic boundary conditions are used in all

directions. All particles are moved with the same constant velocity $\vec{u}_p$ in some arbitrary direction, so there is no relative motion between the approximately cubic particles. A uniform force is applied to the fluid phase to balance the total force from the moving particles on the fluid phase. This ensures that the total momentum of the fluid is zero. The superficial velocity $\vec{U}$ was equal to $-\vec{u}_p$. The particle Reynolds number of the approximately cubic particle is defined based on the diameter of a volume-equivalent sphere, i.e. $\text{Re} = |\vec{u}_p|(2d_p)/\nu$, and the drag force of the particle was normalized by $3\pi\mu_f u_p(2d_p)$. After the simulation has reached steady state, the force was averaged over a large period of time (30000-200000 time steps). A second average was performed over 6 different combinations of particle configurations and flow directions. In this work, we did not include the data which deviated more than three times the standard deviation from the mean value.

2.7.1 Drag force for assemblies of approximately cubic particles

Figure 2.8 shows the simulation data for the normalized drag force for random assemblies of approximately cubic particles as a function of Reynolds number. The following function fits the data well:

$$F_d(\phi,\text{Re}) = \frac{10\phi}{(1-\phi)^2} + \frac{10\phi}{1-1.14\phi^{0.3}} + \frac{0.413\,\text{Re}}{24(1-\phi)^2}[\frac{-0.058(1-\phi)^{-4}+2.16(1-\phi)+23\phi(1-\phi)+8.4\,\text{Re}^{-0.343}}{1+10^{3\phi}\,\text{Re}^{(-0.5-2\phi)}}] \tag{2.27}$$

The first two terms are the drag force for low Reynolds numbers. The form of the second term was selected based on the Carman equation and the coefficients were determined by minimising the difference between the correlation and the simulation data. The third term is a modification of Beetstra et al.'s inertial part by adding a voidage $(1-\phi)$ term following the drag force correlation proposed by Hill et al. (2001b). In Fig. 2.9 we plot our simulation data and Ergun equation for $\alpha(\phi,\text{Re})$ $(\alpha = \frac{F_d(\phi,Re)-F_d(\phi,0)}{Re})$ multiplied by $(1-\phi)^2$, as a function of ϕ. We find that the Ergun equation cannot be applied to the non-spherical particles constructed from spheres directly even for high packing fractions. Our data indicate that α is dependent on the Reynolds number. This is demonstrated more clearly in figure 2.10, where we plot $\alpha(1-\phi)^2$ as a function of Reynolds numbers. It can be seen that the slope of the curve decreases with Re. For $\text{Re} > 50$, α is not very sensitive to the exact value of Re. Figures 2.11, 2.12 and 2.13 compare the results for the drag force and $\alpha(1-\phi)^2$ from the simulations with the correlation proposed by Beetstra et al. (2007), i.e. eq. (2.6). Figure 2.11 shows that Beetstra et al.'s correlation over-predicts the drag force for the individual spheres. The configurations of spheres used in Beetstra et al.'s simulations were considered to be random and the systems were homogeneous. In contrast, the simulations reported here consider approximate cubic particles constructed from 8 identical spheres. Consequently the spheres are not homogeneously distributed in these simulations. In our systems with a low porosity the size of the pores are not that so different, ensuring a more homogeneous flow field

than at higher porosity configurations, so the agreement with Beetstra et al. (2007) is better. In dilute systems some particles will be shielded by particles which are in front of them in the direction of flow. Consequently these shielded particles will experience a lower drag force (Liang et al., 1996). Therefore at high porosities the drag force is substantially different to the predictions of Beetstra et al. (2007), whereas at low porosities (i.e., ϕ=0.4, 0.45) the drag force approaches the value for randomly arranged particles. Increasing the Reynolds number for high packing fractions increases the difference between our simulation data and the correlation proposed by Beetstra et al. (2007), indicating that the drag force is significantly affected by the sphere configuration at moderate Reynolds numbers. Figures 2.12 and 2.13 show the form-drag coefficient α as a function of ϕ and Re. It is clear that the inertial contribution to the drag force is significantly affected by the packing configuration. The inertial contribution has a smaller value than the one for random packings. Figures 2.14 and 2.15 compare the newly proposed drag force correlation with Beetstra et al. (2007) based on the same Reynolds number definition, i.e. Re =

$\left|\vec{u}_p\right|(2d_p)/\nu$. They show that Beetstra et al.'s correlation (Eq. 2.6) does not represent

the data well. In most of the cases it over-predicts the drag force acting on the approximately cubic particle. The data presented above indicate that Beetstra et al.'s correlation cannot be applied directly to non-spherical particles constructed from spheres, i.e. by considering the approximately cubic particles as a sphere of equal volume.
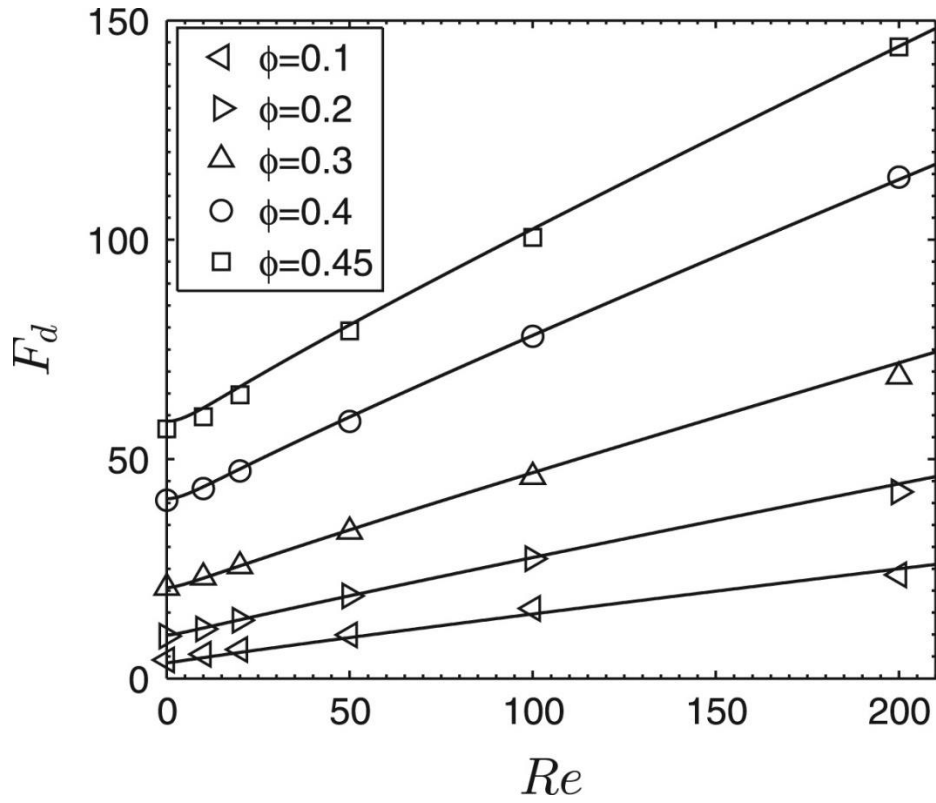
Figure 2.8. Normalized drag force for approximately cubic particles as a function of
Reynolds number. The data points show the results of current LBM simulations. The
lines show the newly proposed correlation, e.g. highest line represents φ = 0.45.
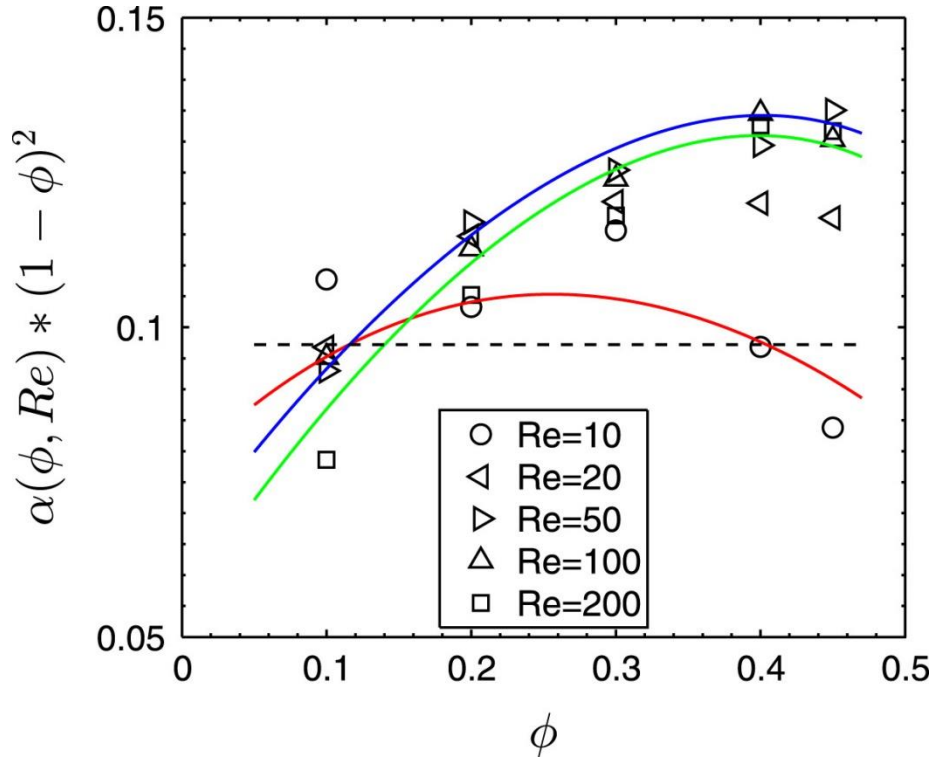
Figure 2.9. Plot of $\alpha(1-\phi)^2$ as a function of solid fraction for assemblies of approximately cubic particles. The data points show the results of current LBM simulations. The red, blue and green lines are the newly proposed drag force correlation for Re=10, 50 and 200, respectively and the dashed line plots the Ergun equation.
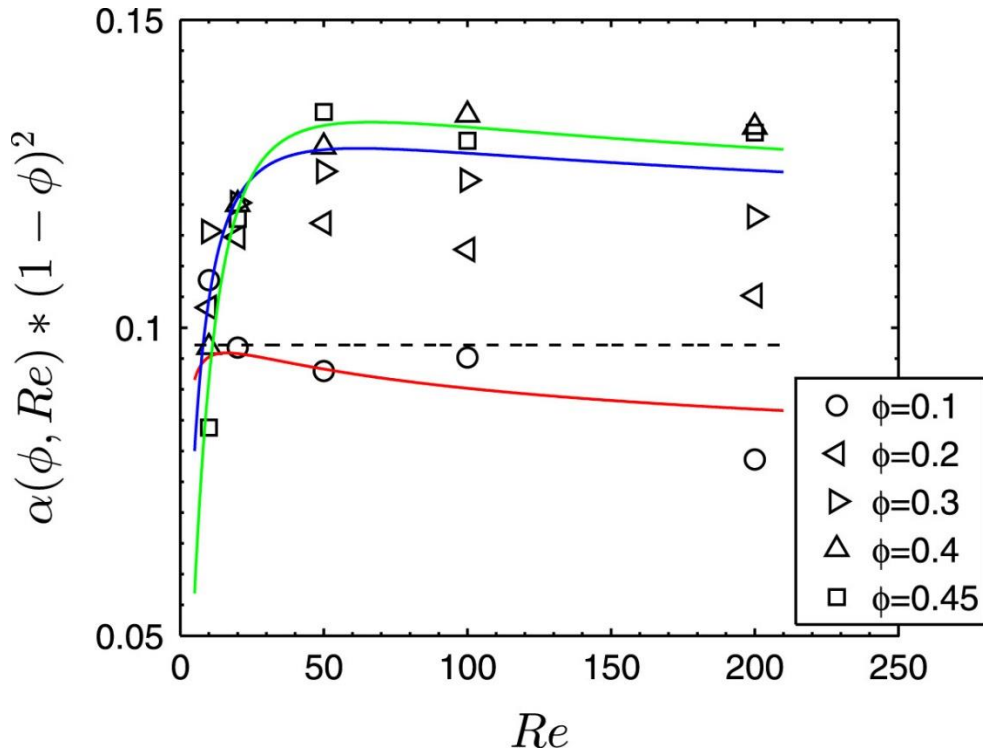
Figure 2.10. Plot of $\alpha(1-\phi)^2$ as a function of Reynolds number for assemblies of approximately cubic particles. The data points show the results of current LBM simulations. The red, blue and green lines are the newly proposed drag force correlation for ϕ=0.1, 0.3 and 0.45, respectively and the dashed line plots the Ergun equation.
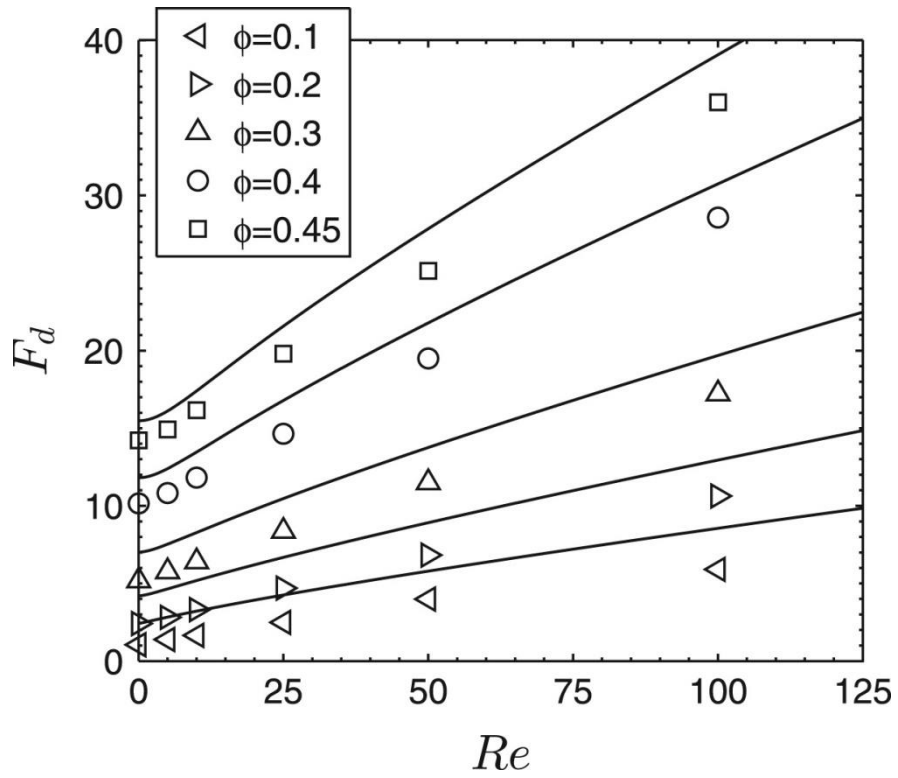
Figure 2.11. Normalized drag force acting on the individual spheres (approximately cubic particles simulations) as a function of the Reynolds number. The data points show the results of current LBM simulations. The lines show Beetstra's correlation, where the highest line represents $\phi=0.45$, and the lowest $\phi=0.1$.
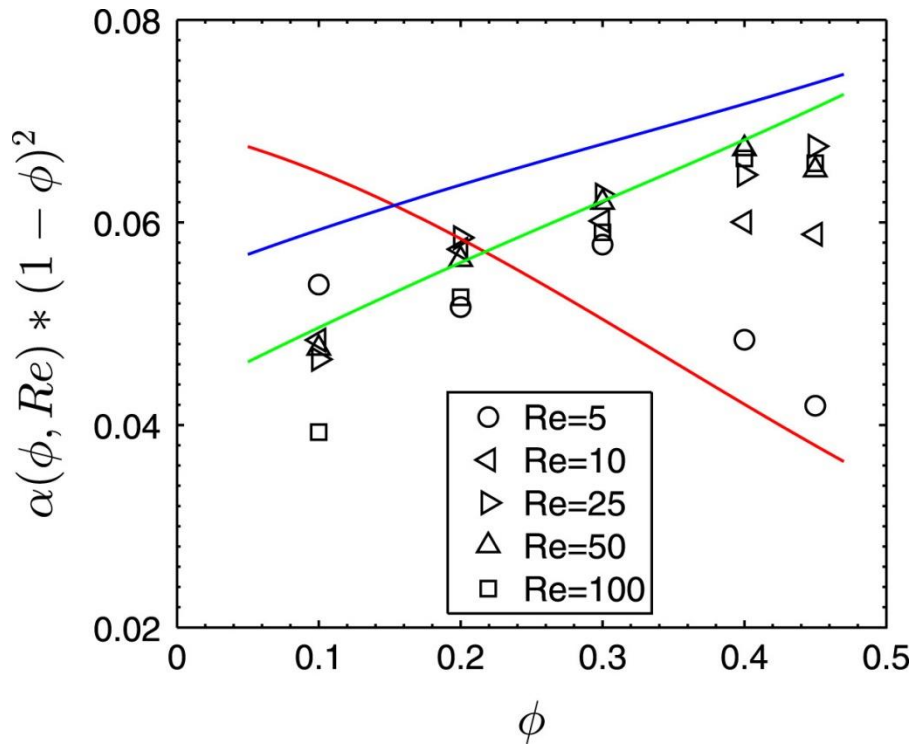
Figure 2.12. Comparison of the drag force acting on a single sphere (approximately cubic particles simulations) with the correlation proposed by Beetstra et al. (2007). The data points show the results of current LBM simulations. The red, blue and green lines are the drag force correlation proposed by Beetstra et al. (2007) for Re=5, 25 and 100, respectively.
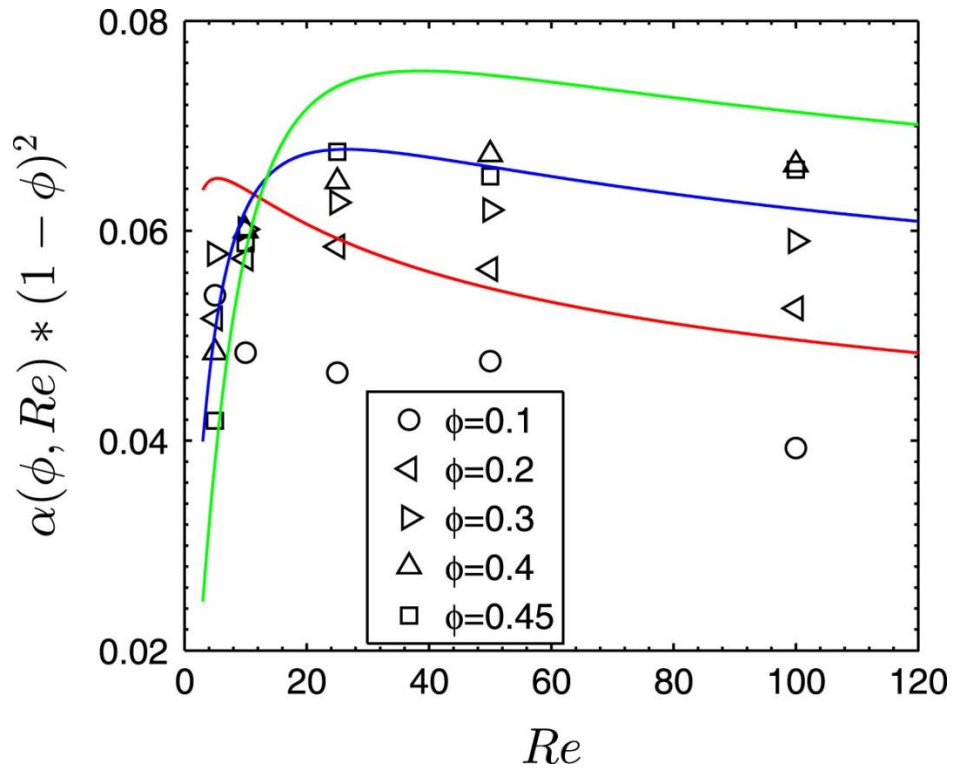
Figure 2.13. Comparison of the drag force acting on a single sphere (approximately cubic particles simulations) with the correlation proposed by Beetstra et al. (2007). The red, blue and green lines plot the predictions of the drag force correlation proposed by Beetstra et al. (2007) for ϕ=0.1, 0.3 and 0.45, respectively.
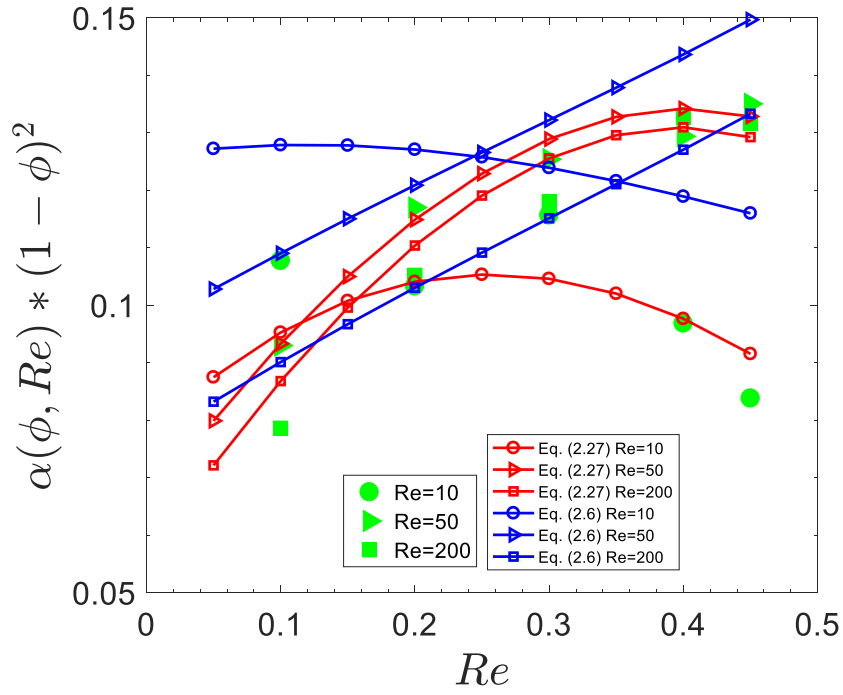
Figure 2.14. Comparison of the newly proposed drag force correlation for assemblies of approximately cubic particles with the correlation proposed by Beetstra et al. (2007). The data points show the results from current LBM simulations. The comparison is performed by modelling the approximately cubic particles as volume equivalent spheres.
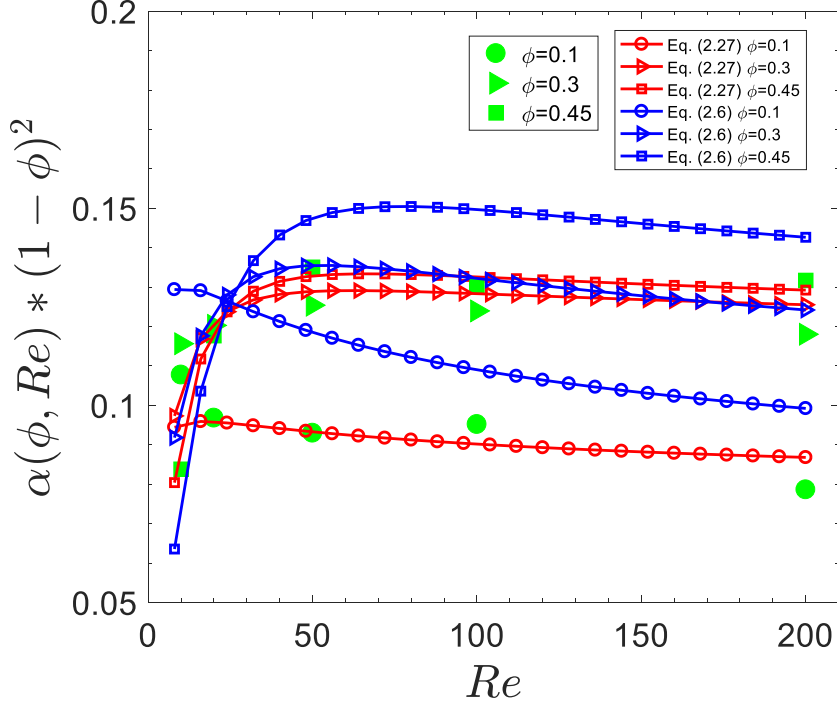
Figure 15. Comparison of the newly proposed drag force correlation for assemblies of cubic particles with the correlation proposed by Beetstra et al. (2007). The data points show the results from current LBM simulations. The comparison is performed by modelling the approximately cubic particles as volume equivalent spheres.

2.8 Conclusions

The lattice Boltzmann method has been used to compute the drag force acting on assemblies of approximately cubic particles constructed from 8 spheres for a wide range of Reynolds number. Based on the simulation data we propose a new drag force correlation for this kind of particles. Since there is no trivial method to couple ϕ and Re in a drag force correlation, we use a Beetstra-type equation to fit the data. We have compared the drag force obtained in our simulations with that predicted by the correlation proposed by Beetstra et al. (2007). This comparison was done by considering either the drag acting on individual spheres, or the drag acting on an approximately cubic particle composed by 8 spheres. These comparisons showed that Beetstra et al.'s correlation cannot predict the system well. The drag force acting on a single sphere is smaller than that predicted by the correlation proposed by Beetstra et al. (2007), and the drag force acting on an approximately cubic particle is also smaller than that predicted by Beetstra's correlation based on the same Reynolds number definition. The discrepancy arises because grouping the spheres into approximately cubic particles results in a less homogeneous packing than the packings studied by Beetstra et al. (2007). The difference is particularly pronounced for high Reynolds

numbers. The correlation proposed in this paper will enable CFD-DEM and Euler-Euler simulations of approximately cubic particles, allowing the influence of the solid volume fraction in CFD-DEM models to be assessed.

3

The effect of solid volume fraction and Reynolds number on the drag force acting on assemblies of cubic particles

3.1 Abstract

The accurate prediction of the drag force exerted by a fluid on assemblies of particles is critical to simulate key characteristics of gas-solid systems such as the bed expansion in fluidized beds. To this end, a lattice Boltzmann method has been applied to compute the drag force acting on assemblies of cubes for a wide range of Reynolds numbers, $\mathrm{Re} = 0 - 200$, and solid volume fractions, $\phi = 0.1 - 0.45$. The numerical data was used to propose a new drag force correlation for assemblies of cubes as a function of the Reynolds number and solid volume fraction. The new drag force correlation is expected to improve the accuracy of Euler-Euler and Euler-Lagrangian simulations of cubic particles.

3.2 Introduction

The numerical simulation of gas-solid systems, e.g. fluidized beds, relies critically on the accurate formulation of the drag force exerted by a fluid on the particulate phase. For example, Li et al. (2003) reported that the bed expansion in a gas fluidized bed is very sensitive to the dependence of the drag force on the voidage for the different drag-force correlations assessed. The most commonly used drag force correlations in the field, i.e. the correlations by Ergun (1952) and Wen & Yu (1966) were derived experimentally by measuring the pressure drop in packings and the sedimentation velocity, respectively. However, it is under debate whether these correlations can be used for the wide range of solid volume fractions typically encountered in fluidized beds (Gidaspow, 1994). Due to the difficulty to perform highly resolved (both temporally and spatially) experiments in gas-solid systems (Müller et al., 2006; Holland et al., 2008; Müller et al., 2011), recently, direct numerical simulations (DNS) have been employed to improve the accuracy (and parameter space) of drag force correlations. In direct numerical simulations the fluid flow around the particles is fully resolved and the drag force acting on the individual particles can be calculated accurately. Hill et al. (2001b) were the first to derive a drag force correlation for assemblies of spheres using a lattice Boltzmann method as a DNS technique. Beetstra et al. (2007) extended the work of Hill et al. (2001b) and proposed new drag force correlations for mono- and bi-disperse assemblies of spheres. Recent works dedicated to improve the accuracy of predictions of the drag force acting on assemblies of spheres for a wide range of Reynolds number have focused on two aspects: (1) developing highly accurate solid-fluid boundary conditions (Tenneti et al., 2011; Tang

et al., 2014) and (2) introducing granular temperature into the drag force correlation for assemblies of spheres (Tang et al., 2016). For example, Tenneti et al. (2011) applied an immersed boundary method with a grid resolution sufficiently fine such that the values determined for the drag force became grid independent, allowing them to propose a new drag force correlation for mono-disperse spheres. When compared to the correlation of Beetstra et al. (2007) differences of up to 30% in the Reynolds number range 100 -300 were observed. Tenneti et al. (2011) argued that the differences were largely due to differences in the grid resolution of the underlying DNS simulations. Tang et al. (2014) developed an accurate immersed boundary method using effective hydraulic diameters, allowing them to keep the computational cost relatively low. Using their simulation data a new drag force correlation was proposed for static and dynamic arrays of spheres (Tang et al., 2015, 2016). Despite the recent progress in this area, the drag force correlations listed above are restricted to spherical particles only. Indeed, very little progress has been made in the development of drag force correlations for non-spherical particles. The first attempt for a drag force correlation for non-spherical particles was made by Haider and Levenspiel (1989), who formulated a general expression for a drag coefficient for single spherical and non-spherical particles in incompressible flow. Subsequently, several new drag force correlations for different particle shapes (and orientations) were proposed (Tran-Cong et al., 2004; Yow et al., 2005; Hölzer et al., 2008). However, these correlations do not take into account the effect of solid volume fraction on the drag force (i.e. are for single particles only). The correlation derived by Hölzer et al. (2008) has been employed for the simulations of gas-solid flows comprising mono-dispersed non-spherical particles, i.e. cuboids and ellipsoids (Hilton et al., 2010, 2011). The work of Hilton et al. (2010) highlighted the limitations of approximating non-spherical particles by spheres and emphasized that particle shape is a critical parameter to determine accurately drag force correlations. To this end, we conduct direct numerical simulations of fluid flowing over assemblies of cubes and develop a drag force correlation that is applicable for Euler-Euler and Euler-Lagrangian simulations.

3.3 Previous studies of the drag force acting on non-spherical particles

3.3.1 Shape description of non-spherical particles

The drag force acting on a non-spherical particle is expressed commonly in the form of a drag coefficient that is a function of the particle Reynolds number and particle shape. The deviation of a particle shape from a sphere is typically quantified through a sphericity factor Φ. Wadell (1933) defined the sphericity factor (Φ) as the ratio of the surface area of a volume equivalent sphere to the surface area of the non-spherical particle. However, the sphericity factor cannot describe the orientation of the particle with respect to the flow. Moreover, the sphericity factor cannot distinguish between different shapes, i.e. differently shaped particles could have the same sphericity factor. Hence, further equivalent diameters have been introduced to characteristic a particle's

dimensions (with the same shortcomings as the sphericity factor). For example, the volume equivalent sphere diameter is defined as:

$$d_V = \sqrt[3]{6V_p / \pi} \tag{3.1}$$

where V_p is the particle volume. The projected area equivalent sphere diameter d_A is equal to

$$d_A = \sqrt[2]{4A_p / \pi} \tag{3.2}$$

where A_p is the projected area of the particle. The surface area equivalent sphere diameter, d_N, is calculated as:

$$d_N = \sqrt[2]{S_p / \pi} \tag{3.3}$$

Here, S_p is the particle surface area. The Sauter diameter of a particle is:

$$d_s = d_V^3 / d_N^2 \tag{3.4}$$

Therefore, the sphericity can be re-written as:

$$\Phi = \frac{d_V^2}{d_N^2} \tag{3.5}$$

3.3.2   Drag coefficient for a single, non-spherical particle

For a single particle immersed in a fluid, the drag coefficient is defined as:

$$c_d = 8\left[\vec{F}_d'\right] / \rho_f \pi d_A^2 \vec{U}^2 \tag{3.6}$$

where ρ_f is the fluid density and $\vec{F}_d'$ is the drag force acting on the particle. For the Stokes regime, Leith (1987) proposed the following expression for the drag coefficient c_d:

$$c_d = \frac{8}{\mathrm{Re}} \frac{d_A}{d_V} + \frac{16}{\mathrm{Re}} \frac{d_N}{d_V} \tag{3.7}$$

The first and second terms on the right hand side of Eq. (3.7) describe the drag acting on a sphere with an identical projected area and an identical surface area, respectively. Fitting of the experimental measurements of drag coefficients for isometric particles (e.g. cubes, spheroids), Pettyjohn & Christiansen (1948) and Ganser (1993) proposed the following equation to predict the drag coefficient of a single, non-spherical particle up to Reynolds number 1×10^5.

$$c_d = \frac{24}{Re}\left(\frac{d_A}{3d_V} + \frac{2d_N}{3d_V}\right)\left(1 + 0.1118 \cdot \left(Re\left(\frac{1}{3}\frac{d_A}{d_V} + \frac{2}{3}\frac{d_N}{d_V}\right)^{-1} \cdot 0.4305 \cdot 10^{1.8148(-\log\Phi)^{0.5743}}\right)^{0.6567}\right)$$

$$+ \frac{0.4305 \cdot 10^{1.8148(-\log(\Phi))^{0.5743}}}{1 + \dfrac{3305}{Re\left(\frac{1}{3}\frac{d_A}{d_V} + \frac{2}{3}\frac{d_N}{d_V}\right)^{-1} \cdot 0.4305 \cdot 10^{1.8148(-\log(\Phi))^{0.5743}}}}$$

<div align="right">(3.8)</div>

Measuring the settling velocities of six different agglomerates that were constructed by gluing together spheres, Tran-Cong et al. (2001) derived the following expression for the drag coefficient of non-spherical particles:

$$c_d = \frac{24}{Re}\frac{d_A}{d_V}\left[1 + \frac{0.15}{\sqrt{c_r}}\left(\frac{d_A}{d_V}Re\right)^{0.687}\right] + \frac{0.42\left(\frac{d_A}{d_V}\right)^2}{\sqrt{c_r}\left[1 + 4.25 \times 10^4\left(\frac{d_A}{d_V}Re\right)^{-1.16}\right]} \tag{3.9}$$

where c_r is the particle circularity defined as $c_r = 2\pi d_A/P$, P is the projected perimeter of the particle with respect to the flow direction. Combing experimental data of the drag coefficients of differently shaped particles from literature and their own numerical data, Hölzer et al. (2008) proposed the following correlation to calculate the drag coefficient of a single, non-spherical particle:

$$c_d = \frac{8}{Re}\frac{1}{\sqrt{\Phi_\perp}} + \frac{16}{Re}\frac{1}{\sqrt{\Phi}} + \frac{3}{\sqrt{Re}}\frac{1}{\Phi^{\frac{3}{4}}} + 0.42 \cdot 10^{0.4(-\log\Phi)^{0.2}}\frac{1}{\Phi_\perp} \tag{3.10}$$

Here $\Phi_\perp$ is the crosswise sphericity defined as the ratio between the cross-sectional area of the volume equivalent sphere and the projected cross-sectional area of the particle. The mean relative error of Eq. (3.10) was 14.4% with respect to the data used for fitting.

3.3.3 Drag force correlation for assemblies of non-spherical particles

When an incompressible fluid percolates through a static, packed bed with constant interstitial velocity $\vec{u}_f$, the total, average fluid-particle interaction force that acts on each particle located in volume V can be expressed as:

$$<\vec{F}_{tot}> = \frac{-\phi V}{N}\nabla P + <\vec{F}'_d> \tag{3.11}$$

where ∇P is the pressure gradient over the volume, ϕ is the solid volume fraction, N is the number of particles in the volume and $\langle\vec{F}'_d\rangle$ is the average drag force due to fluid-solid interactions. Here, $\langle\vec{F}_{tot}\rangle$ is calculated as $\frac{1}{N}\sum_{i=1}^{N}\vec{F}_{tot,i}$, where $\vec{F}_{tot,i}$ is the total force acting on the i-th particle in the computational volume. Since the fluid is forced to move with a constant velocity, a force balance over volume V gives $-V\nabla P = N\langle\vec{F}_{tot}\rangle$. Substituting $-V\nabla P = N\langle\vec{F}_{tot}\rangle$ into equation (3.11) we obtain an

expression for $\langle \vec{F}'_d \rangle$, viz. $\langle \vec{F}'_d \rangle = (1 - \phi)\langle \vec{F}_{tot} \rangle$. In this work, the Reynolds number is

based on the volume equivalent diameter of the particle, viz. $\mathrm{Re} = \rho_f |\vec{U}| d_V / \mu_f$ (ρ_f

and μ_f are density and dynamic viscosity of the fluid, respectively. $\vec{U}$ is the

superficial velocity of the fluid, viz. $\vec{U} = (1 - \phi)\vec{u}_f$). The average drag force ($\langle \vec{F}'_d \rangle$)

is normalized by the Stokes drag ($3\pi\mu_f \vec{U} d_V$), viz. $F_d = \langle \vec{F}'_d \rangle / 3\pi\mu_f \vec{U} d_V$ (Di Felice,

1995).

A common approach to include particle shape in a drag force correlation, is by introducing a shape factor into e.g. the Ergun (1952) equation (Li et al., 2011; Nemec et al., 2005; Liu et al., 1994). It should be noted that the characteristic size of the particles used in the Ergun equation (1952) is the Sauter diameter. Therefore, the coefficients A and B in equation (3.12) are $150/\Phi^2$ and $1.75/\Phi$, respectively, if the volume equivalent sphere diameter is chosen as the characteristic size of the particle.

$$F_d(\phi, \mathrm{Re}) = A \frac{\phi}{18(1-\phi)^2} + B \frac{\mathrm{Re}}{18(1-\phi)^2} \tag{3.12}$$

In many applications, the particles are assumed to be spheres, viz. $\Phi = 1$. Li & Ma (2011) proposed a drag force correlation for non-spherical particles (hollow spheres, cylinders) by simply replacing the Sauter diameter with the product of a sphericity factor and the Sauter diameter (Φd_s) in the Ergun equation. In this case, the A and B in Eq. (3.12) are equal to $150/\Phi^4$ and $1.75/\Phi^2$, respectively. Comparing the predictions of the modified Ergun equation (Li & Ma, 2011) with the experimental measurements of Li & Ma (2011), a good agreement was observed for high Reynolds numbers and high packing fractions. However, the modified Ergun equation over-predicts the pressure drop for low Reynolds numbers.

Due to the lack of drag force correlations for assemblies of non-spherical particles that span a wide range of Reynolds numbers and solid fractions, numerical simulations of gas-fluidized beds have been restricted largely to beds containing spherical particles. Indeed, only very few efforts that model fluidized beds containing non-spherical particles have been reported so far. In one of these studies, Hilton et al. (2010, 2011) modified the drag force correlation of Hölzer et al. (2008) with a voidage-dependent expression of Di Felice (1994) to model non-spherical particle assemblies of ellipsoids and cuboids, viz:

$$F_d = \frac{Re}{24} c_d \varepsilon^{-3.7+0.65\exp[-\frac{1}{2}(1.5-\log \mathrm{Re})^2]} \tag{3.13}$$

where c_d is given by equation (3.10). Equation (3.13) relies on the assumption that the dependence of F_d on voidage is independent of particle shape. This, however, is probably an over-simplification, as Kriebitzsch et al., (2013) showed that the functional form of the voidage dependence of the drag force acting on individual particles is highly affected by the local packing structure which in turn is affected by particle shape. One of the very few drag force correlations that were derived numerically for assemblies of non-spherical particles of a specific shape (i.e. assemblies of approximately cubic particles constructed from eight identical spheres) was proposed by Chen et al. (2015):

$$F_d(\phi, \text{Re}) = \frac{10\phi}{(1-\phi)^2} + \frac{10\phi}{1-1.14\phi^{0.3}} + \frac{0.413\,\text{Re}}{24(1-\phi)^2}\left[\frac{-0.058(1-\phi)^{-4} + 2.16(1-\phi) + 23\phi(1-\phi) + 8.4\,\text{Re}^{-0.343}}{1 + 10^{3\phi}\,\text{Re}^{(-0.5-2\phi)}}\right] \tag{3.14}$$

In this equation, the orientation of the non-spherical particles (with respect to the fluid flow) is, however, not considered. Indeed, this information would not be available for Euler-Euler simulations. The disadvantage of the correlation of Chen et al. (2015) is that cubes are approximated by 8 spheres of equal size. However, in recent years, an increasing number of studies focusing on alternative non-spherical particle representations that avoid the use of assemblies for spheres has been reported. One increasingly popular approach is the use of the super-quadric equation (Lu et al., 2012, 2014, 2015, 2017). Thus, this paper is concerned with the development of a drag force correlation for assemblies of cubes that are described by the super-quadric equation. The fluid flow is modelled using a lattice Boltzmann method. The effect of the solid volume fraction and the Reynolds number on the drag force is studied in detail and incorporated into the new correlation. The new drag force correlation proposed here is suitable for both Euler-Euler and Euler-Lagrangian simulations of gas-fluidized beds comprised of super-quadric cubes.

3.4 Simulation method

In the simulations reported here, a lattice Boltzmann method (LBM) (Ladd, 1994a) was applied to resolve the flow around the moving particles. The lattice Boltzmann equation (LBE) using a single relaxation time is used in the present work, viz.

$$f_i(\vec{x} + \vec{e}_i \Delta t, t + \Delta t) = f_i(\vec{x}, t) - \frac{\Delta t}{\tau}[f_i(\vec{x}, t) - f_i^{eq}(\vec{x}, t)] \tag{3.15}$$

where f_i is the single particle distribution function with velocity $\vec{e}_i$ at the position $\vec{x}$ and time t, f_i^{eq} is the discrete equilibrium distribution and τ is the single relaxation time. For the three-dimensional D3Q19 model, the lattice velocities are

$$\vec{e}_i = \begin{cases} (0,0,0), & i = 0 \\ (\pm 1, 0, 0)c, (0, \pm 1, 0)c, (0, 0, \pm 1)c, & i = 1...6 \\ (\pm 1, \pm 1, 0)c, (\pm 1, 0, \pm 1)c, (0, \pm 1, \pm 1)c, & i = 7...18 \end{cases} \tag{3.16}$$

with c being the ratio of Δx to Δt. The discrete equilibrium distribution function is

$$f_i^{eq} = w_i \rho_f(\vec{x},t)[1 + 3\frac{\vec{e}_i \cdot \vec{u}_f(\vec{x},t)}{c^2} + \frac{9}{2}\frac{(\vec{e}_i \cdot \vec{u}_f(\vec{x},t))^2}{c^4} - \frac{3}{2}\frac{\vec{u}_f^2(\vec{x},t)}{c^2}]$$

$$w_i = \begin{cases} \dfrac{1}{3}, & i = 0 \\ \dfrac{1}{18}, & i = 1...6 \\ \dfrac{1}{36}, & i = 7...18 \end{cases} \tag{3.17}$$

where $\vec{u}_f(x,t)$ is the velocity of the fluid. The macroscopic properties of the fluid are obtained as follows:

$$\rho_f(\vec{x},t) = \sum_i f_i(\vec{x},t)$$

$$\rho_f(\vec{x},t)\vec{u}_f(\vec{x},t) = \sum_i f_i(\vec{x},t)\vec{e}_i \tag{3.18}$$

The viscosity is given by:

$$\nu = \frac{1}{6}c^2(2\tau - \Delta t) \tag{3.19}$$

An immersed moving boundary condition (Noble and Torczynski, 1998) is employed to enforce the non-slip boundary condition at the surface of the particles. Here, the LB equation is modified to account for the interaction between the solid and gas phases:

$$f_i(\vec{x} + \vec{e}_i \Delta t, t + \Delta t) = f_i(\vec{x},t) - \frac{\Delta t}{\tau}(1-B)[f_i(\vec{x},t) - f_i^{eq}(\vec{x},t)] + B\Omega_i^p \tag{3.20}$$

where B is a weighting function that depends on the local solid volume fraction for each lattice covered by particles and relaxation time, i.e.

$$B(\phi_x,\tau) = \frac{\phi_x(\dfrac{\tau}{\Delta t} - \dfrac{1}{2})}{(1-\phi_x) + (\dfrac{\tau}{\Delta t} - \dfrac{1}{2})} \tag{3.21}$$

where ϕ_x is the local solid volume fraction at position $\vec{x}$ and Ω_i^p is an additional collision term that bounces back the non-equilibrium part of the distribution:

$$\Omega_i^p = f_{-i}(\vec{x},t) - f_i(\vec{x},t) + f_i^{eq}(\rho_f(\vec{x},t),\vec{u}_p(\vec{x},t)) - f_{-i}^{eq}(\rho_f(\vec{x},t),\vec{u}_f(\vec{x},t)) \tag{3.22}$$

Here, $\vec{u}_p(x,t)$ is the particle velocity at position $\vec{x}$ and time t (-i denotes the distribution component which has the opposite direction to i).

3.5   Validation of the lattice Boltzmann method

Prior to simulating assemblies of non-spherical particles, the LBM code   was validated comprehensively for spheres using three different flow conditions (Chen et al., 2015): (1) Comparison of the drag coefficient of a single sphere in an uniform flow with the correlation of Bird et al. (2007); (2) Comparison of the total force acting

on a cubic array of spheres in a creeping flow with the results of Hasimoto (1959); (3) Comparison of the drag force of a random assembly of spheres for Reynolds numbers up to 209.9 with the results reported by van der Hoef et al. (2005) and Beetstra et al. (2007). In the current work, the non-spherical particles are represented using the super-quadric equation (equation (3.23)). Figure 3.1 shows snapshots of super-quadric particles that are obtained by varying the parameters *a*, *b*, *c* and *m* in equation (3.23).

$$\left(\frac{x}{a}\right)^{m} + \left(\frac{y}{b}\right)^{m} + \left(\frac{z}{c}\right)^{m} = 1 \tag{3.23}$$

Super-quadric cube   Prolate   Oblate

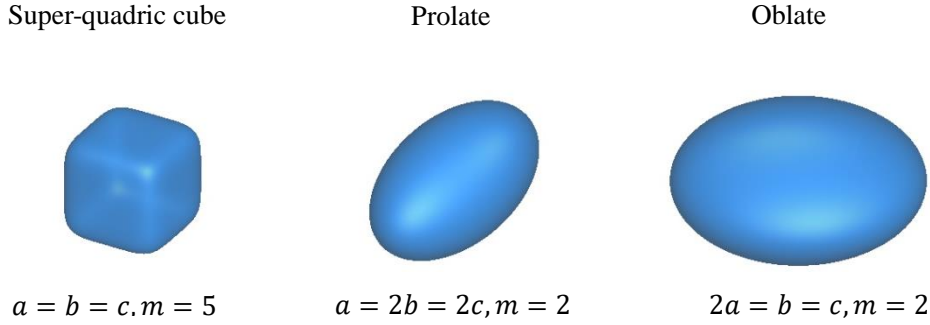$a = b = c. m = 5$ $a = 2b = 2c, m = 2$ $2a = b = c, m = 2$

Figure 3.1. Differently-shaped super-quadric particles.

Next, our LBM simulations were validated by comparing the drag coefficients of single cubes and spheroids in an uniform flow with the data reported by Richter et al. (2012). Richter et al. (2012) calculated the drag coefficients of spheres, prolate spheroids and cubes using a commercial finite volume solver (ANSYS FLUENT). For the prolate (a = 2b = 2c) two different orientations with respect to the flow direction, i.e. its major axis is parallel (prolate 1) or perpendicular (prolate 2) to the flow, were modelled. The major axis of the cube (a = b = c) was parallel to the flow.   The value of *b* was 5 lattice units for Re ≤ 50, whereas 8 lattice units were used for Re > 50.

The drag coefficient of the particle is defined as: $c_d = 8|\vec{F}_d'|/\rho_f \pi d_V^2 \vec{U}^2$. The domain size was $20b \times 20b \times 20b$ and $\nu = 0.01$. Figure 3.2 shows a comparison between our LBM data and the simulation results of Richter et al. (2012) together with the predictions of Eqs. (3.8), (3.9) and (3.10). Our LBM data agrees very well with the simulations of Richter et al. (2012). The blue lines plot the drag coefficient of a cube as predicted by Eqs. (3.8) and (3.9). The solid lines plot the drag coefficients of prolate 1, the cube and prolate 2 as predicted by Eq. (3.10). The predictions of equations (3.8) and (3.9) are slightly below our LBM results. In general, the agreement is good since equations (3.8) and (3.9) are valid for differently-shaped particles and a wide range of Reynolds numbers. On the other hand, equation (3.10) can predict accurately the drag coefficient of a single cube and prolates in uniform flows. Compared to Eqs. (3.8) and (3.9), Eq. (3.10) is easier to implement and more accurate. Our LBM model was validated further by simulating an oblate spheroid

rotating in a shear flow. The shear flow was generated by two parallel walls moving in opposite directions. The computational domain was $200 \times 80 \times 40$ and the semi-axes of the oblate were 16, 16 and 8. Figure 3.3 plots the period of the tumbling motion of the oblate spheroid as a function of the Reynolds number. The tumbling period scales as a function of Re with $T = 200 \times (80 - Re)^{-0.5}$. This result is very close to the predictions of Aidun et al. (1998) ($T = 200 \times (81 - Re)^{-0.5}$). We conclude that the lattice Boltzmann method reported here reproduces accurately a series of reference simulations.
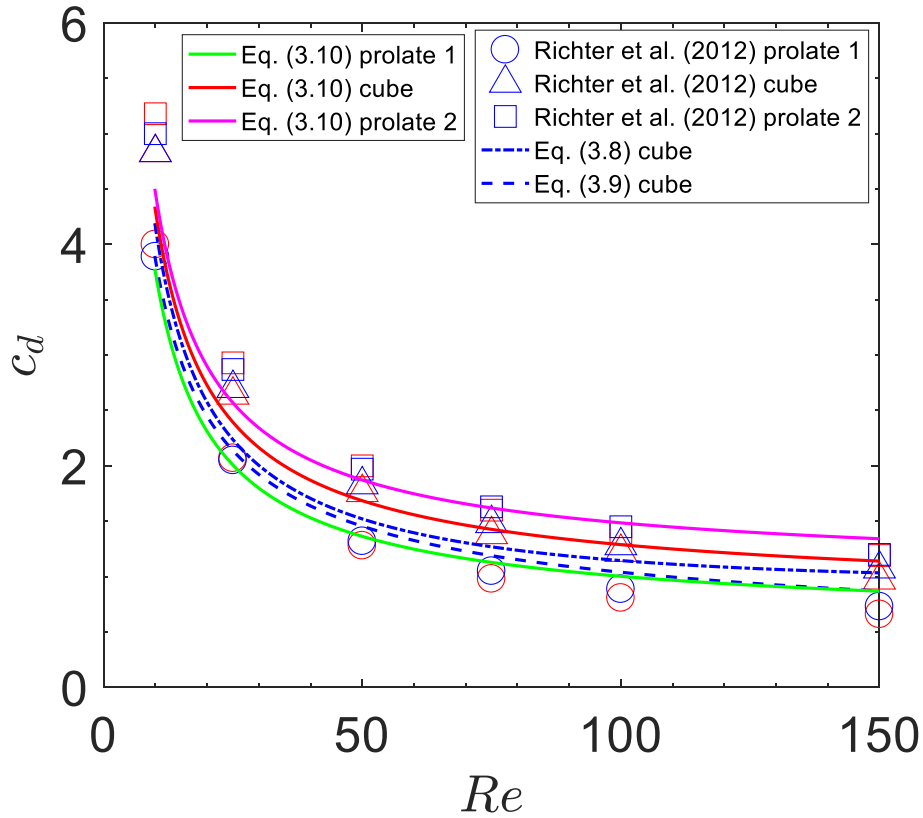

Figure 3.2. Drag coefficients of different, non-spherical particles (individual particles) as a function of the Reynolds number. The red symbols show the results of the LBM simulation.
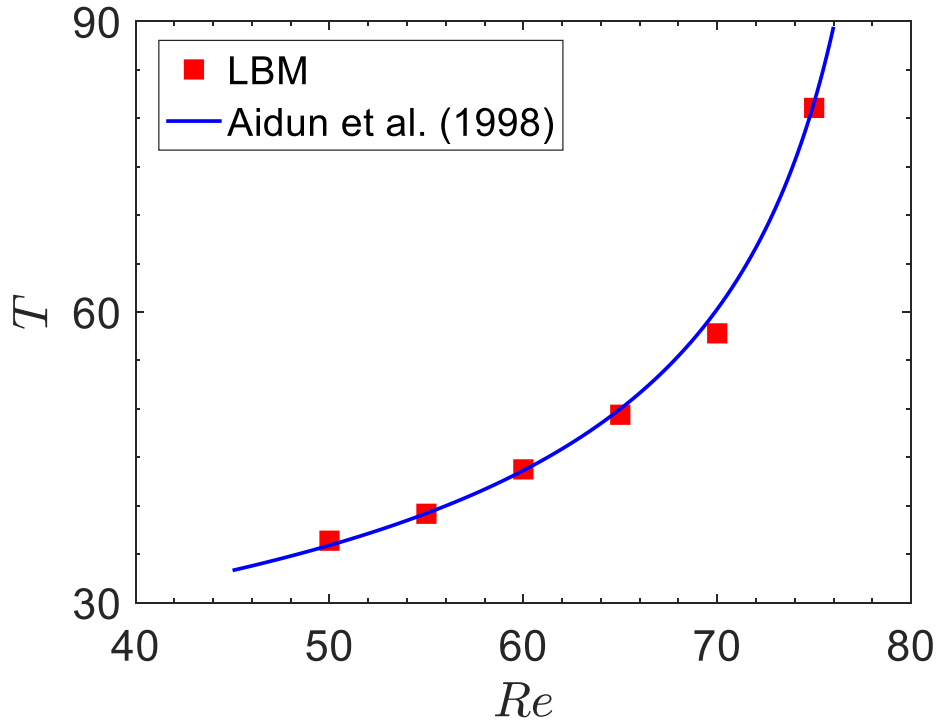
Figure 3.3. Tumbling period of an oblate spheroid in a shear flow as a function of Reynolds number.

3.6 Simulations and Results

3.6.1 Simulation setup

In this work packings of cubes were generated by randomly distributing super-quadric cubes in cubic, periodic domains. Several methods have been proposed to generate random packings of spheres, e.g. sequential addition or collective rearrangement (Liu et al., 1999). However, there is no clear definition of a random packing of cubes available. Thus, here we assumed that configurations generated by a Monte Carlo method (Frenkel and Smit, 1996) are sufficiently random for this work. Specifically, the following method was applied: Initially, all cube centres are placed randomly without any overlap at lattice points with a cube size that is half ($a/2$) of the nominal value of the cube (a). Subsequently the cubes are randomly moved translationally and rotated in a sequential fashion (one cube after another). Simultaneously the size of the cubes is increased by a predetermined increment ($a/1000$). If there is no overlap with another cube at the new position (the particles are allowed to contact with each other), the orientation, coordinates and size of the cube is updated, otherwise the operation is rejected. To this end, the discrete element method for super-quadric shaped particles reported by Lu et al. (2012) was used for overlap detection. After reaching the desired cube size, the randomization is continued but without increasing the size of the cube further until a number of pre-determined time steps (500000 time steps) has been

completed. A sample configuration obtained by this randomization method is shown in Figure 3.4.
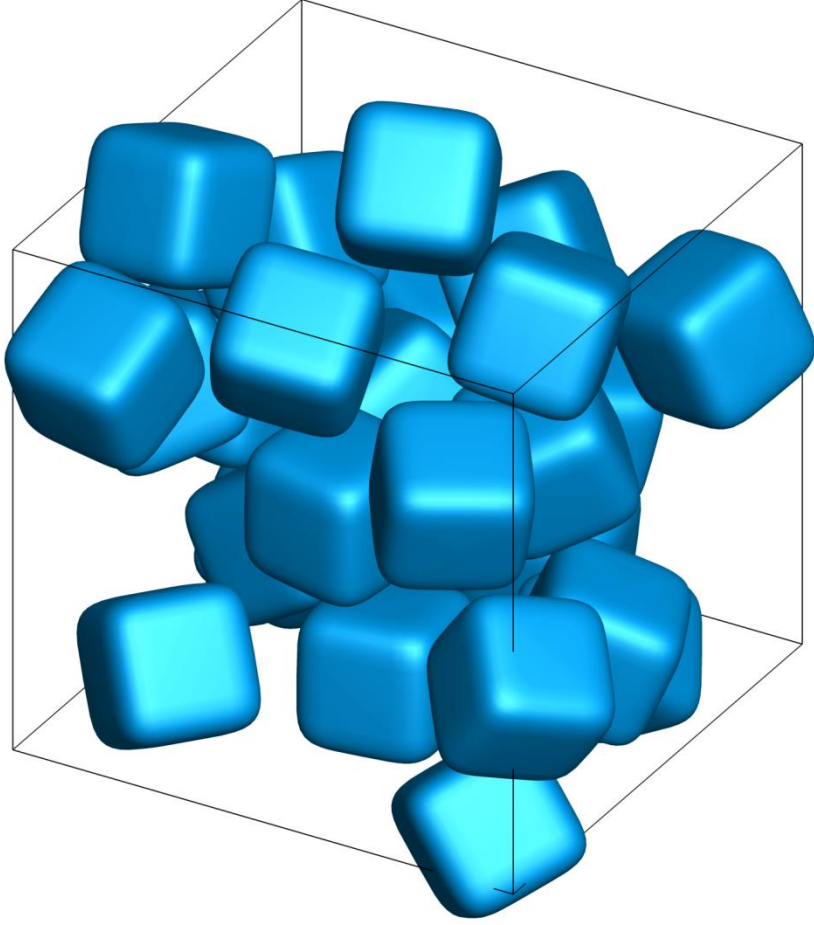
Figure 3.4. An example of a random configuration of super-quadric cubes ($\phi = 0.4$).

In the following all quantities are given in lattice units (l. u.) and the following scaling is applied:

$$u_{phy} = u_{lu}\frac{\Delta x}{\Delta t}, \ d_{V,phy} = d_{V,lu}\Delta x, \ \nu_{phy} = \nu_{lu}\frac{\Delta x^2}{\Delta t} \tag{3.24}$$

The subscript 'phy' denotes physical units. Each simulation contained $N = 25$ cubes and d_V was calculated using the volume of the super-quadric cube. Values for d_V were in the range $17 - 33$ (l. u.). To vary the Reynolds number, Re, viscosities in the range 0.000838 - 0.01 (l. u.) were used. The particle velocity was very low (< 0.02[l. u.]) to ensure numerical stability. Periodic boundary conditions were used in all of the directions. All of the particles were moved with a constant velocity $\vec{u}_p$ in the same (arbitrary) direction. Thus, there was no relative motion between the individual cubes. A uniform force which induces a backflow velocity $\vec{u}_f$ was applied to the fluid phase such that the total momentum of the fluid was zero (Van der Hoef et al., 2005), viz.

$$\rho\phi\vec{u}_p V + \rho(1-\phi)\vec{u}_f V = 0 \tag{3.25}$$

Taking the particles as a fixed reference frame, we obtain the superficial velocity of the fluid as

$$\vec{U} = -\vec{u}_p \qquad (3.26)$$

After reaching a steady state, the force acting on the cubes was averaged over 30000-200000 time steps. For each Reynolds number and solid fraction, 12-18 different configurations were modelled and the values obtained were averaged. In this work, we did not include the data which deviated more than three times the standard deviation from the mean value.
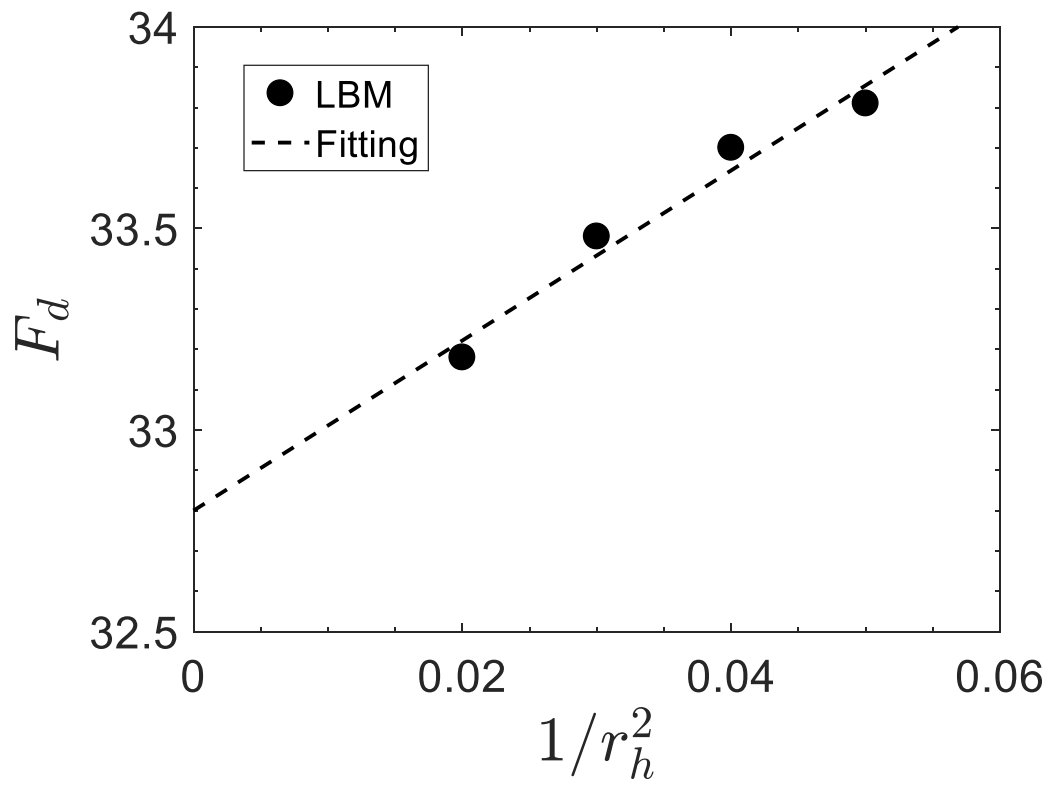
3.6.2 Drag force acting on assemblies of super-quadric cubes

To probe the influence of the (finite) grid resolution on the calculated drag force, a set of simulations that use different grid resolutions for identical particle configurations was performed (the particle size was kept constant). The hydraulic radius that was used to estimate the average "pore size" of the interstices between spherical particles in a packed bed (van der Hoef, 2005) is defined as: $r_h = d(1-\phi)/6\phi$. If r_h is small, it may not be sufficient to fully resolve the fluid flow around the particles. Increasing the diameter of the particle (d) in lattice units, increases the hydraulic radius in lattice units. Van der Hoef et al. (2005) found that the average drag force acting on assemblies of spheres scales with $1/r_h^2$.

Here, analogous to spheres, we define the hydraulic radius for cubes using the volume equivalent diameter, viz. $r_h = d_V\Phi(1-\phi)/6\phi$. In Figure 3.5, the average drag force acting on cubes (identical particle configuration) as a function of $1/r_h^2$ (Re = 100) is plotted for different grid resolutions (d_V). We observe that also the drag force acting on cubes scales with $1/r_h^2$ (for solid fractions of ϕ=0.3 and 0.4). In figure 3.5 (a), the largest value of r_h modelled implies that the flow around cubic particles is resolved on average by 8 lattice points. The difference in F_d between the largest r_h and $r_h \to \infty$ is 0.9% (Figure 3.5(a)). When the drag force is extrapolated to an infinite resolution, i.e. $1/r_h^2 \to 0$, the "correct" drag force is obtained. Therefore, for each configuration, simulations with three different values of r_h were performed and the drag force was extrapolated to the case of infinite resolution using a linear relationship between F_d and $1/r_h^2$. Interestingly, for $\phi = 0.45$ (Fig. 3.5), the drag force is independent of $1/r_h^2$ which implies that the drag force has reached its asymptotic value already with the grid resolutions employed ($d_V > 30$ in lattice units). Therefore, for $\phi = 0.45$ the values of F_d obtained for different values of r_h were averaged to obtain F_d for each configuration. For ϕ=0.1 and 0.2, the difference in F_d for $d_V \approx 20$ and $d_V \approx 30$ is within 1.5% (Re=200). Hence, it is not necessary to extrapolate the drag force to infinite resolution when $d_V > 20$ was used for ϕ=0.1 and 0.2 in the simulations.

(a) $\phi = 0.3$

(b) $\phi = 0.4$
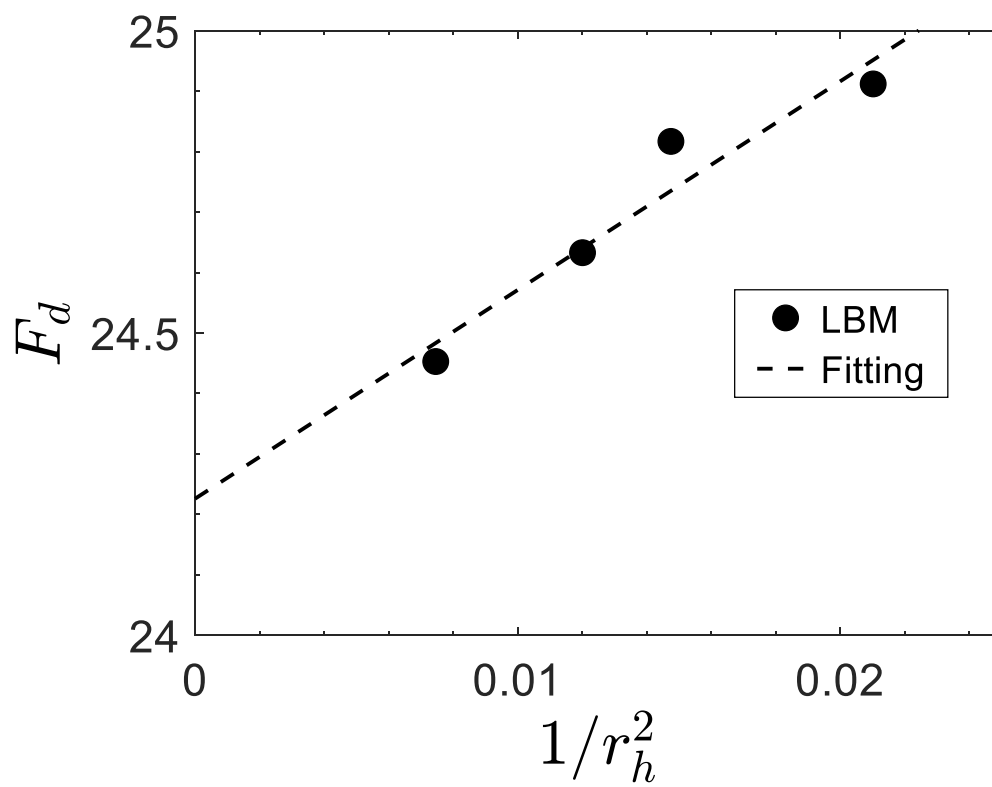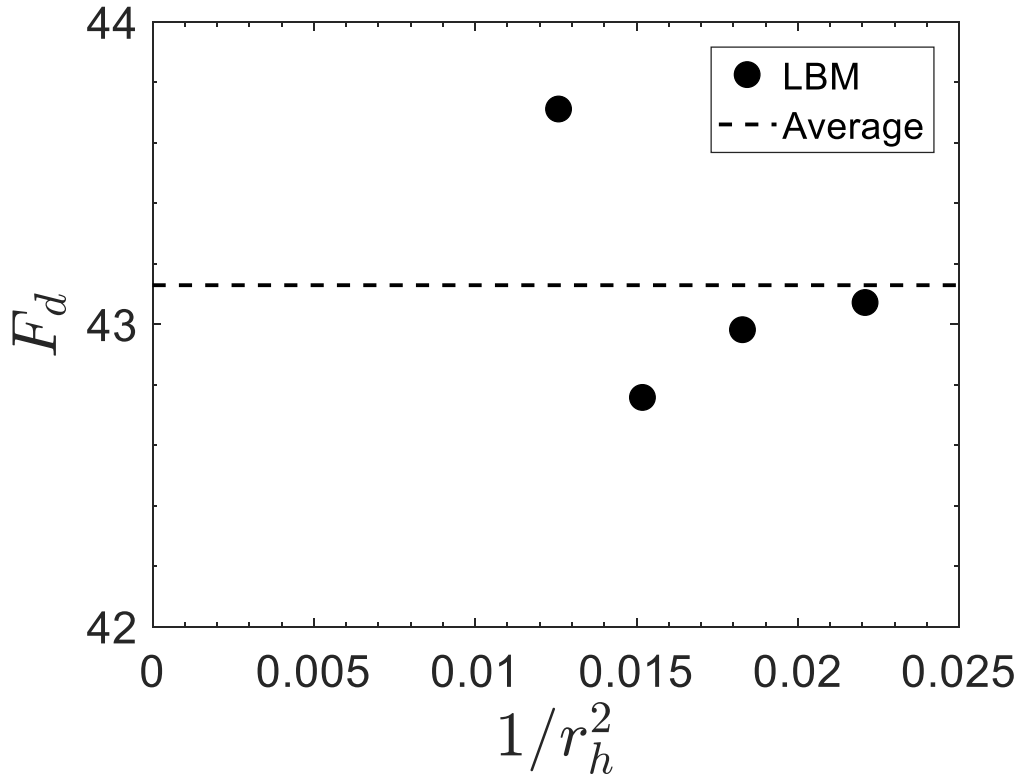
(c) ϕ = 0.45

Figure 3.5. Average, normalized drag force acting on a single particle in an assembly of super-quadric cubes as a function of $1/r_h^2$ for Re=100. The kinematic viscosity was ν = 0.00427.

In Figure 3.6, we compare our simulation data with the Ergun equation (1952) and the modified Ergun equation (Li & Ma, 2011). The inherent shortcoming of the experimentally-derived Ergun correlation (and correlations based on it) is its restriction to dense packings, although, in practice the Ergun equation is used often to calculate the drag force over a large range of solid volume fractions (Gidaspow, 1994). In addition, even for dense packings, three different regimes were identified (Fand et al., 1987), i.e. Darcy regime Re<2.3, Forchheimer regime 5<Re<80, turbulent regime Re>120 and the transition regions in between them. For each regime, the coefficients A and B were derived separately by fitting, e.g. A=192.24 and B=0 for Re<2.3. Hence, one set of values for A and B is not expected to predict accurately the drag force for dense packings over a wide range of Reynolds numbers. Compared to our simulation data, both the Ergun and the modified Ergun equations over-predict significantly the drag force for super-quadric cubes at high Reynolds numbers, while under-predicting the drag force in the Stokes regime. As pointed out before, the experimental data used to correlate the Ergun equation comprise pressure drop measurements of packed beds containing also non-spherical particles (e.g. round sand, cylinders, etc.). It should be noted, that the prediction of the Ergun equation for the drag force for assemblies of spheres are significantly higher than the predictions of numerically derived

correlations (e.g. Hill et al., 2001b; Beetstra et al., 2007; Tenneti et al., 2011) (Tenneti et al., 2011). Since the shape of a super-quadric cube ($\Phi = 0.9559$) is close to a sphere, it is possible that the Ergun equation over predicts the drag force for assemblies of super-quadric cubes. The modified Ergun equation proposed by Li & Ma (2011) was based on pressure drop measurements in packed beds that contained hollow spheres or cylinders (only four differently shaped particles were used in the experiments). Since the shape of a super-quadric cube is significantly different from that of a hollow sphere or cylinder, it is not overly surprising that there is an appreciable difference between the equation proposed by Li & Ma (2011) and our numerical data. Following Li & Ma's method (2011), we re-fitted Eq. (3.12) using our simulation data to assess whether an Ergun-type equation could represent well our data. Eq. (3.27) was obtained for assemblies of super-quadric cubes (the coefficients A and B are equal to, respectively, $213.7/\Phi^4$ and $1.13/\Phi^2$ with $\Phi = 0.9559$). Figure 3.7 plots the normalized average drag force of assemblies of super-quadric cubes predicted by Eq. (3.27). Due to the linear dependence of Eq. (3.27) on the Reynolds number, the relative deviation between Eq. (3.27) and our LBM data is high for low Reynolds numbers. The maximum relative deviation is 22 %. One possible solution to increase the accuracy of an Ergun-type equation is to identify different flow regimes, and then determine coefficients A and B for each regime separately. However, such an approach is probably of very little practical use. An alternative approach is to adopt a non-linear Reynolds number dependency of F_d such as Eq. (3.14) or Beetstra et al. (2007).

$$F_d(\phi, \text{Re}) = \frac{213.7}{\Phi^4} \frac{\phi}{18(1-\phi)^2} + \frac{1.13}{\Phi^2} \frac{\text{Re}}{18(1-\phi)^2} \qquad (3.27)$$

Although implemented in CFD-DEM simulations of gas-fluidized beds comprising non-spherical particles (e.g. cubes, cylinders) (Hilton et al., 2010; Zhou et al., 2011; Oschmann et al, 2014), the validity of Eq. (3.13) was not yet assessed explicitly by experiments or direct numerical simulations. Figure 3.8 compares the predictions of equations (3.13) and LBM data for ϕ=0.2 and 0.45. For a solid volume fraction and a Reynolds number, the drag force acting on individual cubes in six different configurations is calculated using Eq. (3.13). In Figure 3.8, we observe that Eq. (3.13) under-predicts the drag force for assemblies of super-quadric cubes. The discrepancy between Eq. (3.13) and the LBM data is most likely due to the fact that the exponent of the voidage term in Eq. (3.13) was derived originally for assemblies of spheres. At low Reynolds numbers, the relative deviation between Eq. (3.13) and the LBM data is up to 50%. Therefore, the error of Eq. (3.13) in predicting the drag force for assemblies of super-quadric cubes is substantial.

The predictions of the drag force correlations of Tang et al. (2015), Chen et al. (2015) and our LBM data are compared in Figure 3.9. The equation of Tang et al. (2015) was proposed originally for assemblies of spheres. From figure 3.11, we can see that the drag force acting on assemblies of super-quadric cubes and volume equivalent spheres

is comparable. For ɸ = 0.1, Tang's equation agrees well with our LBM data. However, the difference between our LBM data and the equation of Tang et al. (2015) increases with increasing solid volume fraction and Reynolds number. Somewhat surprisingly, we observe that the difference in the drag force between super-quadric cubes and approximately cubic particles constructed from eight spheres (Eq. (3.14)) is substantial. The reason for this very large difference is probably that fluid can flow through the "cubes" constructed from eight spheres, which increases appreciably the contact surface area of the fluid. From the comparisons above, it is clear that the drag force is significantly affected by particle shape. It seems that only for relatively small Reynolds numbers (Re<10) super-quadric cubes can be approximated by volume equivalent spheres. At higher Reynolds numbers, this approximation would induce a large error (up to 56%) in estimating the gas-solid interaction and lead, in turn, to large errors in modelling the dynamics of e.g. gas-solid fluidized bed. Hence, correlating our LBM data, we propose Eq. (3.28) to model accurately the drag force for assemblies of super-quadric cubes. The first two terms of equation (3.28) describe the contribution of viscous forces to the drag force. The functional form of the second term is based on an expression for low Reynolds numbers that was initially proposed by van der Hoef et al. (2005). The third term is a modification of the inertial contribution to the drag force as proposed by Beetstra's (Beetstra et al., 2007). Figure 3.10 plots the LBM-derived normalized drag force acting on random assemblies of super-quadric cubes as a function of the Reynolds number. Equation (3.30) represents the simulation data pretty well.

$$F_d(\phi, \text{Re}) = \frac{10\phi}{(1-\phi)^2} + (1-\phi)^{0.5}(-0.2 + 5.6\phi^{0.5}) + \frac{0.413\,\text{Re}}{24(1-\phi)^2}[\frac{-1.17(1-\phi)^{-1} + 0.45\phi(1-\phi) + 8.4\,\text{Re}^{-0.15+0.24\phi}}{1+10^{2\phi}\,\text{Re}^{(-0.5-2\phi)}}]$$

(3.28)
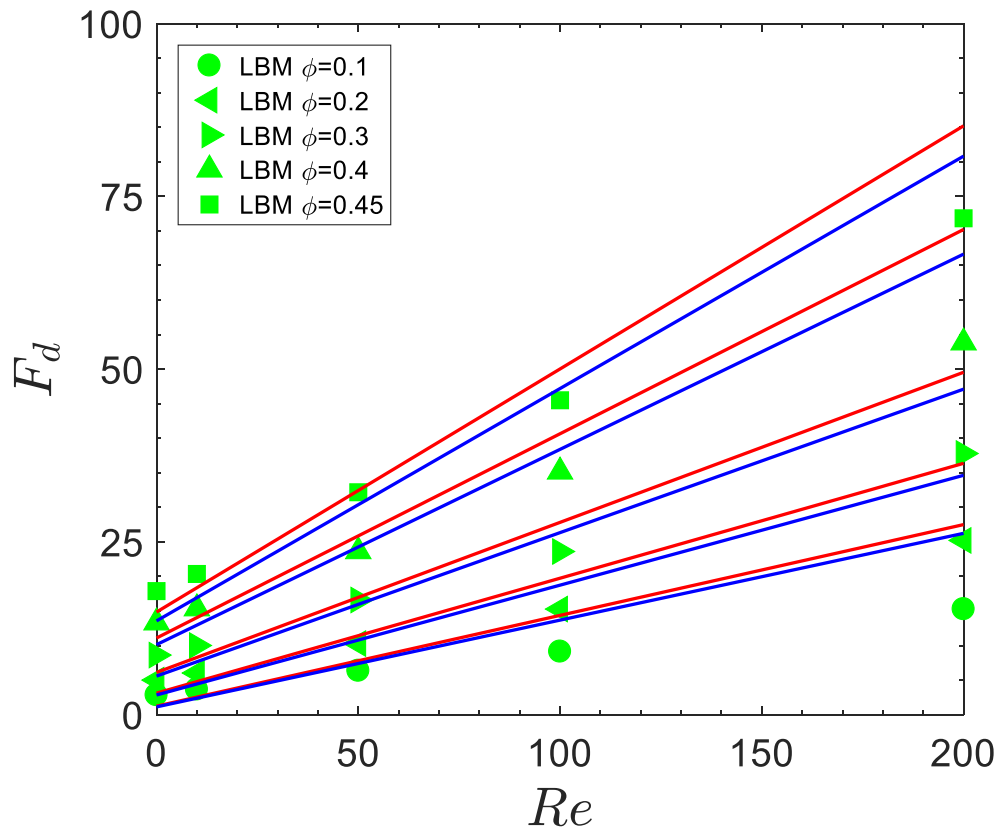
Figure 3.6. Normalized drag force as a function of Reynolds number. The data points plot the LBM data, whereas the blue and red lines represent the Ergun and the modified Ergun equation (Li & Ma, 2011), respectively.
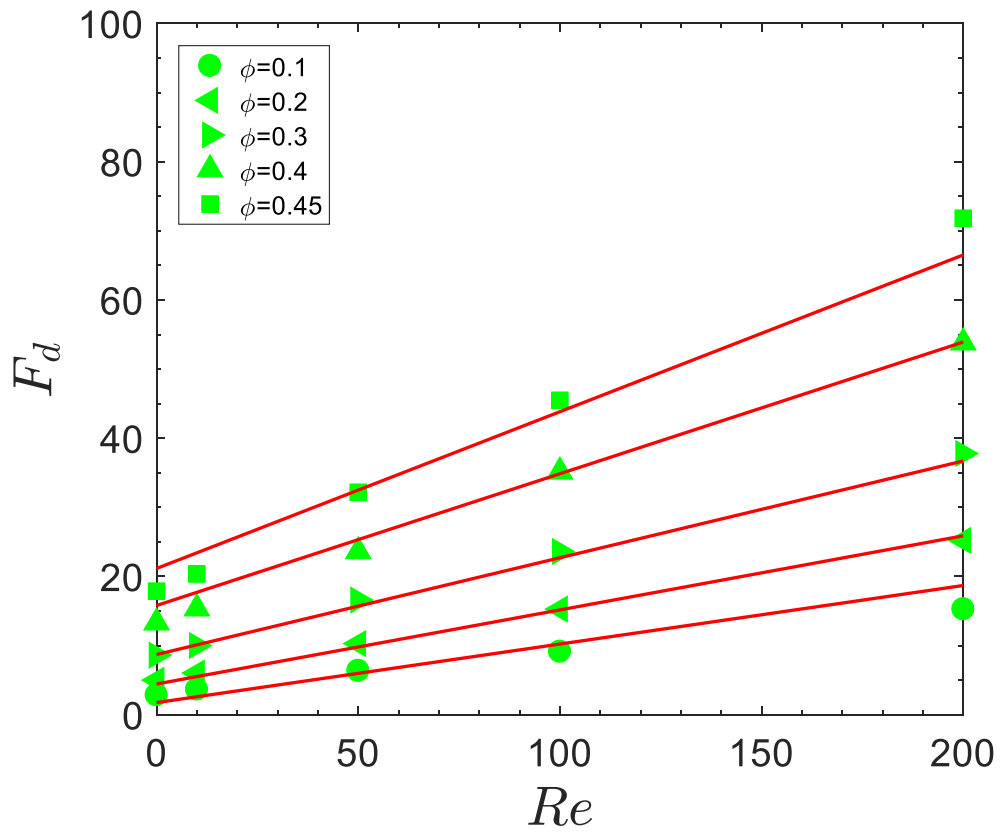
Figure 3.7. Comparison of the normalized drag force predicted by Eq. (3.27) and the LBM data obtained in this work.
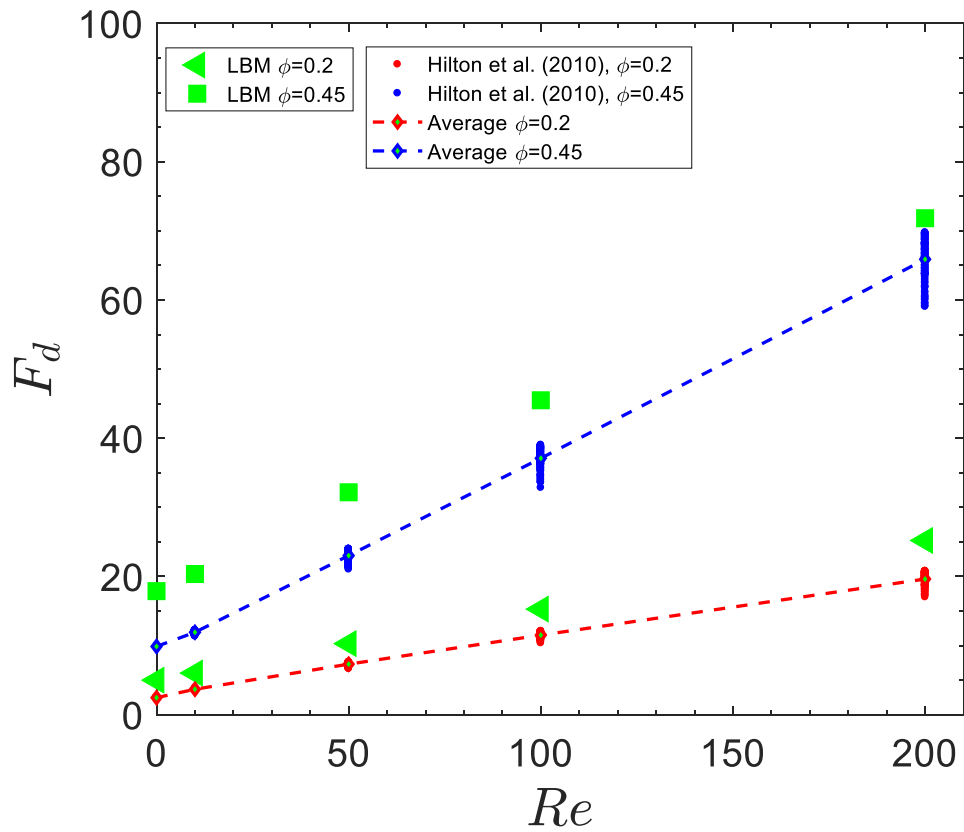
Figure 3.8. Comparison of the LBM data and Eq. (3.13) (Hilton et al., 2010) for φ=0.2, 0.45. The dashed lines represent the average drag force for cubes calculated using Eq. (3.13). The squares and triangles plot the LBM data.
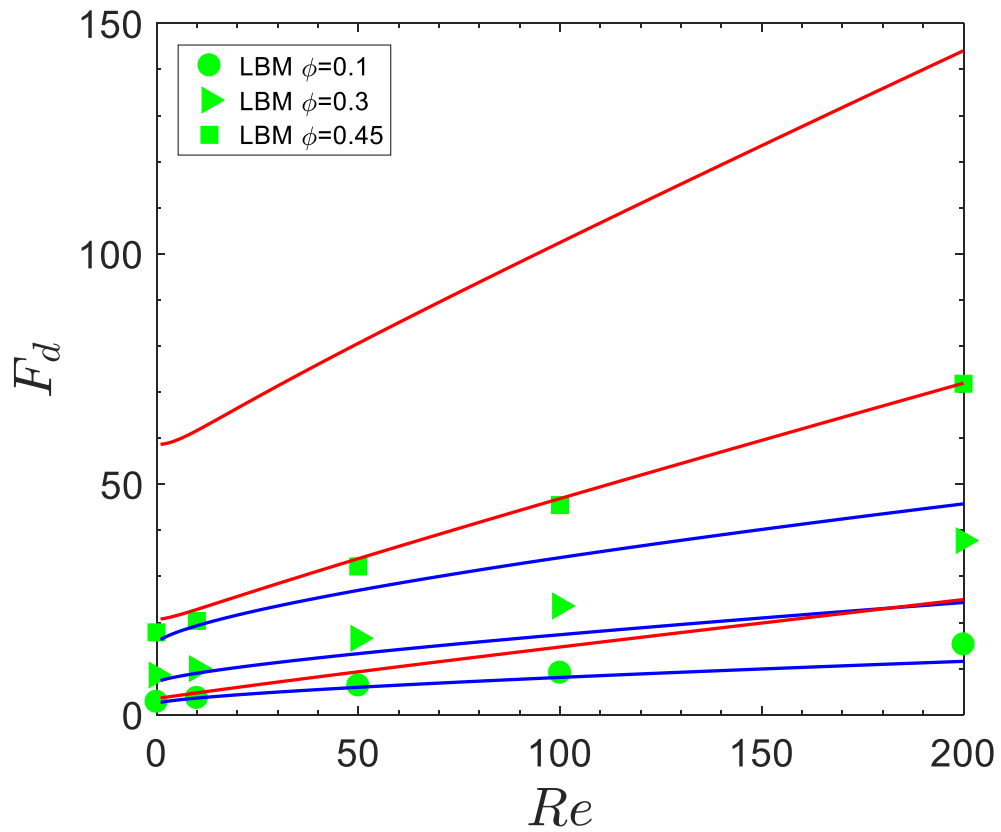
Figure 3.9. Drag force for assemblies of spheres, approximately cubic particles constructed from eight identical spheres and super-quadric cubes as a function of Reynolds number. The blue and red lines plot the correlations of Tang et al. (2015) and Eq. (3.14), respectively.
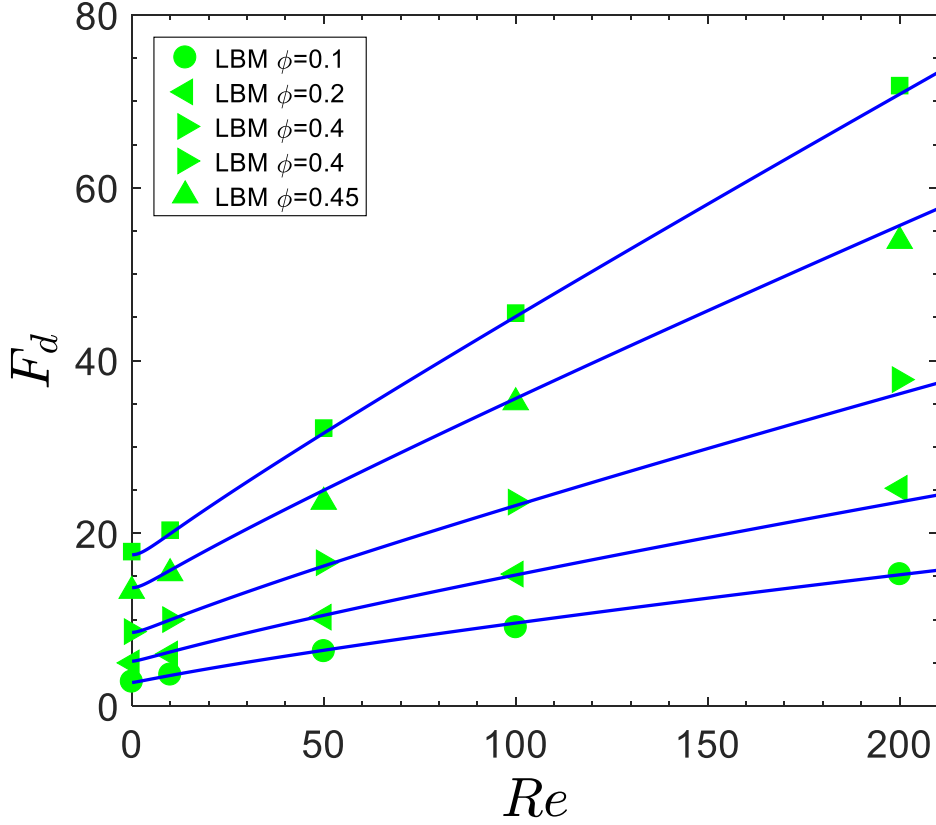
Figure 3.10. Normalized drag force as a function of Reynolds number. The green symbols represent the LBM simulation results. The lines plot the predictions of equation (3.28).

3.7 Conclusions

The lattice Boltzmann method has been used to compute the drag force acting on assemblies of super-quadric cubes for a wide range of solid volume fractions and Reynolds numbers. Correlating our simulation data we propose a new drag force correlation for super-quadric cubes. We have compared the drag forces calculated here with those predicted by the Ergun equation (1952) and the correlations proposed for assemblies of spheres (Tang et al., 2015) and assemblies of non-spherical particles (Li & Ma, 2011; Chen et al., 2015; Hilton et al., 2010). The correlations proposed by Li & Ma (2011) and Chen et al. (2015) over-predict the drag force for super-quadric cubes in particular for high solid volume fractions and Reynolds numbers. Hence, a general drag force correlation for assemblies of non-spherical particles or a drag force correlation derived from a coarse level representation of non-spherical particles (e.g. constructed by few identical spheres) is currently associated with a large error. The correlation used by Hilton et al. (2010) under-predicts the drag force for super-quadric cubes. Despite the fact that Eq. (3.10) is accurate to estimate the drag coefficients of individual cubes and prolates, the reason for the under-prediction of the drag force of assemblies of super-quadric cubes is the fact that the exponent of the voidage

dependence in Eq. (3.13), originally derived for assemblies of spheres, is not suitable to describe accurately the effect of the solid volume fraction on the drag force for cubes. Interestingly, the Ergun equation (1952) shows appreciable differences with our LBM data for both low and high Reynolds numbers for solid volume fractions in the range 0.1-0.45. Our results indicate that it is essential for Euler-Euler and Euler-Lagrangian simulations of cubic particles to implement drag force correlations that are indeed proposed from cubic particle data and not to use correlations that were initially developed for spherical particles. We expect that the correlation proposed here will improve CFD-DEM and Euler-Euler simulations of cubic particles.

4

A Dirichlet boundary condition for thermal lattice Boltzmann method

4.1 Abstract

In this work a thermal boundary condition based on the bouncing back of the non-equilibrium distribution of energy distribution function are presented for thermal lattice Boltzmann simulations that contain a Dirichlet boundary condition. To this end the thermal lattice Boltzmann equation is modified by introducing an additional collision term that takes into account the thermal diffusivity and local solid volume fraction of a lattice (partially) covered by the solid phase. Asymptotic analysis of the boundary condition confirms a second order accuracy of the new boundary condition. The method is validated using an analytical solution for Nusselt number correlation of a single sphere in unbounded stationary fluid and previous direct numerical simulations of fluid particle heat transfer.

4.2 Introduction

Particulate two phase, non-isothermal flows are encountered widely in industrial applications, e.g. gas-fluidized reactors. Understanding the complicated interaction between fluid mechanics and thermal effects are essential to improve the design reactors commonly applied in the chemical industry and improving their efficiency. In the past decades, Computational fluid dynamics (CFD) has been applied extensively to compute the fluid flow, heat transfer and chemical reactions in complex systems, e.g. packed or fluidized reactors. However, the flow structure in these systems spans a wide range of length scales, e.g. from millimeters (particle) to meters (bubble). Freund et al. (2003) simulated single phase reacting flows in a randomly packed bed using lattice Boltzmann method and found that the integral quantities such as pressure drop were significantly influenced by the local packing structure, a feature which was neglected in the CFD simulations. On contrary, in direct numerical simulations (DNS), the flow around individual particles is fully resolved and interactions between fluid and particles are directly taken into account by imposing boundary conditions at the particles' surface. Additionally, DNS has the potential to complement experiments as DNS provides a versatile tool to extract data that is otherwise extremely difficult if not impossible to obtain experimentally. Among the different DNS methods available,

the lattice Boltzmann method has several advantages when compared to conventional numerical methods (Chen & Doolen, 1998) (e.g. Finite volume method): (1) The convective and collision operators are linear; (2) The fluid pressure can be calculated simply by an equation of state; (3) Complex boundaries are relatively easy to implement; (4) ease of parallelization as computations are local.

Recently the extension of LBM to thermal flows has received significant attentions (Yoshida & Nagaoka, 2010; Li et al., 2013; Pareschi et al., 2016; Wang et al., 2016). In general, three different approaches have been proposed: a multispeed model (Alexander et al., 1993), a passive-scalar model (Bartoloni et al., 1993; Shan, 1997), and a double population model (He et al., 1998).

Alexander et al. (1993) developed the multispeed approach which only needs a density distribution function for thermal flows. However, additional speeds are required and equilibrium density distribution functions including higher order velocity terms are necessary so that the temperature can be evaluated at the macroscopic level. Moreover, the model suffers from numerical instability for high Rayleigh number flows and temperature variation in the simulations is limited to a narrow range (McNamara et al., 1995). In the passive-scalar model (Bartoloni et al., 1993; Shan, 1997), the temperature is considered as a passive scalar and simulated using a separate distribution function which is independent of density distribution function. This approach enhances the numerical stability when compared to the multispeed model (Guo et al., 2002). The main disadvantage of passive scalar model is that the viscous dissipation and compression work done by the pressure is not taken into account. He et al. (1998) proposed a double-population model at incompressible limit. The temperature distribution function in double population model is derived directly from the second order moment of density distribution function (internal energy). As a result, the viscous dissipation and compression work done by pressure are involved in the temperature evolution equation. To avoid the implicitness of temperature evolution equation, new variables for temperature evolution equation are introduced. Hence, the temperature evolution equation is transformed to the form of new variables. However, the shortcoming of double population model is that the temperature evolution equation includes temporal and spatial derivatives of macroscopic fluid velocity, which increases the complexity of the implementation. In addition, the bounce back boundary condition for the non-equilibrium distribution of the distribution functions is only valid for the old variables (i.e. density and temperature distribution functions). Peng et al. (2002) proposed a simplified thermal lattice Boltzmann model for incompressible thermal flow which overcomes the shortcomings of double-population model (He et al., 1998), yet maintains the bounce back rule for the thermal boundary

condition. As the work reported here is based on the model proposed by Peng et al. (2002). Equations (4.1) and (4.2) are the density and energy evolution equations, respectively.

$$f_i(\vec{x} + \vec{e}_i \Delta t, t + \Delta t) = f_i(\vec{x}, t) - \frac{\Delta t}{\tau_v}[f_i(\vec{x}, t) - f_i^{eq}(\vec{x}, t)] \tag{4.1}$$

$$g_i(\vec{x} + \vec{e}_i \Delta t, t + \Delta t) = g_i(\vec{x}, t) - \frac{\Delta t}{\tau_c}[g_i(\vec{x}, t) - g_i^{eq}(\vec{x}, t)] \tag{4.2}$$

where f_i and g_i are the density and energy distribution functions with velocity $\vec{e}_i$ at the position $\vec{x}$ and time t, respectively. The superscript 'eq' denotes the equilibrium state, τ_v and τ_c are the single relaxation times related to viscosity and thermal diffusivity, respectively and Δt is the time step applied in the model. The model of Peng et al. (2002) is based on the assumption that the viscous dissipation and compression work done by pressure can be neglected in real incompressible flows. The numerical simulation of natural convection in a square cavity showed that the simplified thermal model had the same accuracy with the model proposed by He et al. (1998). The D3Q19 and D3Q7 lattices (Figure 4.1) for the density and energy distributions are given as follows:

$$\vec{e}_i = \begin{cases} (0,0,0), & i = 0 \\ (\pm1,0,0)c,(0,\pm1,0)c,(0,0,\pm1)c, & i = 1...6 \\ (\pm1,\pm1,0)c,(\pm1,0,\pm1)c,(0,\pm1,\pm1)c, & i = 7...18 \end{cases} \tag{4.3}$$

with c being the ratio of Δx and Δt. The discrete equilibrium density distribution function can be expressed as

$$f_i^{eq} = w_{i,v}\rho_f[1 + 3\frac{\vec{e}_i \cdot \vec{u}_f}{c^2} + \frac{9}{2}\frac{(\vec{e}_i \cdot \vec{u}_f)^2}{c^4} - \frac{3}{2}\frac{\vec{u}_f^2}{c^2}]$$

$$w_{i,v} = \begin{cases} \dfrac{1}{3}, & i = 0 \\ \dfrac{1}{18}, & i = 1...6 \\ \dfrac{1}{36}, & i = 7...18 \end{cases} \tag{4.4}$$

where $\vec{u}_f(x, t)$ is the velocity of the fluid. The discrete equilibrium energy distribution is:

$$g_i^{eq} = w_{i,c} \phi (1 + 4 \cdot \frac{\vec{e}_i \cdot \vec{u}_f}{c^2})$$

$$w_{i,c} = \begin{cases} \dfrac{1}{4}, & i = 0 \\ \dfrac{1}{8}, & i = 1...6 \end{cases} \qquad (4.5)$$

The macroscopic properties such as density, momentum and energy can be obtained through the following summations:

$$\rho_f = \sum_i f_i, \quad \rho_f \vec{u}_f = \sum_i f_i \vec{e}_i, \quad \phi = \sum_i g_i \qquad (4.6)$$

The relationships to obtain the viscosity and thermal diffusivity are:

$$v = \frac{1}{3} c^2 (\tau_v - \frac{\Delta t}{2})$$

$$D = \frac{1}{4} c^2 (\tau_c - \frac{\Delta t}{2}) \qquad (4.7)$$

(a)   (b)

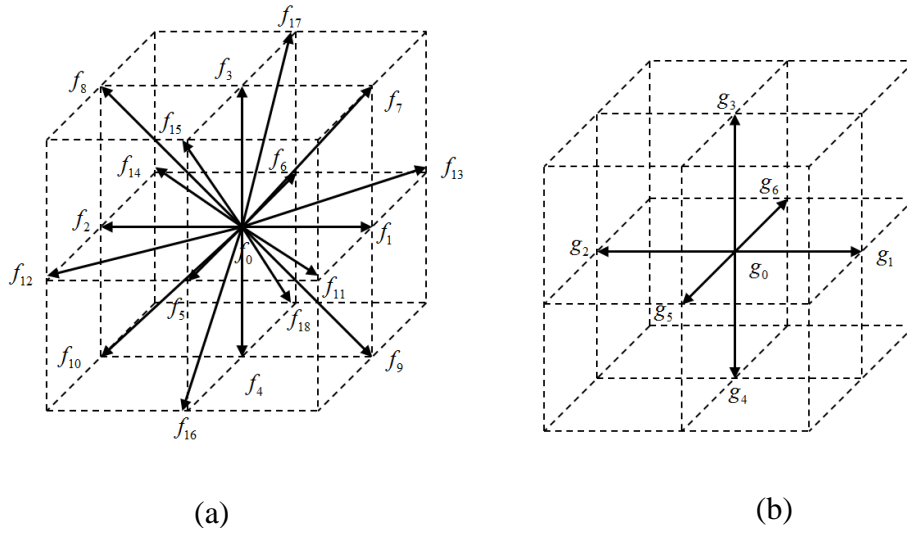Figure 4.1. Lattice structure for the (a) D3Q19 and (b) D3Q7 lattices.

A key aspect in every numerical scheme is the accurate description of the boundary condition, in particular for multi-boundary systems such as packed or fluidized beds. For the energy equation, the method that is easiest to implement in thermal LBM is the bounce back scheme. He et al. (1998) extended the bounce back rule for

non-equilibrium distribution proposed by Zou & He (199) to thermal boundary condition. Ginzburg (2005) proposed a multi-reflection approaches for Dirichlet boundary condition which is a general form of interpolation based bounce back scheme. Li et al. (20) developed a bounce-back-based interpolation method for Dirichlet boundary condition for multiple relaxation time-thermal lattice Boltzmann method. By tuning the interpolation parameters, the method can achieve second order accuracy. In addition to bounce back scheme, Guo et al. (2002) proposed a non-equilibrium extrapolation method for double population model by decomposing the distribution into equilibrium and non-equilibrium parts at the boundary nodes. In this method, the equilibrium part of the temperature distribution at the boundary node is calculated using known wall temperature, whereas the non-equilibrium part is extrapolated from neighboring fluid nodes. To improve the accuracy of interpolation based boundary conditions, cut cell or sub-grid information is introduced. However, the computational cost and selection of interpolation scheme have to be taken into account when addressing complex boundaries.

In this Chapter, the hydrodynamic boundary condition proposed by Noble and Torczynski (1998) for isothermal flows is extended to the thermal lattice Boltzmann method. The original method for the hydrodynamic boundary condition can easily handle boundary dominated problems (e.g. porous media) in which the solid-fluid interface does not confirm to the grid. In addition, this method takes into account the sub-grid effects and viscosity so that the solid fluid interface shifts smoothly.

4.3   Boundary conditions

In this section, the treatments for hydrodynamic and thermal boundary conditions are presented. The hydrodynamic boundary condition proposed by Noble and Torczynski (1998) is implemented for the isothermal lattice Boltzmann method. The extension of the method to the thermal lattice Boltzmann method is developed for Dirichlet boundary conditions.

4.3.1   Hydrodynamic boundary condition

An immersed moving boundary condition (Noble and Torczynski, 1998) is incorporated to enforce the no-slip condition at the surface of each particle. The lattice Boltzmann equation is therefore modified to account for the interaction between the solid and fluid phases:

$$f_i(\vec{x} + \vec{e}_i \Delta t, t + \Delta t) = f_i(\vec{x}, t) - \frac{\Delta t}{\tau_v}(1 - B_v)[f_i(\vec{x}, t) - f_i^{eq}(\vec{x}, t)] + B_v \Omega_{i,v}^{p} \qquad (4.8)$$

where B_v is the weighting function that depends on the local solid volume fraction ϕ_x of a lattice covered by the particles and relaxation time τ_v, according to:

$$B_v(\phi_x, \tau_v) = \frac{\phi_x(\frac{\tau_v}{\Delta t} - \frac{1}{2})}{(1 - \phi_x) + (\frac{\tau_v}{\Delta t} - \frac{1}{2})} \qquad (4.9)$$

$\Omega_{i,v}^{p}$ is an additional collision term that bounces back the non-equilibrium part of the distribution:

$$\Omega_{i,v}^{p} = f_{-i}(\vec{x}, t) - f_i(\vec{x}, t) + f_i^{eq}(\rho_f(\vec{x}, t), \vec{u}_p(\vec{x}, t)) - f_{-i}^{eq}(\rho_f(\vec{x}, t), \vec{u}_f(\vec{x}, t)) \qquad (4.10)$$

where $\vec{u}_p(x, t)$ is the particle velocity at position $\vec{x}$ and time t, and -i denotes the distribution component which has the opposite direction to i.

4.3.2   Dirichlet thermal boundary condition

Figure 4.2 plots the unknown distribution at the boundary. The energy distribution function g_i at the boundary node, which streams into the fluid lattice at next time step, is unknown.   To calculate g_i, the bounce back rule for a non-equilibrium energy distribution (Peng et al., 2003) is applied:

$$g_i^{neq} = -g_{-i}^{neq} \qquad (4.11)$$

Thus

$$g_i(\vec{x}_B, t) - g_i^{eq}(\phi_s, \vec{u}_f) = -(g_{-i}(\vec{x}_B, t) - g_{-i}^{eq}(\vec{x}_B, t)) \qquad (4.12)$$
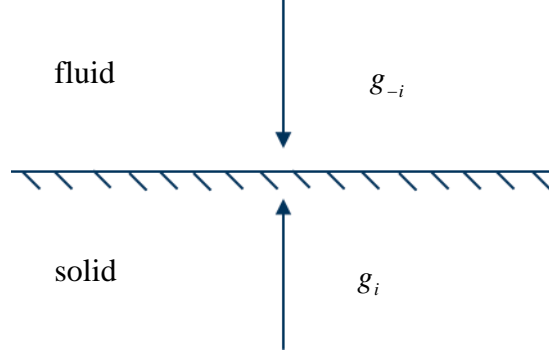
Figure 4.2. Schematic plot of the unknown distribution at the boundary.

Analogous to the hydrodynamic boundary condition, the evolution equation for the energy distribution function is therefore modified

$$g_i(\vec{x}+\vec{e}_i\Delta t, t+\Delta t) = g_i(\vec{x},t) - \frac{\Delta t}{\tau_c}(1-B_c)[g_i(\vec{x},t) - g_i^{eq}(\vec{x},t)] + B_c\Omega_{i,c}^p \qquad (4.13)$$

where $\Omega_{i,c}^p$ is an additional collision term, and B_c is the weighting function which has a similar form   to B_v.

$$\Omega_{i,c}^p = -g_{-i}(\vec{x},t) - g_i(\vec{x},t) + g_i^{eq}(\phi_s, \vec{u}_f) + g_{-i}^{eq}(\phi, \vec{u}_f) \qquad (4.14)$$

$$B_c(\phi_x, \tau_c) = \frac{\phi_x(\frac{\tau_c}{\Delta t} - \frac{1}{2})}{(1-\phi_x) + (\frac{\tau_c}{\Delta t} - \frac{1}{2})} \qquad (4.15)$$

where ϕ_s is the particle energy at the position $\vec{x}$ and time t. $B_c=0$ and $B_c=1$ correspond to pure fluid nodes and solid nodes, respectively.

Figure 4.3 shows the calculation of the local solids volume fraction for each lattice for a spherical particle. If the lattice is partially covered by the particle, the lattice is then subdivided into uniform cubes, e.g. $N_{sub} \times N_{sub} \times N_{sub}$. If the center of the cube is inside of the particle, then the volume of the cube is taken into account. Looping all the cubes, we obtain the solids volume fraction ϕ_x for the lattice. In current work the N_{sub} is 10.
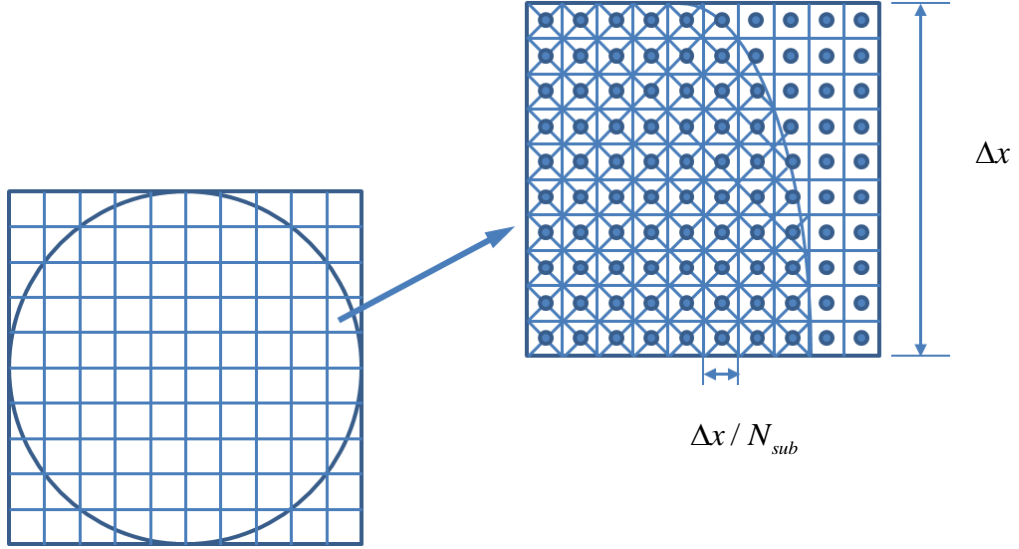
Figure 4.3. Schematic description of calculating local solids volume fraction covered by a spherical particle

4.4 Asymptotic analysis of the thermal boundary condition

In this section, asymptotic analysis of a thermal boundary condition proposed by Yoshida et al. (2010) is applied. Prior to asymptotic analysis, the following dimensionless variables are introduced:

$$t' = \frac{U}{L}t, \quad \vec{x}' = \frac{1}{L}\vec{x}, \quad \varepsilon = \frac{\Delta x}{L} \tag{4.16}$$

where L is the reference length, U is the reference speed and ε is a small parameter used for expansion. U is defined as follows:

$$U = \frac{\Delta x}{\Delta t}\varepsilon \tag{4.17}$$

Thus

$$t' = \frac{\varepsilon^2}{\Delta t}t \tag{4.18}$$

After introducing the dimensionless variables, the energy evolution equation becomes

$$g_i(t' + \varepsilon^2, \vec{x}' + \vec{e}_i \varepsilon) - g_i(t', \vec{x}') = -\frac{1}{\tau_c}[g_i(t', \vec{x}') - g_i^{eq}(t', \vec{x}')] \qquad (4.19)$$

$$g_i^{eq}(t', x') = w_{i,c}\phi(1 + \varepsilon \cdot 4 \cdot \frac{\vec{e}_i \cdot \vec{u}_f'}{c^2}) \qquad (4.20)$$

Where $\vec{u}_f' = \frac{\vec{u}_f}{U}$. The energy distribution function and macroscopic ϕ are expanded in terms of powers of ε, respectively.

$$g_i = g_i^{(0)} + g_i^{(1)}\varepsilon + g_i^{(2)}\varepsilon^2 + \cdots \qquad (4.21)$$

$$\phi = \phi^{(0)} + \phi^{(1)}\varepsilon + \phi^{(2)}\varepsilon^2 + \cdots \qquad (4.22)$$

According to equation (4.6), we get

$$\phi^{(m)} = \sum_i g_i^{(m)} \qquad (4.23)$$

Where m is the order of the expansion. Expanding the left hand side (LHS) of equation (4.19) using Taylor expansion (here the Einstein convention is used):

$$LHS = e_{i\alpha}\frac{\partial g_i^{(m)}}{\partial x_\alpha'}\varepsilon + \left(\frac{\partial g_i^{(m)}}{\partial t'} + \frac{1}{2}\frac{\partial^2\left(e_{i\alpha}e_{i\beta}g_i^{(m)}\right)}{\partial x_\alpha'\partial x_\beta'}\right)\varepsilon^2 + O\left(\varepsilon^2\right) \qquad (4.24)$$

Where α, β, γ are the coordinates in 3D space. After inserting equations (4.21) and (4.22) into the right hand side of equation (4.19), we find

$$RHS = -\frac{1}{\tau_c}\left[g_i^{(0)} + g_i^{(1)}\varepsilon + g_i^{(2)}\varepsilon^2 - w_{i,c}\left(\phi^{(0)} + \phi^{(1)}\varepsilon + \phi^{(2)}\varepsilon^2\right) - 4 \cdot \frac{w_{i,c}\vec{e}_i\vec{u}_f'}{c^2}\left(\phi^{(0)} + \phi^{(1)}\varepsilon\right)\varepsilon + O\left(\varepsilon^2\right)\right] \qquad (4.25)$$

Equating the coefficients of the same power of ε for equation (4.19), we find the following equations:

$$\text{Zeroth-order } \varepsilon^0: \quad g_i^{(0)} - w_{i,c}\phi^{(0)} = 0 \qquad (4.26)$$

$$\text{First-order } \varepsilon^1: \quad e_{i\alpha}\frac{\partial g_i^{(0)}}{\partial x_\alpha'} = -\frac{1}{\tau_c}\left[g_i^{(1)} - w_{i,c}\phi^{(1)} - 4 \cdot \frac{w_{i,c}\phi^{(0)}\vec{e}_i\vec{u}_f'}{c^2}\right] \qquad (4.27)$$

Taking the Taylor expansion of equation (4.13) at the boundary node $\vec{x}_B$ and assuming that the boundary locates between nodes $\vec{x}'$ and $\vec{x}' + \vec{e}_i \varepsilon$, we find:

$$\vec{x}' + \vec{e}_i \varepsilon = \vec{x}_B' + \vec{e}_i (1 - B_c) \varepsilon , \quad \vec{x}' = \vec{x}_B' - \vec{e}_i B_c \varepsilon \tag{4.28}$$

Thus, we have

$$g_i^{(m)}\left(t' + \varepsilon^2, \vec{x}_B' + \vec{e}_i\left(1 - B_c\right)\varepsilon\right) = g_i^{(m)} +$$

$$\left(e_{i\alpha} \varepsilon \left(1 - B_c\right) \frac{\partial}{\partial x_\alpha'} + \varepsilon^2 \frac{\partial}{\partial t'} + \frac{1}{2}\left(1 - B_c\right)^2 \varepsilon^2 e_{i\alpha} e_{i\beta} \frac{\partial^2}{\partial x_\alpha' x_\beta'} + O\left(\varepsilon^2\right) \right) g_i^{(m)} \tag{4.29}$$

$$g_i^{(m)}\left(t' + \varepsilon^2, \vec{x}_B' - \vec{e}_i B_c \varepsilon\right) = g_i^{(m)} + \left(-e_{i\alpha} \varepsilon B_c \frac{\partial}{\partial x_\alpha'} + \varepsilon^2 \frac{\partial}{\partial t'} + \frac{1}{2} B_c^2 \varepsilon^2 e_{i\alpha} e_{i\beta} \frac{\partial^2}{\partial x_\alpha' x_\beta'} + O\left(\varepsilon^2\right) \right) g_i^{(m)} \tag{4.30}$$

$$\phi^{(m)}\left(t' + \varepsilon^2, \vec{x}_B' - \vec{e}_i B_c \varepsilon\right) = \phi^{(m)} + \left(-e_{i\alpha} \varepsilon B_c \frac{\partial}{\partial x_\alpha'} + \varepsilon^2 \frac{\partial}{\partial t'} + \frac{1}{2} B_c^2 \varepsilon^2 e_{i\alpha} e_{i\beta} \frac{\partial^2}{\partial x_\alpha' x_\beta'} + O\left(\varepsilon^2\right) \right) \phi^{(m)} \tag{4.31}$$

$$g_i^{eq}\left(\phi_s, \vec{u}_f'\right) = w_{i,c} \phi_s \left(1 + \varepsilon \cdot 4 \cdot \frac{\vec{e}_i \vec{u}_f'}{c^2} \right) \tag{4.32}$$

$$g_i^{eq}\left(\phi, \vec{u}_f'\right) = w_{i,c} \phi^{(m)}\left(t' + \varepsilon^2, \vec{x}_B' - \vec{e}_i B_c \varepsilon\right)\left(1 + \varepsilon \cdot 4 \cdot \frac{\vec{e}_i \vec{u}_f'}{c^2} \right) \tag{4.33}$$

Equation (4.13) expressed in zeroth order with respect to ε is:

$$g_i^{(0)} = g_i^{(0)} - \frac{1}{\tau_c}\left(1 - B_c\right)\left[g_i^{(0)} - w_{i,c} \phi^{(0)} \right] + B_c \left(-g_i^{(0)} - g_{-i}^{(0)} + w_{i,c} \phi_s + w_{i,c} \phi^{(0)} \right) \tag{4.34}$$

Using equation (4.26), equation (4.34) becomes

$$g_i^{(0)} = w_{i,c} \phi_s \tag{4.35}$$

Taking the zeroth moment of equation (4.35):

66

$$\phi^{(0)} = \phi_s \tag{4.36}$$

Therefore, the zeroth order solution $\phi^{(0)}$ satisfies the Dirichlet boundary condition. The first order of equation (4.13) in ε is

$$\left(1 - B_c\right) e_{i\alpha} \frac{\partial g_i^{(0)}}{\partial x_\alpha^{'}} = -B_c e_{i\alpha} \frac{\partial g_i^{(0)}}{\partial x_\alpha^{'}} - \frac{1}{\tau_c}\left(1 - B_c\right)\left[g_i^{(1)} - B_c e_{i\alpha} \frac{\partial g_i^{(0)}}{\partial x_\alpha^{'}} + w_{i,c} B_c e_{i\alpha} \frac{\partial \phi^{(0)}}{\partial x_\alpha^{'}} - w_{i,c}\phi^{(1)} - 4 \cdot w_{i,c}\phi^{(0)} \frac{\vec{e}_i \vec{u}_f^{'}}{c^2} \right]$$
$$+ B_c\left(-\left(g_{-i}^{(1)} + B_c e_{i\alpha} \frac{\partial g_{-i}^{(0)}}{\partial x_\alpha^{'}} + g_i^{(1)} - B_c e_{i\alpha} \frac{\partial g_i^{(0)}}{\partial x_\alpha^{'}} \right) + 4 \cdot w_{i,c}\phi_s \frac{\vec{e}_i \vec{u}_f^{'}}{c^2} + w_{i,c}\phi^{(1)} - 4 \cdot w_{i,c}\phi^{(0)} \frac{\vec{e}_i \vec{u}_f^{'}}{c^2} + w_{i,c} B_c e_{i\alpha} \frac{\partial \phi^{(0)}}{\partial x_\alpha^{'}} \right) \tag{4.37}$$

Substituting equations (4.26) and (4.27) into equation (4.37), we find

$$0 = -e_{i\alpha} \frac{\partial g_i^{(0)}}{\partial x_\alpha^{'}} +$$
$$\left(-\left(g_{-i}^{(1)} + B_c e_{i\alpha} \frac{\partial g_{-i}^{(0)}}{\partial x_\alpha^{'}} + g_i^{(1)} - B_c e_{i\alpha} \frac{\partial g_i^{(0)}}{\partial x_\alpha^{'}} \right) + 4 \cdot w_{i,c}\phi_s \frac{\vec{e}_i \vec{u}_f^{'}}{c^2} + w_{i,c}\phi^{(1)} - 4 \cdot w_{i,c}\phi^{(0)} \frac{\vec{e}_i \vec{u}_f^{'}}{c^2} + w_{i,c} B_c e_{i\alpha} \frac{\partial \phi^{(0)}}{\partial x_\alpha^{'}} \right) \tag{4.38}$$

Since

$$\sum_i e_{i\alpha} \frac{\partial g_i^{(0)}}{\partial x_\alpha^{'}} = 0$$

$$\sum_i g_{-i}^{(1)} = \sum_i g_i^{(1)} = \phi^{(1)}$$

$$\sum_i 4 \cdot w_{i,c}\phi_s \frac{\vec{e}_i \vec{u}_f^{'}}{c^2} = \sum_i 4 \cdot w_{i,c}\phi \frac{\vec{e}_i \vec{u}_f^{'}}{c^2} = 0$$

$$\sum_i w_{i,c}\phi^{(1)} = \phi^{(1)}$$

$$\sum_i w_{i,c} B_c e_{i\alpha} \frac{\partial \phi^{(0)}}{\partial x_\alpha^{'}} = 0 \tag{4.39}$$

Thus, summing the equation (4.38) over i, we find

$$\phi^{(1)} = 0 \tag{4.40}$$

Recalling equations (4.22) and (4.36), the following expression is therefore obtained:

$$\phi = \phi_s + O(\varepsilon^2) \qquad (4.41)$$

Equation (4.41) indicates that the proposed boundary condition is satisfied with up to second order accuracy with $\phi^{(0)}$ solving the thermal lattice Boltzmann equation.

4.5 Numerical validation of the thermal boundary condition

In this section, the new boundary condition is applied to solve several problems with curved boundaries. The goal is to validate the method by comparison with theoretical solutions and previous direct numerical simulations. The accuracy of the boundary condition and convergence with grid refinement are confirmed numerically. Moreover, the second and third tests indicate that the method is robust to predict heat transfer due to convection between fluid and particles with both static and moving curved boundaries.

4.5.1 Heat diffusion of a hot sphere in unbounded stationary fluid

A sphere with constant temperature ($T_s = 1$) is immersed in an unbounded stationary fluid at $t=1$. The temperature T_∞ of the fluid that is far away from the sphere is 0. The analytical solution of the fluid temperature $T(r, t)$ in radial direction is as follows:

$$\frac{T(r,t) - T_\infty}{T_s - T_\infty} = \frac{R}{r}(1 - erf(\frac{r - R}{\sqrt{4tD}})) \qquad (4.42)$$

Where R is the radius of the sphere, r is the radial distance from the sphere centre, $r > R$. The Nusselt number, which is defined as $N_u = h_f(2R)/k_f$, where h_f is the heat transfer coefficient and k_f is the thermal conductivity of the fluid, is theoretically calculated as a function of time t:

$$Nu(t) = 2 + \frac{2}{\sqrt{\pi}}\frac{R}{\sqrt{Dt}} \qquad (4.43)$$

In the simulations, the particle diameter is 1mm, and the thermal diffusivity is $D = 10^{-6}\ m^2/s$. The time step is 10^{-4} s. Four different resolutions of sphere are used,

d_p=15, 20, 25 and 30. The domain size is set to $8d_p$. The setup and fluid properties are therefore the same as Tavassoli et al. (2013), who used an immersed boundary method with a finite different method to solve the momentum and energy equations. The normal derivative of temperature at all domain boundaries is set to zero.

Figure 4 shows the non-dimensional temperature distribution around the sphere at time $t = 0.6$ s for $d_p = 20$. Table 4.1 reports the Nusselt number calculated by the LBM, Tavassoli et al. (2013) and equation (4.43) at different times. It shows that the grid resolution of $d_p = 15$ is sufficient. The comparison indicates that the current model is more accurate than the model reported by Tavassoli et al. (2013). Figure 4.5 plots the instantaneous non-dimensional temperature profile obtained by LBM and the analytical solution for $d_p = 20$. It demonstrates that the model successfully predicts the temperature evolution of the fluid. Figure 4.6 shows the relative deviation for Nusselt number between LBM results and equation (4.43) as a function of particle resolution at t=0.1 s. The log-log plot indicates that the proposed boundary condition has quadratic convergence with grid refinement. Moreover, the LBM simulations converge quickly with regards to grid resolution since the accuracy does not apparently increase with increasing resolution if $d_p \geq 15$. Therefore, the new boundary condition can achieve a high accuracy at relatively low grid resolution. To probe the accuracy of the boundary condition numerically, the maximum error between LBM simulations and analytical solution is calculated for different resolutions at t=0.1 s. E_∞ is defined as follows:

$$E_\infty = \underset{x,y,z}{Max} \left| Nu_{LBM} - Nu \right| \tag{4.44}$$

Figure 4.7 plots E_∞ as a function of grid resolution. The plot confirms that the new thermal boundary condition is second order accurate.
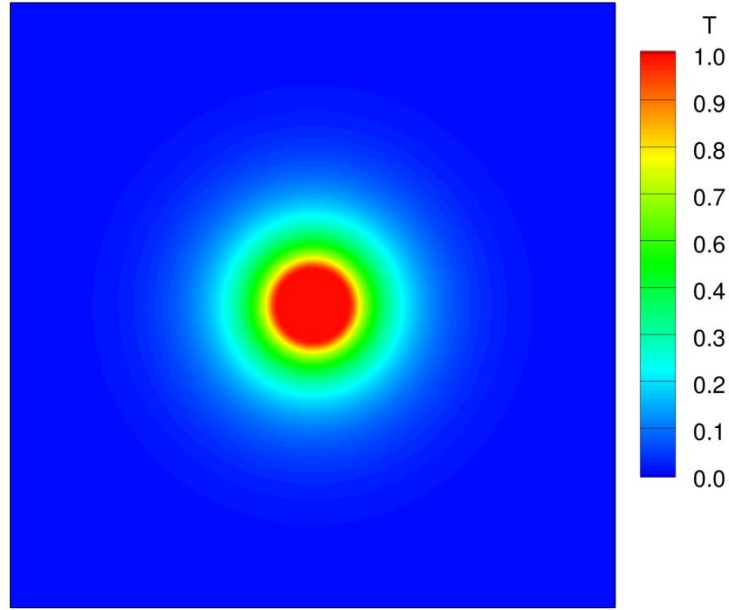
Figure 4.4. Non-dimensional temperature distribution around the sphere at time t=0.6 s for $d_p = 20$. The relaxation time is 0.66.

Time (s)	LBM				Tavassoli et al. (2013)				Eq. (4.39)
	$d_p = 15$	$d_p = 20$	$d_p = 25$	$d_p = 30$	$d_p = 15$	$d_p = 20$	$d_p = 25$	$d_p = 30$	
0.4	2.90	2.89	2.89	2.89	3.01	2.97	2.95	2.93	2.89
0.6	2.73	2.73	2.73	2.72	2.83	2.80	2.78	2.77	2.73
0.8	2.63	2.63	2.63	2.63	2.73	2.70	2.68	2.67	2.63
1.0	2.57	2.56	2.57	2.56	2.66	2.63	2.61	2.60	2.56

Table 4.1. Comparison of Nusselt number obtained from LBM, Tavassoli et al. (2013) and the analytical solution

Figure 4.5.Comparison of radial temperature distribution between LMB and the analytical solution. The relaxation time is 0.66.
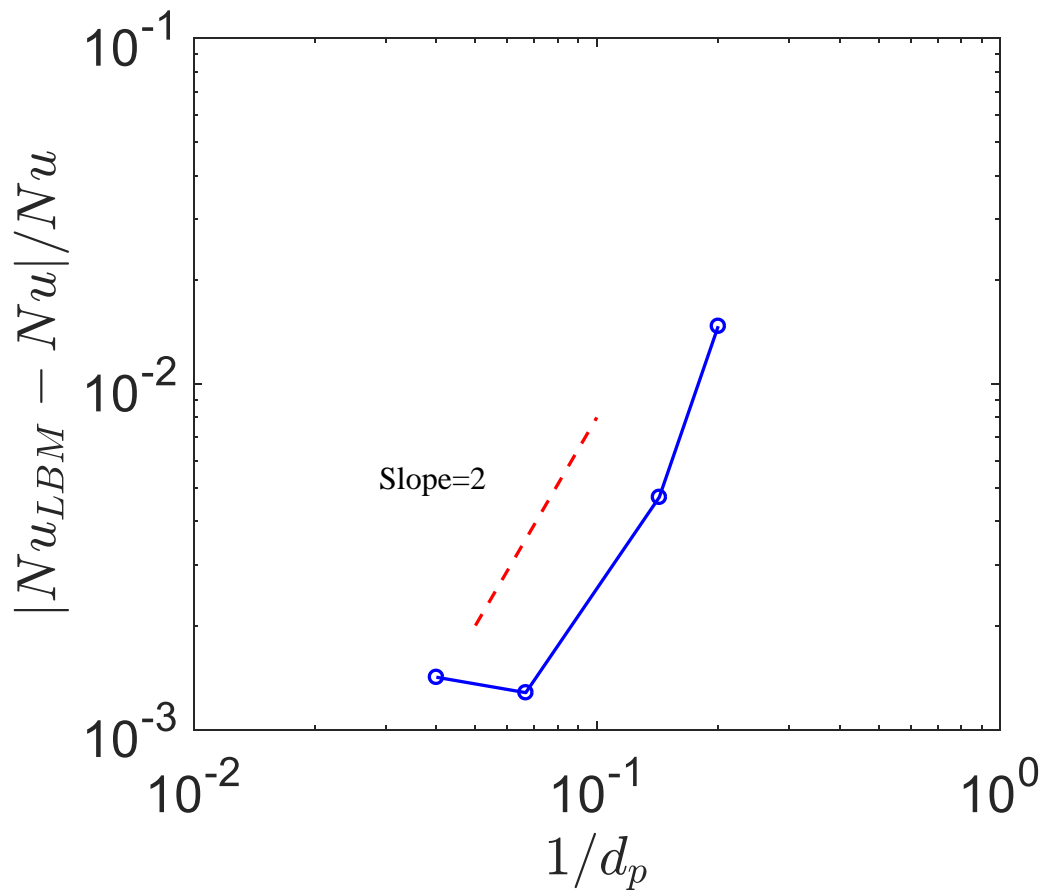
Figure 4.6. Relative deviation between LBM data and the analytical solution as a function of resolution for $\tau_c = 0.5899$.
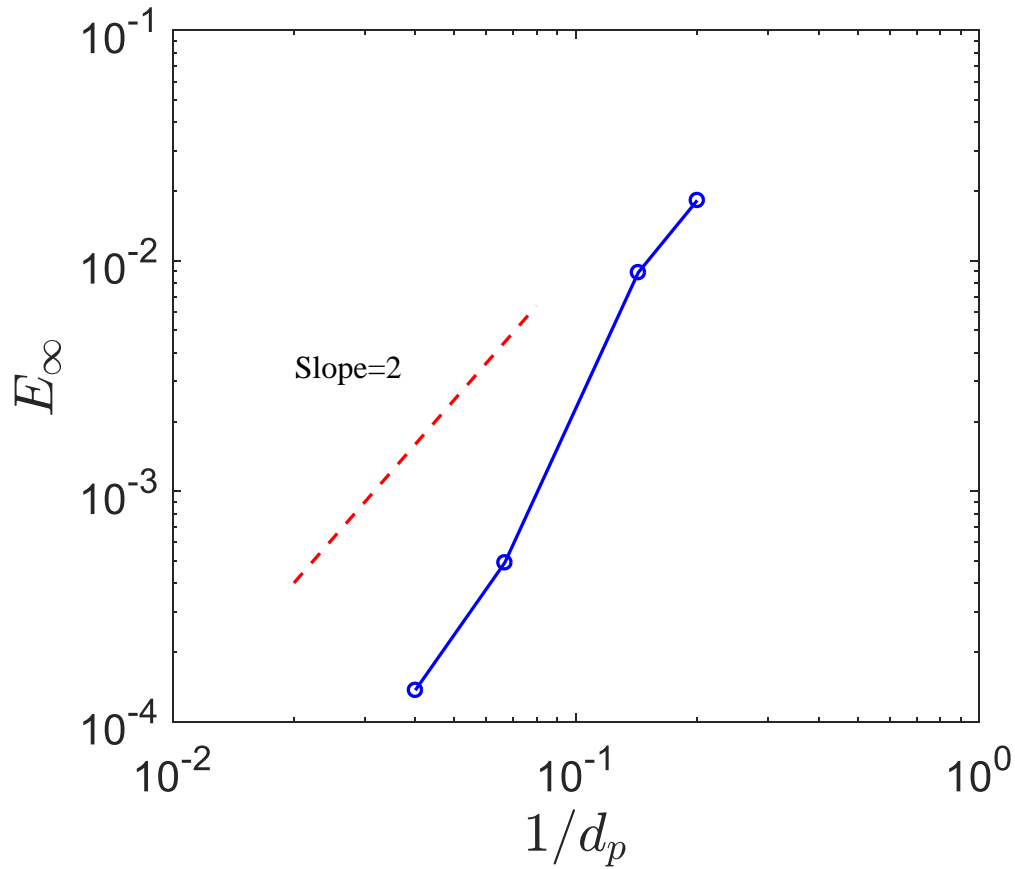
Figure 4.7. The maximum error E_∞ as a function of grid resolution at t=0.1 s. The relaxation time is 05899.
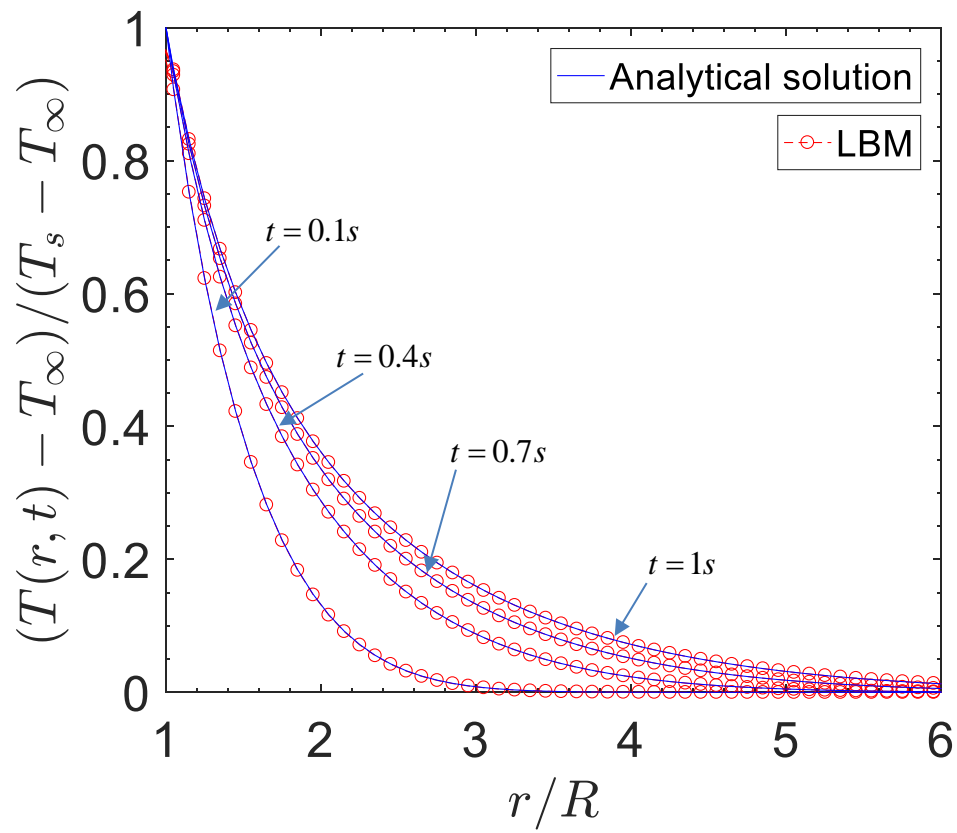
4.5.2 Thermal evolution of a sphere in uniform flow

A cold sphere is suddenly immersed in a hot fluid at time t=0. Due to the heat transfer from the surrounding fluid to the sphere, the temperature of the sphere increases with time and approaches the far field fluid temperature. If the diffusion time scale inside the sphere is much smaller than the convective time scale of the flow outside, the temperature distribution inside the sphere can be considered homogeneous which means that there is no temperature gradient inside the sphere. The temperature of the sphere can be calculated as follows:

$$\frac{dT_s}{dt} = -\frac{\gamma D}{V_p} \oint_{\partial s} \nabla T \cdot \vec{n} ds \qquad (4.45)$$

where Pr is the Prandtl number, defined as $Pr = \nu/D$ ($Pr = 0.7$ in the simulations), $\vec{n}$ denotes the norm direction pointing into the fluid at the surface of the sphere and $\gamma = \left(\rho C_p\right)_f / \left(\rho C_p\right)_s$, where C_p is the heat capacity. V_p is particle volume. To validate our boundary condition, the temperature evolution of the sphere in a uniform flow is calculated and compared with the results of Balachandar et al. (2001) who used a spectral method in spherical coordinates to solve the problem. The number of lattices is $300 \times 150 \times 150$. The particle diameter is 25 in lattice units. The Reynolds number is 50. The time step is 0.00004 s. The lattice size is 0.00008 m. A uniform flow is specified at the inlet. A stress free boundary is taken at the outlet. The symmetry boundary condition is imposed at the side walls. At the particle surface, the no-slip condition is enforced. The fluid temperature at the inlet is set to 1, and the particle temperature is initialized as zero. Adiabatic boundary conditions are applied at all other boundaries. In the simulation, γ is set to 0.1, 0.02, 0.004. The time is normalized by d_p/u_s, where $\vec{u}_s$ is the fluid velocity at the inlet. Figure 4.8 compares the LBM results with that calculated by Balachandar et al. (2001). In general, the agreement is good. It should be pointed out that Balachandar et al. (2001) used a very fine grid to resolve the boundary layer of the sphere. Moreover, the grid in radial direction was non-uniform in the prior work. However, a uniform grid is used in our simulations. Because of the computational time, we could not use as large of a domain size as Balachandar et al. (2001) did.
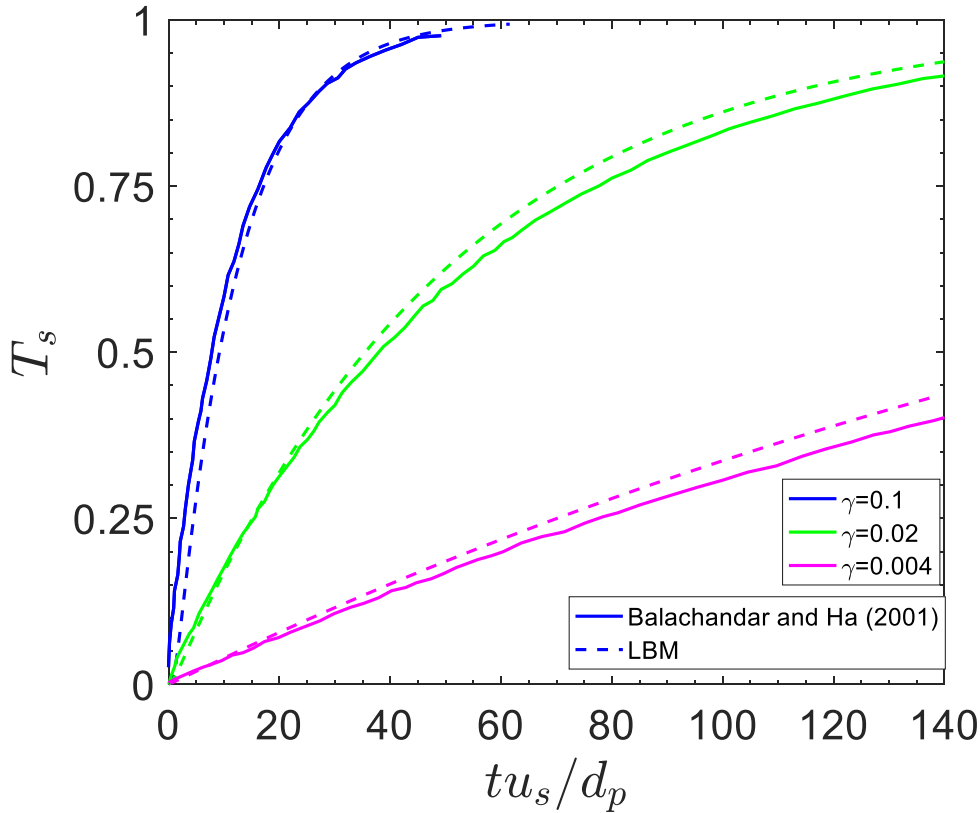
Figure 4.8. Evolution of particle temperature in a uniform flow. The lines with circles are the simulation results calculated by Balachandar et al. (2001).

4.5.3 Settling of a sphere in a semi-infinite channel

Before validating the method against the results of Dan et al. (2010) for a non-isothermal case, we first validate the boundary condition for hydrodynamics using an isothermal case. The hydrodynamic boundary condition has been applied to calculate the drag force for assemblies of spheres and approximately cubic particles (Chen et al., 2015). To validate the capacity of addressing moving boundaries, a sphere settling in a box is simulated. Ten Cate et al. (2002) measured the spherical particle sedimentation velocity in a box for several Reynolds numbers. The box size is 160 mm×100 mm×100 mm and the diameter of the particle is 0.015 m. The density of the particle is 1120 kg/m^3. In the simulations, the grid size is 0.001 m, and the time step is 0.00005s. Figure 4.9 reports the settling velocity of the particle together with the experimental data (Ten Cate et al., 2002) and simulation results of Dan et al. (2010). The comparison between LBM simulations and the results of Dan et al. (2010) is rather good. In general, the LBM simulation results have a good agreement with the

experimental results. The discrepancy in the deceleration regime may be due to the coarse grid resolution since the grid size is 1 mm. In addition, we do not employ any lubrication model when the particle approaches the bottom wall.

If a hot sphere sediments in a cold fluid, the sphere can be considered as a heat source. Due to the heat transfer between sphere and surrounding fluid, the temperature of the fluid changes with time. The Boussinesq approximation is used so that the temperature change only modifies the fluid density:

$$\rho_f = \rho_{f0}[1 - \beta_f(T_f - T_{f0})] \tag{4.46}$$

Where ρ_{f0}, T_{f0} are the initial fluid density and temperature, respectively. β_f is the fluid thermal expansion coefficient. T_f is the instantaneous fluid temperature. As a result, a body force which is equal to $\rho_f \vec{g}$ is applied to the fluid. The Grashof number, which is the ratio of buoyancy to viscous force, is defined as follows:

$$Gr = \frac{\beta_f d_p^3 g(T_s - T_{f0})}{\nu^2} \tag{4.47}$$

The reference velocity, which is defined as the theoretical sedimentation velocity (U_{ref}) of a single particle in unbounded flow, is used to estimate the Reynolds number.

$$U_{ref} = \sqrt{\frac{4d_p(\rho_s/\rho_f - 1)}{3}g} \tag{4.48}$$

The last validation test is a sphere settling in a semi-infinite channel with different Grashof numbers which was studied by Dan et al. (2010) using the finite element method (FEM). The Reynolds number (Re = $U_{ref}d_p/\nu$) is 35, 50 and 100. The Pr and γ are set to 1. ρ_s/ρ_f is in the range of 1.002 to 1.1. The domain size is $20d_p \times 20d_p \times 20d_p$. The lattice size and time step are 0.00008 m and 0.00008 s, respectively. The particle diameter is 0.0016 m. Once the particle moves one lattice, we remove one layer of fluid at the top and add one layer of fluid to the bottom (Dan et al., 2010). This ensures the infinite long channel in the particle settling direction. Zero velocity and stress free boundary conditions are assigned at the bottom and top boundaries. No-slip boundary condition is specified at the side walls and the particle surface. Figure 4.10 shows the vertical velocity and temperature contour for Re=50 and Gr=100 at the central plane. Figure 4.11 plots the terminal settling velocity

normalized by U_{ref} as a function of Reynolds number. It shows that the positive Gr decreases the terminal settling velocity of the particle since the body force induces upward flow which increases the relative velocity between the particle and surrounding fluid. However, with increasing Reynolds number, the Grashof number ($Gr=\pm100$) has a negligible effect on the terminal settling velocity. Figure 4.11 shows a good agreement between current simulations and the results of Dan et al. (2010). Therefore the present method can accurately handle thermal and curved moving boundaries.
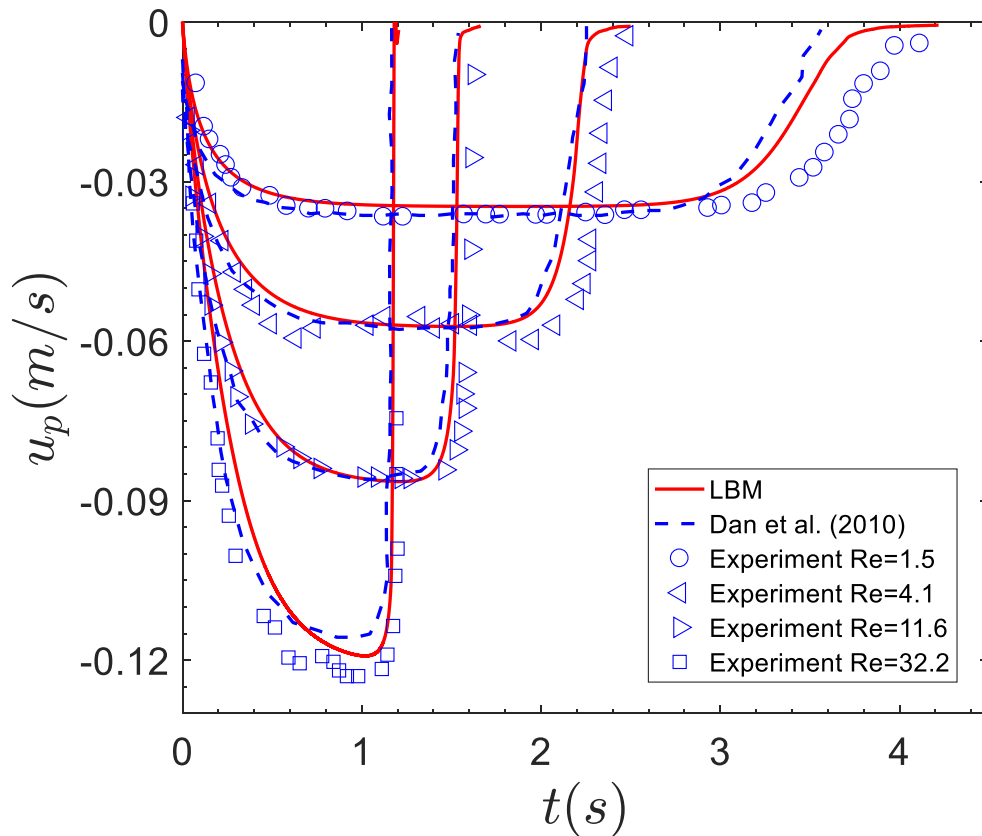
Figure 4.9. Particle settling velocity as a function of time in a box. The symbols are the experimental data extracted from Ten Cate et al. (2002). The blue dashed lines plot the simulation results of Dan et al. (2010).
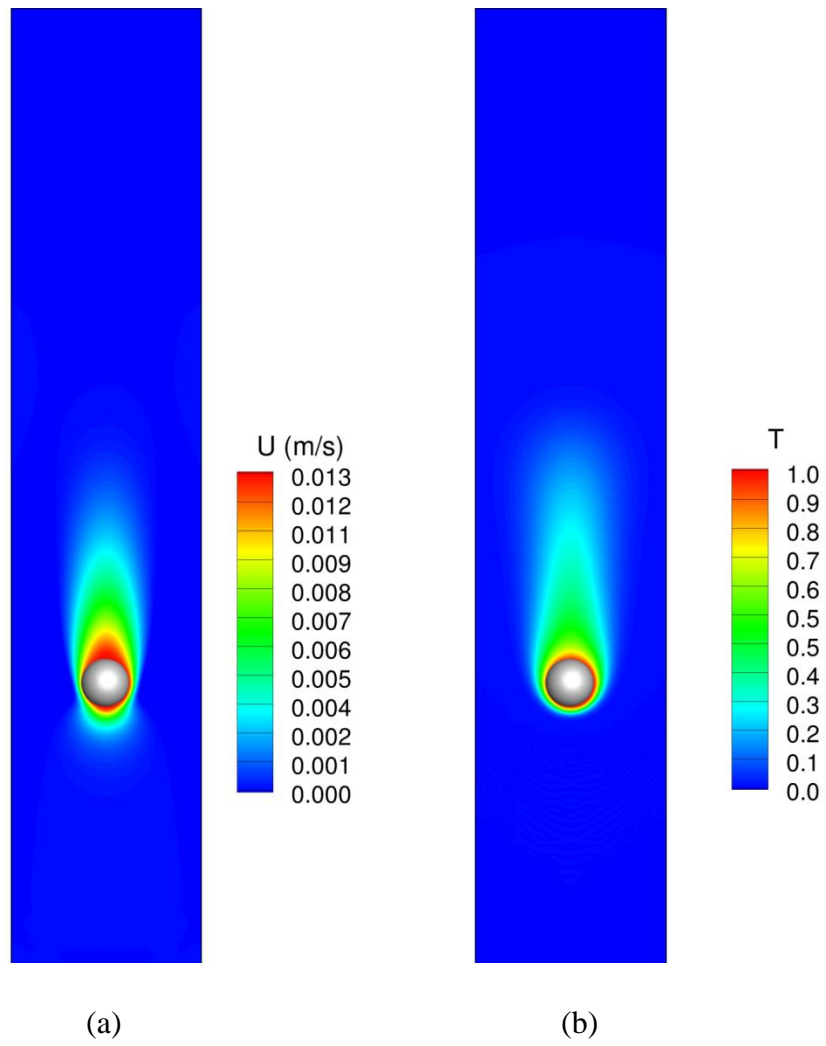
Figure 4.10. (a) Vertical velocity contour for Gr=100, Re=50 at the central plane. (b) Corresponding temperature contour.
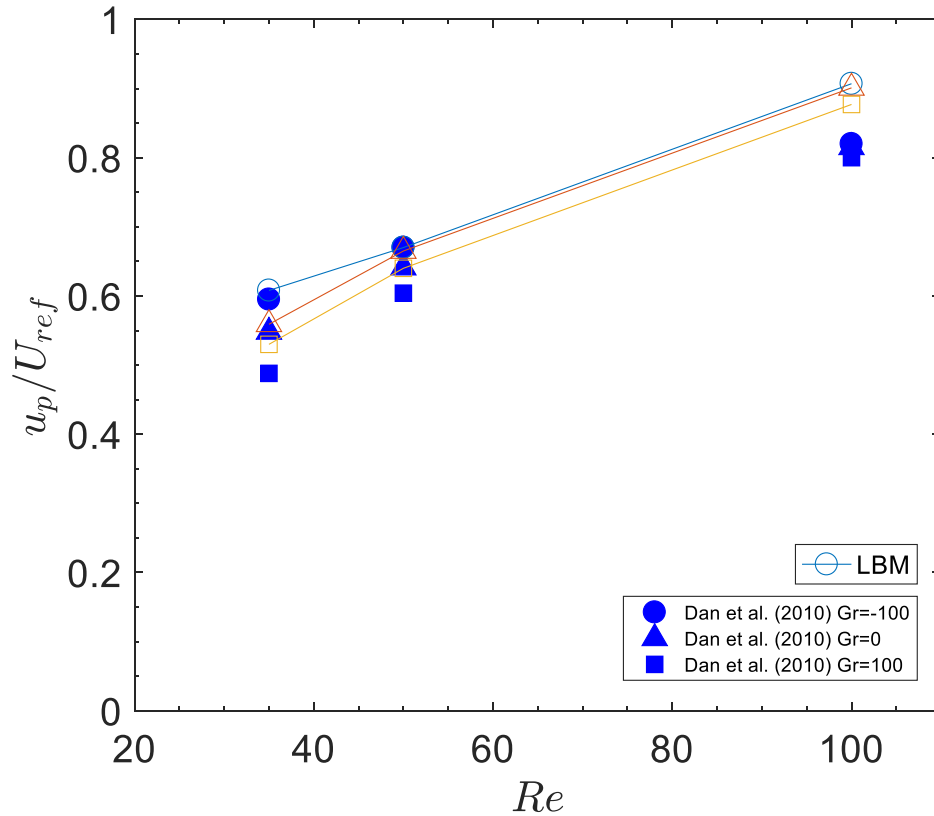
Figure 4.11. Sedimentation of sphere in a semi-infinite long channel for different Grashof numbers.

4.6   Conclusions

A new Dirichlet boundary condition for the thermal lattice Boltzmann method has been developed and applied to simulate heat diffusion and convection for spheres immersed in a fluid. Asymptotic analysis of the method shows that the boundary condition has second order accuracy with respect to the lattice spacing. Comparison with the analytical solution for pure heat diffusion numerically confirms that the new boundary condition is second order accurate and has approximately quadratic convergence with grid refinement. In addition, the predictions for fluid temperature and Nusselt number match the analytical solution. Further validations indicate that the new boundary condition can accurately capture the heat convection for curved boundaries between particles and fluids. Based on these validation cases, the new thermal boundary condition is robust to simulate static and moving curved boundaries.

In the future, the thermal lattice Boltzmann method will be applied to investigate the heat transfer in packed or fluidized beds. The effect of Prandtl number, Reynolds number and solid volume fraction on the heat transfer coefficient in packed or fluidized beds can be studied in detail. Additionally, the thermal boundary condition will be extended to problems with Neumann boundary condition.

5

Lattice Boltzmann simulation of gas-solid heat transfer in random assemblies of spheres: The effect of solids volume fraction on the average Nusselt number for $\text{Re} \leq 100$

5.1 Abstract

A thermal lattice Boltzmann method has been applied to simulate gas-solid heat transfer in a random assembly of spheres using an immersed moving boundary approach. The numerical data was correlated to propose an expression for the Nusselt number as a function of the Reynolds number and solid volume fraction over a wide range of solids volume fractions ($\phi = [0,0.5]$) for Reynolds numbers up to 100. It is hoped that the new Nusselt number correlation for gas-solid systems improves the accuracy of Euler-Euler and Euler-Lagrangian simulations of gas-solid heat transfer in packed and fluidized beds.

5.2 Introduction

Gas-solid, non-isothermal flows are encountered widely in industry, e.g. gas-fluidized bed reactors. In this context, an improved understanding of the complex interplay between fluid flow and thermal effects, e.g. the formation of hot spots, is essential to improve the reactor design and optimize process conditions. In the past few decades, computational fluid dynamics (CFD) has been used extensively to model fluid flow, heat transfer and chemical reactions in gas-solid systems (Deen et al., 2014). However, the accuracy of numerical predictions of thermal, gas-solid systems relies critically on the availability of accurate closure relationships, such as drag force or heat transfer. For example, Li et al. (2003) reported that the bed expansion in gas-fluidized beds was very sensitive to the dependence of the drag force on the void fraction in the different correlations implemented. Feng et al. (2008) simulated the non-isothermal sedimentation of particles and demonstrated that the drag force acting on the particles was strongly affected by the Reynolds and Grashof numbers (ratio of the buoyancy to the viscous force acting on the fluid). The buoyancy current(s) induced by a pair of hot particles could reverse or prevent the well-known drafting-kissing-tumbling (DKT) motion which is commonly encountered in isothermal sedimentation flows. Indeed, the development of drag force correlations based on the direct numerical simulation

(DNS) of small (idealized) gas-solid systems has attracted substantial attention during the last two decades and has progressed appreciably. Hill et al. (2001a, b) were the first to develop a drag force correlation using direct numerical simulations. Beetstra et al. (2007) extended the work of Hill et al. (2001b) and proposed additional drag force correlations for mono- and bi- dispersed particles for Reynolds numbers up to 1000. Conceptually, improvements in the accuracy of drag force correlations can be divided into two groups: (1) Development of accurate solid boundary descriptions (Tenneti et al., 2011; Tang et al., 2014) that reduce the numerical error due to the discrete representation of a particle's surface and (2) introduction of granular temperature to the drag force correlation (Tang et al., 2016).

Although DNS has been used widely to investigate heat transfer for particulate flows (Shao et al., 2012; Deen et al., 2013; Tenneti et al; 2013; Derksen, 2014; Feng et al., 2014), very few efforts have been reported for the development of heat transfer correlations for randomly packed assemblies using particle-level, direct numerical simulations. Yang et al. (2010), using the commercial code CFX10, proposed correlations for the Nusselt number of ordered packings (i.e. simple cubic, body center cubic and face center cubic packings with spheres and ellipsoids) for turbulent flows. The comparison of their Nusselt number predictions with an empirical correlation (Wakao et al., 1979) showed that the empirical correlation over-predicts the Nusselt number in ordered packings. Deen et al. (2012) using an immersed boundary method simulated randomly packed beds comprising 1326 spheres to determine the heat transfer coefficient. The solids volume fraction and Prandtl number were 0.3 and 0.8, respectively. The results of Deen et al. indicate that the commonly used Gunn equation (1978) over-predicts the heat transfer coefficients for $Re < 100$. Following Deen's work, Tavassoli et al. (2015) proposed a Nusselt number correlation for packed beds of 54 spheres for Reynolds numbers 0-100 and solid volume fraction 0.1-0.6. Sun et al. (2015) using particle-resolved direct numerical simulations developed a Nusselt number correlation for Reynolds numbers in the range 1-100 and solid volume fraction covering the range 0-0.5. The difference between the Nusselt numbers predicted by the correlations of Tavassoli et al. (2015) and Sun et al. (2015) is, however, considerable. Sun et al. (2015) argued that the discrepancy was due to different set ups of the numerical simulations. The numerical set up of Sun et al. (2015) will be discussed in detail in the following section.

Currently, empirical heat transfer correlations, in which the Nusselt number is expressed as a function of the Reynolds number, voidage and Prandtl number are used to model at a macroscopic (i.e. not particle resolved) level gas-solid systems. However, at small Reynolds number, the bed is in a state of thermal equilibrium (or

very close to it) (Shen et al., 1981). As a consequence it is difficult to measure experimentally the Nusselt number under such conditions. Hence, it is not surprising that the experimental data reported by different studies differ by indeed orders of magnitude for $Re \leq 10$ (Gunn, 1978). Also the confidence in empirical correlations (Gunn, 1978; Wakao et al., 1979) for $Re < 100$ is low since those correlations were developed commonly for a wide range of Reynolds number (up to 10^4-10^5). Hence in this work, we propose a Nusselt number correlation for assemblies of spheres for $Re \leq 100$ based on lattice Boltzmann simulations.

The lattice Boltzmann method provides an alternative numerical approach to model fluid flow, heat transfer and chemical reactions. Compared to conventional numerical methods (e.g. finite volume method), the lattice Boltzmann method has several advantages: (1) The convective and collision operators are linear; (2) The fluid pressure can be calculated simply by an equation of state; (3) It is easy to handle complex boundary conditions and (4) it can be parallelized readily, since all computations are local. Here we use the immersed moving boundary approaches proposed by Noble & Torczynski (1998) and Chen & Müller (Chapter 4) to enforce, respectively, a no-slip and a constant temperature boundary condition at the particle surface. The boundary methods used here are suitable for boundary-dominated problems, such as the flow in porous media, fluidized or packed beds.

5.3 Governing equations

In this work the flow is assumed to be incompressible and viscous heat dissipation is neglected. With these assumptions the Navier-Stokes and energy equations can be written as:

$$\rho_f \left(\frac{\partial \vec{u}_f}{\partial t} + \vec{u}_f \cdot \nabla \vec{u}_f \right) = -\nabla p + \mu_f \nabla^2 \vec{u}_f \tag{5.1}$$

$$\rho_f c_{pf} \left(\frac{\partial T_f}{\partial t} + \vec{u}_f \cdot \nabla T_f \right) = k_f \nabla^2 T_f \tag{5.2}$$

Where ρ_f, μ_f, c_{pf}, k_f, $\vec{u}_f$, P and T_f are the density, dynamic viscosity, specific heat capacity, thermal conductivity, velocity, pressure and temperature of the fluid, respectively. The continuity equation for incompressible flows is:

$$\nabla \cdot \vec{u}_f = 0 \tag{5.3}$$

The flow properties (e.g. fluid density and viscosity) are assumed to be independent of the fluid temperature. The Reynolds number is calculated based on the particle diameter (d_p) and the superficial fluid velocity ($\vec{u}_s$) which is defined as the fluid velocity averaged over the total volume of the bed:

$$\text{Re} = \frac{\rho_f \vec{u}_s d_p}{\mu_f} \tag{5.4}$$

The Prandtl number is given by:

$$\text{Pr} = \frac{c_{pf} \mu_f}{k_f} \tag{5.5}$$

The heat transfer coefficient for a spherical particle can be calculated as:

$$h = \frac{\dot{q}}{\pi d_p^2 \Delta T} \tag{5.6}$$

$$\Delta T = T_{f-ave} - T_s \tag{5.7}$$

where $\dot{q}$, T_{f-ave} and T_s are the heat transfer rate, average temperature of the surrounding fluid and the particle temperature, respectively. In practice, the heat transfer coefficient h is expressed in terms of the Nusselt number:

$$Nu = \frac{h d_p}{k_f} \tag{5.8}$$

According to the definition of T_{f-ave}, two different local Nusselt numbers are proposed. The 'mixing cup' temperature is the average fluid temperature of a plane which is perpendicular to the streamwise direction, viz.

$$< T_f(x) >= \frac{\iint_S u_f(x, y, z) T_f(x, y, z) dy dz}{\iint_S u_f(x, y, z) dy dz} \tag{5.9}$$

For example, Tenneti et al. (2013) used this temperature to compute the local Nusselt number.

$$Nu(x) = \frac{\dot{q}(x) d_p}{k_f P(< T_f(x) > -T_s)} \tag{5.10}$$

Here, P is the perimeter obtained by cutting the particles with the plane at location x and $\dot{q}(x)$ is the total interphase heat transfer rate per unit length of the fluid particle interface in the plane (Tenneti et al., 2013). The average Nu number for an assembly of spheres is obtained by averaging Eq. (5.10) along the streamwise direction (Eq. (5.11)).

$$Nu = \frac{1}{N}\sum_{i=1}^{N} Nu(x_i) \tag{5.11}$$

where N is the number of planes along the streamwise direction.

An alternative approach to calculate the average Nu number is to compute first the Nu number of the individual particles. The Nu number of the i-th particle is calculated as:

$$Nu_i = \frac{\dot{q}_i d_p}{\pi d_p^2 (\overline{T}_f - T_s) k_f} \tag{5.12}$$

In equation (5.12), $\vec{T}_f$ is the local average fluid temperature, $\dot{q}_i$ is the heat transfer rate between particle i and the surrounding fluid:

$$\dot{q}_i = -\iint_{S_{pi}} k_f \nabla T_f \cdot \vec{n} ds \tag{5.13}$$

$$\overline{T}_f = \frac{\iiint_{V_b} u_{f,x}(x,y,z) T_f(x,y,z) dxdydz}{\iiint_{V_b} u_{f,x}(x,y,z) dxdydz} \tag{5.14}$$

where S_{pi} is the surface of the i-th particle, V_b is a cubic box, the centre of which has the same position as the centre of gravity of the particle. $u_{f,x}$ is the fluid velocity in x direction. In this work, the size of the box was $3d_p$. The average Nu number of the packed bed is then obtained as:

$$Nu = \frac{1}{N_p}\sum_{i=1}^{N_p} Nu_i \tag{5.15}$$

where N_p is the number of particles in the assembly. It should be pointed out that other definitions of T_{f-ave} are also used in literature. For instance, Feng et al. (2014) took the initial fluid temperature as T_{f-ave} to calculate Nu numbers in fluidized beds. It was reported that the bed expansion and the fluid superficial velocity are

significantly affected by the overall average Nu number. The Nu number was greater for higher bed expansions since the cool fluid was able to penetrate deeper into the bed. However, increasing the superficial velocity of the fluid did not only increase the bed expansion but also enhanced the forced convection. Therefore, the relationship between bed expansion and the average Nu number in fluidized beds is still unclear.

5.4 Nusselt number of randomly packed beds and fluidized beds

Based on experimental data and theoretical analysis, Gunn (1978) proposed a Nusselt number correlation for fixed and fluidized beds:

$$Nu = (7-10\varepsilon+5\varepsilon^2)(1+0.7\,\mathrm{Re}^{0.2}\,\mathrm{Pr}^{1/3})+(1.33-2.4\varepsilon+1.2\varepsilon^2)\,\mathrm{Re}^{0.7}\,\mathrm{Pr}^{1/3} \quad (5.16)$$

where ε is the bed voidage. The Gunn's correlation is valid for voidages in the range 0.35-1.0 and Reynolds numbers up to 10^5. Wakao et al. (1979) proposed the following Nusselt number correlation for packed beds:

$$Nu = 2+1.1\,\mathrm{Re}^{0.6}\,\mathrm{Pr}^{1/3} \quad (5.17)$$

Equation (5.17) is valid for voidage 0.4. As we have outlined above, the confidence of Eqs. (5.16) and (5.17) for $\mathrm{Re} < 100$ is low (Shen et al., 1981).

Figure 5.1 sketches the computational set-up of Tavassoli et al. (2015) to model gas-solid heat transfer. At the inlet, a uniform velocity profile and constant temperature are assigned to the gas. At the outlet, the derivative of the velocity and temperature in the x direction is zero. Periodic boundary conditions are applied in the y and z directions. The particles are homogeneously distributed in the packed section. As the gas flows over the hot particles, the gas is continually heated up along the x direction. The overall average Nu number for the whole domain can then be calculated as:

$$Nu = A\overline{Nu}_{0-h_0}+(1-A)\overline{Nu}_{h_0-h} \quad (5.18)$$

The first term of Eq. (5.18) is the contribution of the heat transfer in the transient region ($x < h_0$, thermally-developing region. h_0 is the minimum domain size for the flow to become thermally fully-developed) to the overall average Nu number. The second term is the contribution of the heat transfer in the thermally fully-developed region ($x > h_0$) to the overall, average Nu number. A is the weighting coefficient depending on the calculation method of the overall average Nu number. If the overall,

average *Nu* number is computed using Eq. (5.11), *A* is the ratio of the number of planes in the domain section $x < h_0$ to the number of planes in the whole domain in the *x* direction. On the other hand, if Eq. (5.15) is used to calculate the overall average *Nu* number, *A* is the ratio of the number of particles in the domain section $x < h_0$ to the number of particles in the whole domain. If $h_0 > h$ (*h* is the domain size), Eq. (5.18) only contains the first term leading to a larger average *Nu* number. In contrast, if $h_0 \ll h$, the first term in Eq. (5.18) can be neglected. As a result, the boundary effect in the x direction becomes negligible in this set-up.

Tavassoli et al. (2015) computed the average *Nu* number for random assemblies of 54 spheres using Eq. (5.11). To minimize the effect of domain boundaries, a certain fraction of the computational domain that is close to the inlet and outlet boundaries in the *x* direction was excluded from the calculation of the average *Nu* number based on the variation of *Nu(x)*. Using their numerical data, Tavassoli et al. (2015) re-assessed Gunn's equation (1978) and proposed the following correlation:

$$Nu = (7 - 10\varepsilon + 5\varepsilon^2)(1 + 0.1\,\mathrm{Re}^{0.2}\,\mathrm{Pr}^{1/3}) + (1.33 - 2.19\varepsilon + 1.15\varepsilon^2)\,\mathrm{Re}^{0.7}\,\mathrm{Pr}^{1/3} \quad (5.19)$$

Tenneti et al. (2013) used a periodic boundary condition for the temperature in the *x* direction. It was assumed that a statistically homogeneous, gas-solid flow is analogous to a fully developed pipe flow and hence, also the heat transfer in a statistically homogenous, gas-solid flow was expected to be an analogous to a thermally fully-developed flow in a pipe with isothermal walls. The heat ratio (r_h, ratio of the difference between the fluid temperature of the bulk and the particle temperature at the inlet to the difference between the temperature of the bulk fluid and the particle temperature at the outlet) and the dimensionless fluid temperature (ψ) were defined such that the periodic boundary condition can be applied to ψ. The calculation of these variables (i.e. r_h and ψ) and boundary condition are given below:

$$r_h = \frac{<T_f(0)> - T_s}{<T_f(L)> - T_s}$$

$$\psi(x, y, z) = \frac{T_f(x, y, z) - T_s}{<T_f(0)> - T_s}$$

$$\psi(0, y, z) = r_h \psi(L, y, z) \quad (5.20)$$

where *L* is the domain size in the *x* direction and $\langle T_f(0)\rangle$ and $\langle T_f(L)\rangle$ are obtained using Eq. (5.9). Once the heat ratio has reached a steady state, the temperature field was considered to be fully developed. Sun et al. (2015) extended Tenneti's work

(2013) and proposed a Nusselt number correlation for $1 \leq \mathrm{Re} \leq 100$ and $0 \leq \phi \leq 0.5$. The following correlation was proposed:

$$Nu = (-0.46 + 1.77\varepsilon + 0.69\varepsilon^2)/\varepsilon^3 + (1.37 - 2.4\varepsilon + 1.2\varepsilon^2)\,\mathrm{Re}^{0.7}\,\mathrm{Pr}^{1/3} \qquad (5.21)$$

However, it is currently not clear whether the analogy to pipe flow as proposed by Tenneti et al. (2013) can indeed predict accurately the heat transfer coefficient in packed beds. Comparing the *Nu* number predictions of the correlations of Tavassoli et al. (2013) and Sun et al. (2015) appreciable differences, in particular for low solids volume fractions ($\phi \leq 0.3$), are observed. Thus, in the current work, we employ a fully periodic domain for both velocity and temperature in three directions. The periodic boundary conditions can eliminate the effect of the inlet and outlet regions on the average *Nu* number.
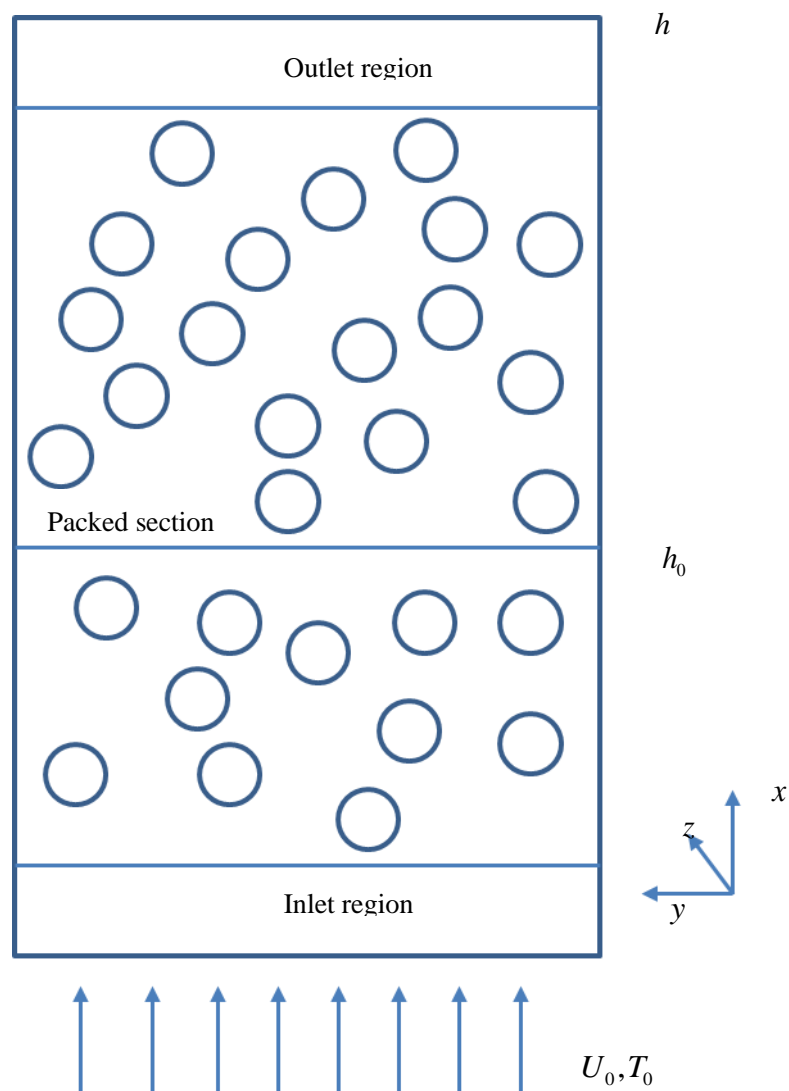

Figure 5.1. Schematic description of the computational domain used by Tavassoli et al. (2014)

5.5 Numerical method

5.5.1 Thermal lattice Boltzmann method

The thermal lattice Boltzmann method proposed by Peng et al. (2003) for incompressible flow is used here to solve the momentum and energy equations.

$$f_i(\vec{x}+\vec{e}_i\Delta t, t+\Delta t) = f_i(\vec{x},t) - \frac{\Delta t}{\tau_v}[f_i(\vec{x},t) - f_i^{eq}(\vec{x},t)] \qquad (5.22)$$

$$g_i(x+\vec{e}_i\Delta t, t+\Delta t) = g_i(x,t) - \frac{\Delta t}{\tau_c}[g_i(x,t) - g_i^{eq}(x,t)] \qquad (5.23)$$

where f_i and g_i are the density and energy distribution functions at time t and position $\vec{x}$ with velocity $\vec{e}_i$ and τ_v and τ_c are the relaxation times related to viscosity and thermal diffusivity, respectively. The superscript 'eq' denotes the equilibrium state. The D3Q19 and D3Q7 lattices are used for density and the energy distribution functions, respectively.

$$\vec{e}_i = \begin{cases} (0,0,0), & i=0 \\ (\pm1,0,0)c,(0,\pm1,0)c,(0,0,\pm1)c, & i=1...6 \\ (\pm1,\pm1,0)c,(\pm1,0,\pm1)c,(0,\pm1,\pm1)c, & i=7...18 \end{cases} \qquad (5.24)$$

Here c is the ratio of Δx to Δt and is set to 1. The equilibrium distributions for the density and energy distribution functions are given as:

$$f_i^{eq} = w_{i,v}\rho_f[1+3\frac{\vec{e}_i\cdot\vec{u}_f}{c^2} + \frac{9}{2}\frac{(\vec{e}_i\cdot\vec{u}_f)^2}{c^4} - \frac{3}{2}\frac{\vec{u}_f^{\,2}}{c^2}] \qquad (5.25)$$

$$g_i^{eq} = w_{i,c}\varphi(1+4\cdot\frac{\vec{e}_i\cdot\vec{u}_f}{c^2}) \qquad (5.26)$$

where

$$w_{i,v} = \begin{cases} \dfrac{1}{3}, & i=0 \\ \dfrac{1}{18}, & i=1...6 \\ \dfrac{1}{36}, & i=7...18 \end{cases} \qquad (5.27)$$

$$w_{i,c} = \begin{cases} \dfrac{1}{4}, & i = 0 \\ \dfrac{1}{8}, & i = 1...6 \end{cases} \qquad (5.28)$$

The macroscopic variables density, momentum and energy can be obtained through the following equations, respectively:

$$\rho_f = \sum_i f_i , \quad \rho_f \vec{u}_f = \sum_i f_i \vec{e}_i , \quad \varphi = \sum_i g_i \qquad (5.29)$$

The viscosity and thermal diffusivity are computed using the following expressions:

$$\nu = \frac{1}{3} c^2 (\tau_v - \frac{\Delta t}{2}) \qquad (5.30)$$

$$D = \frac{1}{4} c^2 (\tau_c - \frac{\Delta t}{2}) \qquad (5.31)$$

5.5.2 Boundary conditions for thermal lattice Boltzmann method

The immersed boundary condition proposed by Noble and Torczynski (1998) is implemented to enforce the no-slip boundary conditions for the fluid velocity at the particle surface. The thermal boundary condition for a Dirichlet boundary problem as proposed by Chen et al. (Chapter 4) is used to enforce a constant temperature at the particle surface. The evolution equation for the density and energy distribution functions are modified to account for the interaction between the solid and fluid phases:

$$f_i(\vec{x} + \vec{e}_i \Delta t, t + \Delta t) = f_i(\vec{x}, t) - \frac{\Delta t}{\tau_v}(1 - B_v)[f_i(\vec{x}, t) - f_i^{eq}(\vec{x}, t)] + B_v \Omega_{i,v}^p \qquad (5.32)$$

$$g_i(\vec{x} + \vec{e}_i \Delta t, t + \Delta t) = g_i(\vec{x}, t) - \frac{\Delta t}{\tau_c}(1 - B_c)[g_i(\vec{x}, t) - g_i^{eq}(\vec{x}, t)] + B_c \Omega_{i,c}^p \qquad (5.33)$$

where $\Omega_{i,v}^p$ and $\Omega_{i,c}^p$ are additional collision terms that bounce back the non-equilibrium parts of the density and energy distributions, respectively.

$$\Omega_{i,v}^p = f_{-i}(\vec{x}, t) - f_i(\vec{x}, t) + f_i^{eq}(\rho_f(\vec{x}, t), \vec{u}_p(\vec{x}, t)) - f_{-i}^{eq}(\rho_f(\vec{x}, t), \vec{u}_f(\vec{x}, t)) \qquad (5.34)$$

$$\Omega_{i,c}^{p} = -g_{-i}(\vec{x},t) - g_{i}(\vec{x},t) + g_{i}^{eq}(\varphi_{s},\vec{u}_{f}(\vec{x},t)) + g_{-i}^{eq}(\varphi(\vec{x},t),\vec{u}_{f}(\vec{x},t)) \qquad (5.35)$$

$\vec{u}_{p}$ is the particle velocity at position $\vec{x}$, φ_{s} is the temperature of the particle and B_{v} and B_{c} are weighting functions, which can be calculated as follows:

$$B_{v}(\phi_{x},\tau_{v}) = \frac{\phi_{x}(\dfrac{\tau_{v}}{\Delta t} - \dfrac{1}{2})}{(1-\phi_{x}) + (\dfrac{\tau_{v}}{\Delta t} - \dfrac{1}{2})} \qquad (5.36)$$

$$B_{c}(\phi_{x},\tau_{c}) = \frac{\phi_{x}(\dfrac{\tau_{c}}{\Delta t} - \dfrac{1}{2})}{(1-\phi_{x}) + (\dfrac{\tau_{c}}{\Delta t} - \dfrac{1}{2})} \qquad (5.37)$$

Here ϕ_{x} is the local solids volume fraction of a lattice that is covered (partially or fully) by the solid particles. The hydrodynamic boundary condition has been comprehensively validated for single spheres and assemblies of spheres and applied to calculate the drag force for cubic particles (Chen et al., 2015; Chen et al., Chapter 3). The thermal boundary condition has been shown to have second order accuracy (Chen et al., Chapter 4).

5.5.3   Validation of the thermal lattice Boltzmann method

For validation, the Nusselt numbers of a single sphere and a linear array of spheres are calculated and compared with previous simulation results. The first test is a hot sphere in a uniform flow. The domain size is $240 \times 120 \times 120$. The particle diameter is 15 in lattice units. The temperature of the particle is set to 1. The initial temperature of the fluid is set to 0. The Prandtl number is 0.744. A uniform velocity and a constant temperature of the fluid are specified at the inlet. At the outlet, the derivative of the velocity and temperature of the fluid in the x direction is set to zero. At the side boundaries, symmetry boundary conditions are imposed for the velocity and temperature. Fitting experimental data, Whitaker (1972) proposed the following Nusselt number correlation for a single sphere:

$$Nu = 2 + (0.4\,\mathrm{Re}^{1/2} + 0.06\,\mathrm{Re}^{2/3})\,\mathrm{Pr}^{0.4} \qquad (5.38)$$

Figure 5.2 plots the results of the LBM simulations and the predictions of the Whitaker (1972) correlation. A good agreement is observed. Richter et al. (2012) used a commercial finite volume solver (ANSYS FLUENT) to calculate the Nu number for

a single sphere in a uniform flow. The predicted *Nu* numbers are slightly higher than our predictions (relative deviation is 5%), nonetheless, the agreement is good.
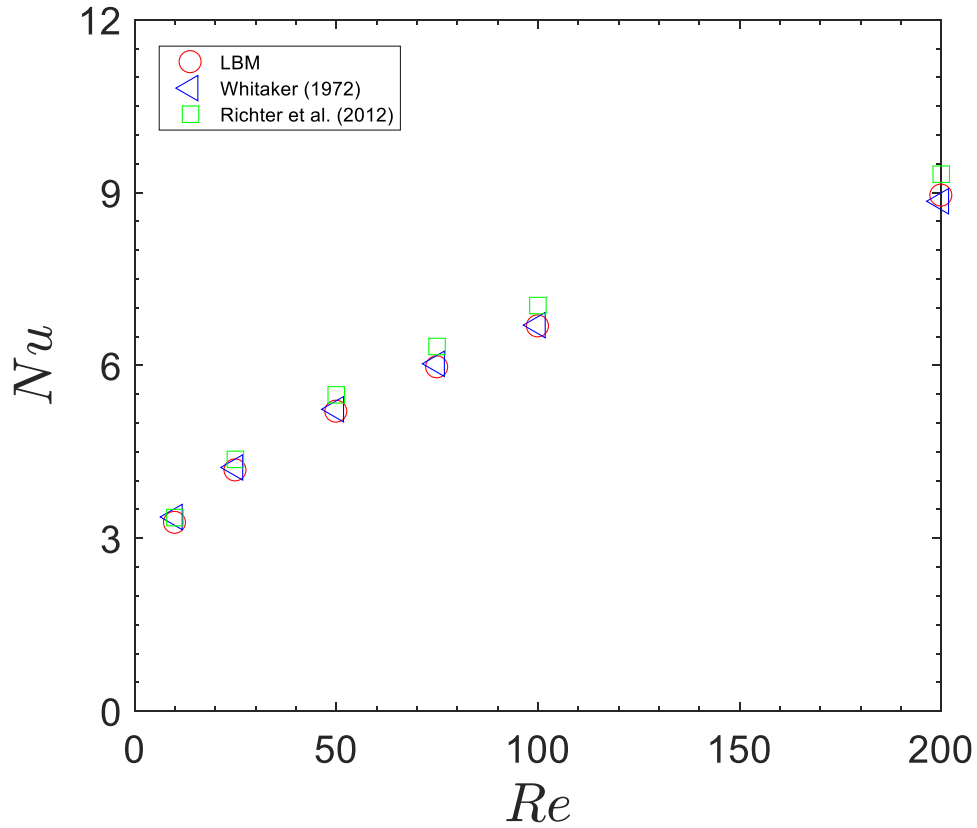

Figure 5.2. Nusselt number for a single sphere in a uniform flow as a function of Reynolds number.

The second validation test conducted was the calculation of the *Nu* number for a linear array of spheres in a uniform flow (Figure 5.3). Ramachandran et al. (1989) computed the Nusselt number for a linear array of spheres using a finite element method. Tavassoli et al. (2013) simulated the same problem to validate their immersed boundary method. Here the domain size and particle diameter in lattice units are identical to the settings of Tavassoli et al. (2013). The centre to centre distance s between the spheres is set to $2d_p$ or $4d_p$. The diameter of the particle is 15 in lattice units. The Prandtl number is 0.74. The numbers of lattices nodes are $150 \times 150 \times 195$ and $150 \times 150 \times 255$ for $s = 2d_p$ and $s = 4d_p$, respectively. The leading sphere is $4.5d_p$ away from the inlet, and the third sphere is $4.5d_p$ away

from the outlet. Uniform velocity and constant temperature are assigned to the fluid at the inlet. At the outlet, the derivatives of the velocity and the temperature in the x direction are set to zero. The temperature of the particles is set to 1 and the initial fluid temperature is set to 0. Symmetry boundary conditions for the velocity and temperature are specified at the side boundaries. The Nu number for each particle is calculated using Eqs. (5.12) and (5.13). $\bar{T}_f$ is the temperature difference between the particle and the initial fluid temperature. Table 5.1 reports the calculated Nu numbers for each sphere together with the simulation results of Ramachandran et al. (1989) and Tavassoli et al. (2013). The results show that the shielded particles have a smaller Nu number. This is due to the interactions between the wake of the first sphere and the flow over the shielded particles. Comparing our data to the results of Ramachandran et al. (1989) shows good agreement. The small differences may be due to differences in grid resolution. Ramachandran et al. (1989) used a non-uniform grid with a very fine grid in the proximity of the particles to resolve the boundary layer of the particles. In addition, the lengths of the inlet and outlet regions may affect the simulation results as well. The discrepancy between our data and Tavassoli et al. (2013) is about 4-8% for the first and third spheres for $Re = 50$. The LBM data are closer to the simulation results of Ramachandran et al. (1989). From the comparisons above, we conclude that the lattice Boltzmann method reported here reproduces accurately a series of reference simulations.
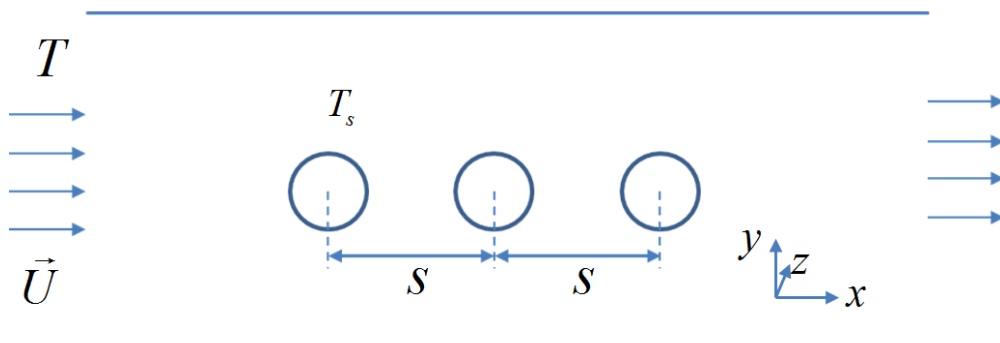

Figure 5.3. Schematic description of the computational set up.

Re	s/d_p	LBM			Ramachandran et al. (1989)			Tavassoli et al. (2013)		
		1st	2nd	3rd	1st	2nd	3rd	1st	2nd	3rd
10	2	3.33	2.35	2.16	3.37	2.32	2.03	3.45	2.40	2.21
10	4	3.42	2.78	2.58	3.28	2.79	2.49	3.51	2.83	2.62
50	2	5.31	3.38	3.03	5.50	3.39	2.98	5.72	3.55	3.19
50	4	5.42	4.01	3.63	5.40	4.18	3.60	5.80	4.21	3.81

Table 5.1. Nusselt number for a linear array of three spheres in a uniform flow.

5.6 Simulations and Results

In this work, packings of spheres were generated by randomly distributing spheres in cubic, periodic domains using a Monte Carlo method (Frenkel and Smit, 1996). $N_p = 54$ particles were placed in the domain for $\phi \leq 0.4$, while $N_p = 61$ particles were used for $\phi > 0.4$. The Prandtl number was 0.7. The diameter of the particles was varied in the range from 22 to 42 in lattice units. For $\phi > 0.3$, the particle diameter was larger than 35 in lattice units. For each given Reynolds number and solids volume fraction, 6-12 different configurations were modelled and the values obtained were averaged. The method for assigning a steady state *Nu* number as proposed by Yang et al. (2011) was adopted. When the change of the *Nu* number in the final 20% of the computational time was less than 1%, the computation was assumed to have reached a steady state. Figure 5.4 plots the *Nu* number as a function of simulation time (The time is normalized by d_p/u_s). The high *Nu* number at the start of the simulation is due to the large temperature gradient at the particle fluid interface when initiating the heat transfer. The particle Nusselt number (Nu_i) along the *x* direction for $Re = 50$ and $\phi = 0.4$ at time 10 is plotted in Figure 5.5, which confirms that at the given time the flow was thermally fully-developed.

In the first set of simulations, we tested the effect of domain "shape" on the average *Nu* number. A cuboid domain of size $350 \times 100 \times 100$ was used to simulate $Re = 10$ and $\phi = 0.3$. The average *Nu* number for six different particle configurations was 4.93, while the average *Nu* number for a cubic domain of size 150^3 was 4.89 (the deviation between these two different numerical set-ups is within 1%). Hence we conclude that the simulation results are not affected by domain shape. Second, the effect of domain size on the *Nu* number calculated was assessed. Three different domain sizes are used for $\phi = 0.4$ and $Re = 10$. The average Nusselt numbers for domain size $130 \times 130 \times 130$, $150 \times 150 \times 150$ and $160 \times 160 \times$

160 were 5.53, 5.34 and 5.31, respectively. Hence, in the following we used a domain size of 150^3 for solids volume fractions 0.1 and 0.2, while domain sizes of 155^3, 160^3 and 165^3 were used for solids volume fractions of 0.3, 0.4, and 0.5, respectively.
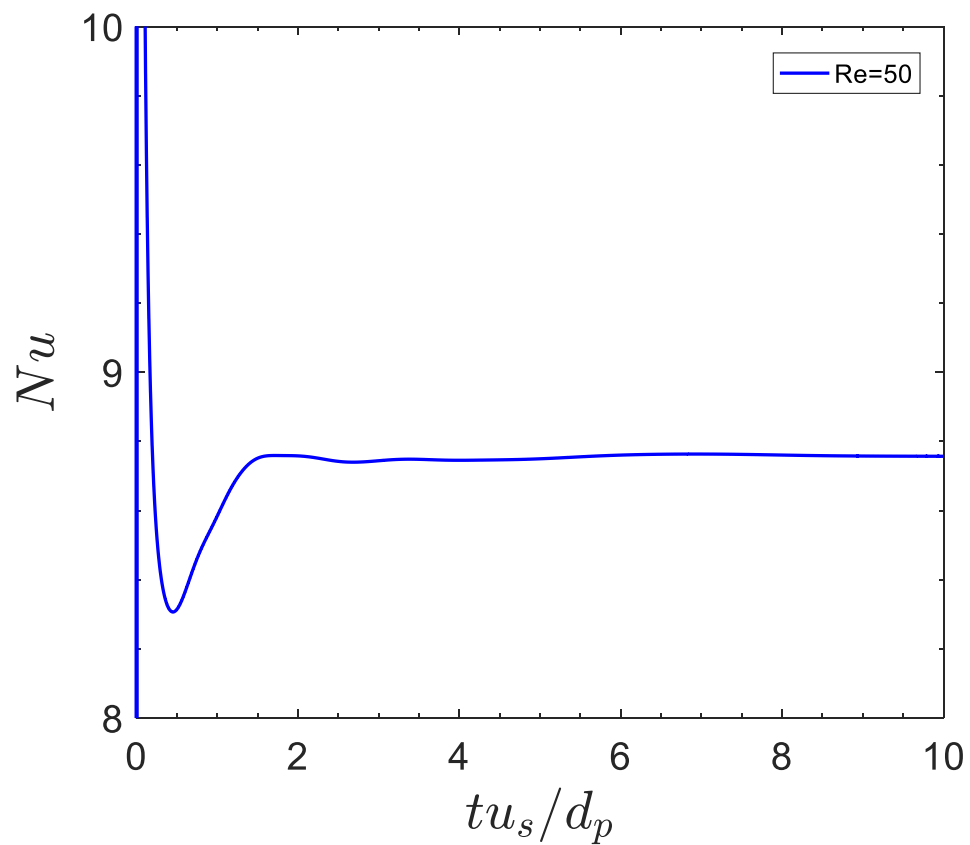

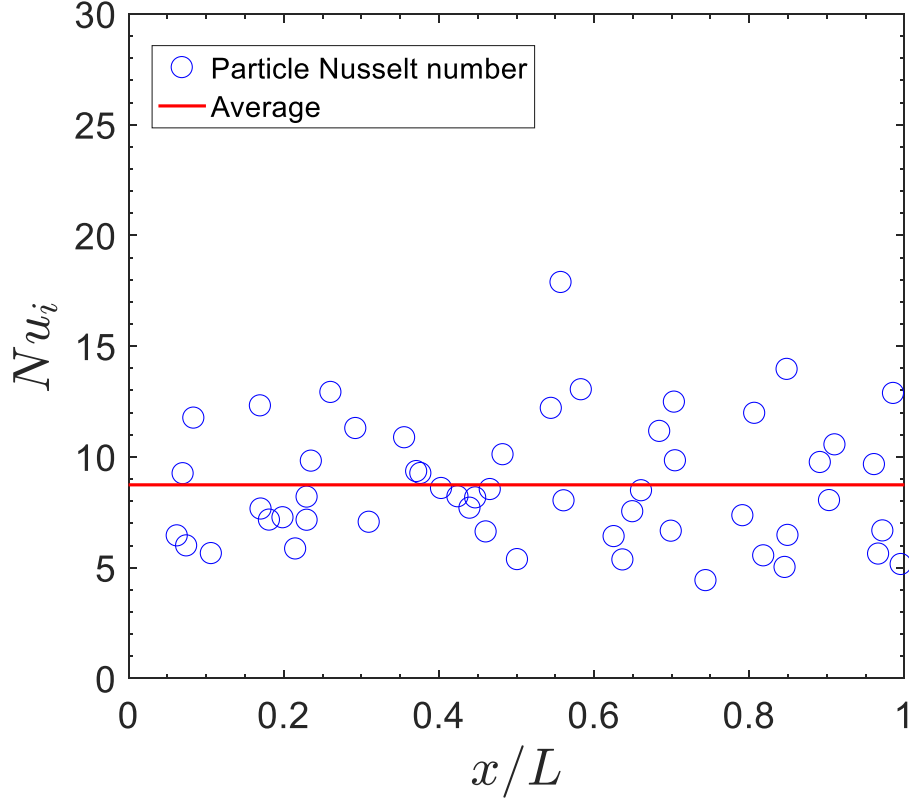Figure 5.4. Nusselt number as a function of simulation time for $\phi = 0.4$. The Prandtl number is 0.7.

Figure 5.5. The particle Nusselt number along the x direction at $\frac{tu_s}{d_p} = 10$ for

$\mathrm{Re} = 50$ and $\phi = 0.4$. The Prandtl number is 0.7.

Figure 5.6 shows an example of the temperature distribution in three planes within a random assembly of spheres. The average Nu number obtained from these simulations is plotted as a function of Reynolds number in Figure 5.7. It was possible to fit well our simulation data for assemblies of spheres to the following correlation:

$$Nu = 2 + 0.77\phi + 0.64\phi^2 + (0.6 + 1.1\phi)\,\mathrm{Re}^{0.5}\,\mathrm{Pr}^{1/3} \qquad (5.39)$$

It is worth noting that if $\phi = 0$, Eq. (5.39) reduces to the well-known Froessling equation (1938) for the Nu number of a single sphere in unbounded flow. In the literature, there is currently no consensus about the Nu number as a function of the solids volume fraction at low Reynolds numbers for random particle assemblies. For instance, at $\mathrm{Re} = 0$, Gunn's equation (1978) reduces to:

$$Nu = 7 - 10\varepsilon + 5\varepsilon^2 \qquad (5.40)$$

For $\varepsilon = 0.4$, Eq. (5.40) is equal to 3.8, whereas Wakao's equation (Wakao et al., 1979) is equal to 2. Since the particles and surrounding fluid are almost in thermal equilibrium for $Re \leq 10$, it is very difficult to accurately measure experimentally the *Nu* number in the Stokes regime (Shen et al., 1981). Hence, it is hoped that the numerical simulation results for $Re = 1$ reported here can provide a good estimate for the *Nu* number in the Stokes regime. The functional form of the Reynolds number independent and dependent terms of Eq. (5.39) are polynomial expressions of the solid volume fraction ϕ and show some similarity to Gunn's equation (1978). The coefficients were determined by minimizing the difference between the correlation and the simulation data.
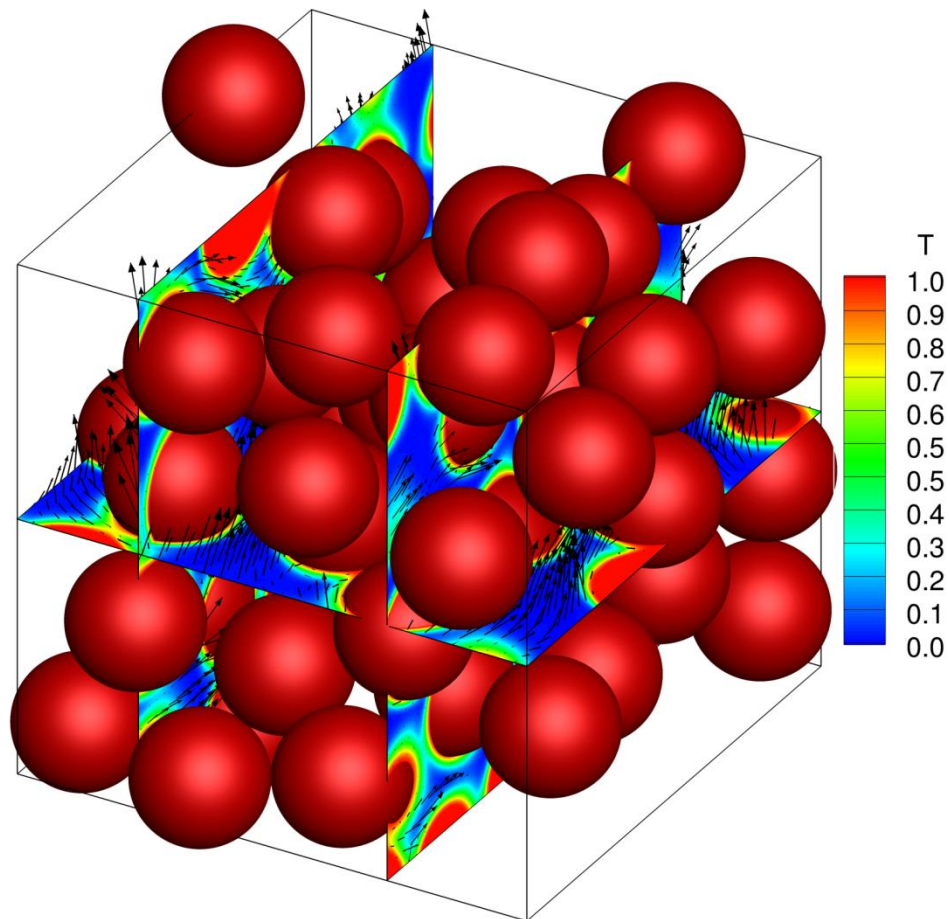

Figure 5.6. Example of the temperature distribution in a random assembly of spheres ($Re = 50$ and $\phi = 0.4$). The Prandtl number is 0.7.
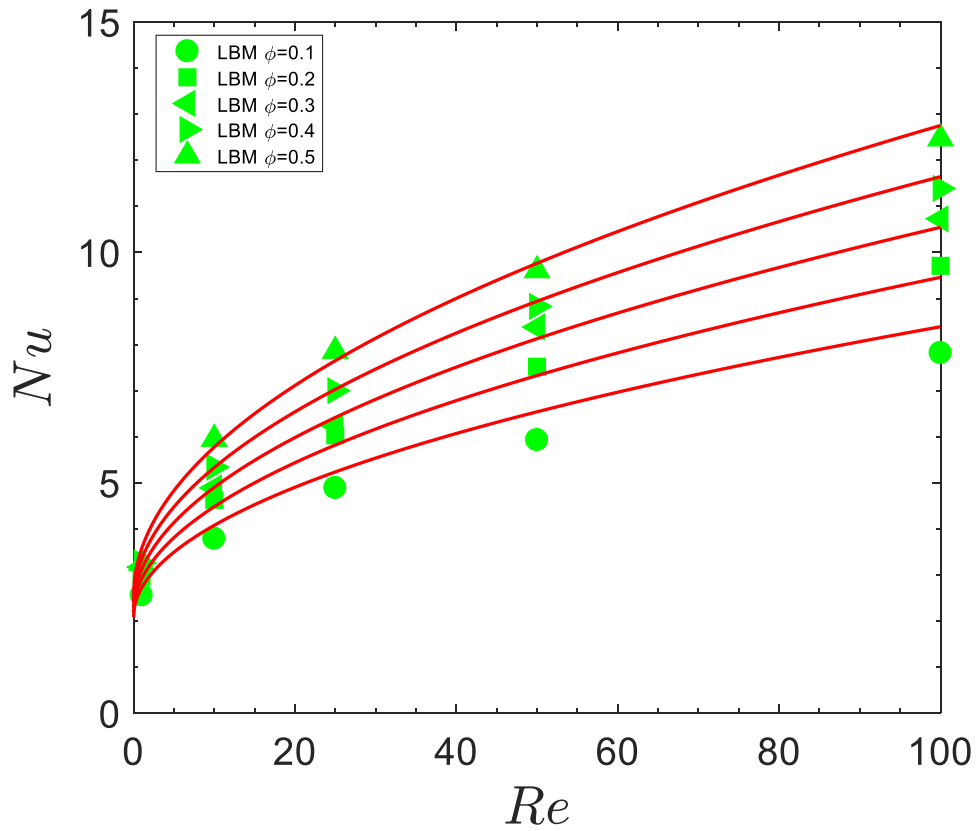
Figure 5.7. Nusselt number as a function of Reynolds number. The lines plot Eq. (5.39). The Prandtl number is 0.7.

Figure 5.8 compares Gunn's equation and equation (5.39) with our LBM simulation data for solid volume fractions 0.1, 0.3 and 0.5. Generally, the trend of the simulation data is consistent with Gunn's equation (Gunn, 1978) for $\text{Re} \leq 100$. However, Gunn's equation over-predicts the Nu number, in particular for $\phi = 0.5$. The maximum relative difference between Gunn's equation and the simulation data are 29% and 20% for a solid volume fraction of 0.1 and 0.3, respectively. The highest deviations are observed for Reynolds numbers in the range 1 - 10. A possible reason for this observation is that Gunn's equation was obtained from experimental data that differed by several orders of magnitude at a given (small) Reynolds number ($\text{Re} \leq$ 10). At high Reynolds numbers, the agreement between the LBM data and Gunn's equation is good for solid volume fractions 0.1 and 0.3. For a solid volume fraction of

0.5, the difference between Gunn's equation and the LBM data is, however, again considerable, i.e up to 61%. Tavassoli et al. (2015) also reported that Gunn's equation is only accurate for low solid volume fractions for $\text{Re} \leq 100$, i.e. $\phi < 0.3$.
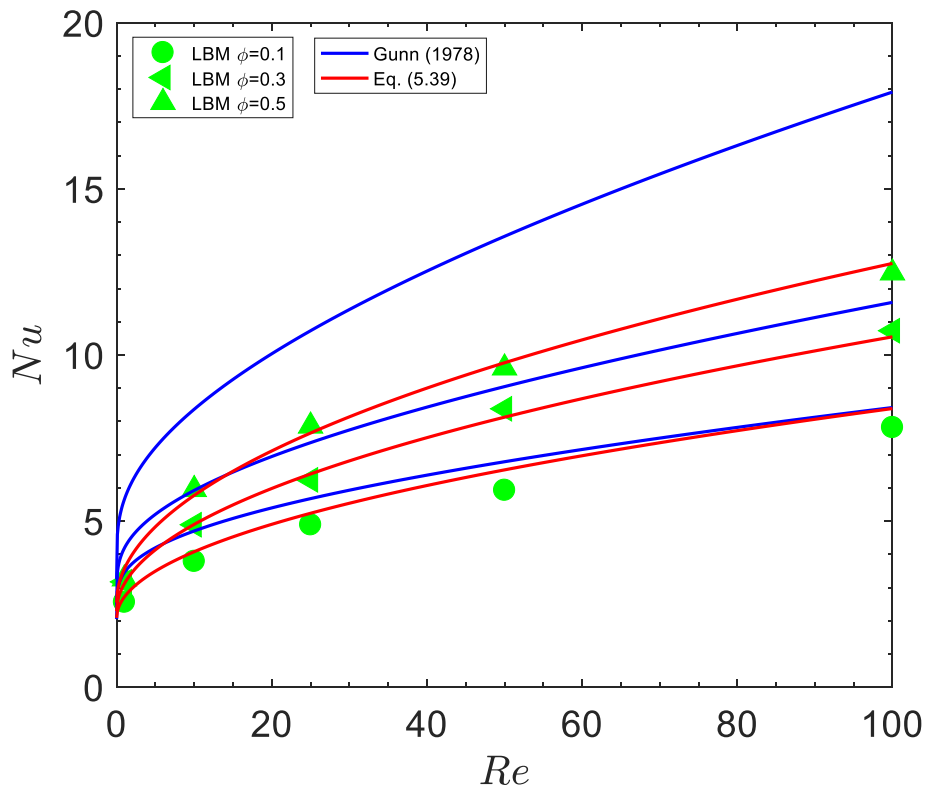
Figure 5.8. Comparison of the Nusselt number as predicted by Gunn's equation (Gunn, 1978), equation (5.39) and simulation data. The Prandtl number is 0.7.

Figure 5.9 compares the *Nu* number predicted by Tavassoli et al. (2015), Sun et al. (2015) and equation (5.39) for a solid volume fraction of 0.1, 0.3 and 0.5. Generally, the correlation of Tavassoli shows a good agreement with the LBM data for solid volume fractions 0.1 and 0.3. It is worth noting that the smallest Reynolds number Tavassoli et al. (2015) simulated was 10. Thus, predictions of the *Nu* number for small Reynolds numbers (Re < 10) using Tavassoli et al.'s (2015) correlation is, unsurprisingly, associated with some error (8%). At high Reynolds numbers (Re > 60), the prediction by Tavassoli et al. (2015) is slightly higher than our LBM data for solid volume fractions 0.1 and 0.3. However, the difference between the *Nu* number

as obtained from LBM simulations and the equation of Tavassoli et al. (2015) for a solid volume fraction of 0.5 is again considerable for Re > 20. The observations summarized above can be rationalized as follows. For small solid volume fractions ($\phi \leq 0.3$) or small Reynolds numbers (Re $\leq$ 20), the thermally developing region h_0 is small when compared to the domain size *h*. Since some part of the computational domain in the *x* direction was excluded in Tavassoli's work (Tavassoli, 2014) from the calculation of the average *Nu* number based on the variation in $Nu(x)$, the predictions of Tavassoli et al. (2015) agree well with our LBM data. At high solid volume fractions and Reynolds numbers, h_0 may be under-estimated by Tavassoli et al. (2014). As a result, the difference between the correlation of Tavassoli et al. (2015) and our LBM data becomes appreciable. Furthermore, we also observe that the difference between the average *Nu* number as predicted by Sun et al. (2015) and our LBM data is considerable for all solid volume fractions and Reynolds numbers. This may be due to the fact that the proposed analogy between a fully-developed thermal pipe flow with isothermal walls and a packed bed is somewhat inaccurate, and thus the boundary conditions applied in the simulations are not realistic for a packed bed configuration (Sun et al., 2015).
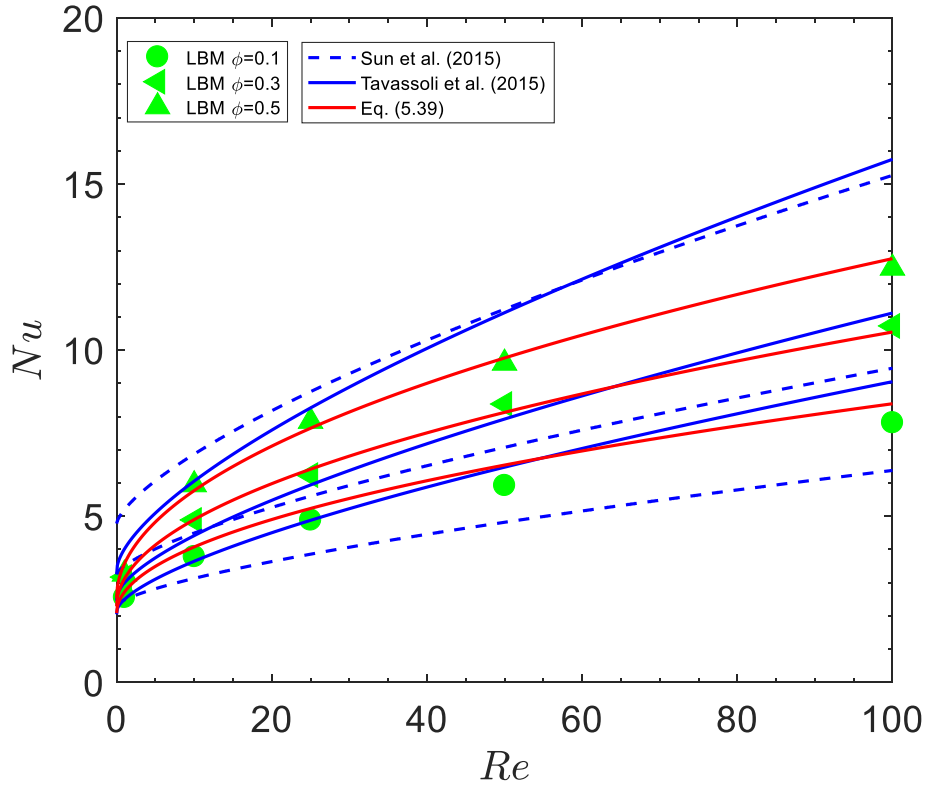
Figure 5.9. Comparison of the predictions of Sun et al. (2015) and Tavassoli et al. (2015) with Eq. (5.39) for solid volume fractions of 0.1, 0.3 and 0.5. The Prandtl number is 0.7.

Finally, the numerically derived Nusselt number correlations (i.e. Tavassoli et al., 2015, Sun et al., 2015 and Eq. (5.39)) were compared with the empirical correlation (experimentally derived) proposed by Wakao et al. (1979) which is only valid for dense packings ($\varepsilon = 0.4$) and the simulation results of Guardo et al. (2005) for $\phi = 0.6$ and $Pr = 0.71$. Guardo et al. (2005) computed the Nu number for a packed bed comprising 44 spheres and a sphere-to-tube diameter ratio of 3.923 using a Reynolds-averaged Navier-Stokes model for $Re < 1000$. In figure 5.10, we observed that the predictions of Tavassoli et al. (2015) and Sun et al. (2015) are higher than the values determined by Wakao et al. (1979), while the predictions of Eq. (5.39) are lower than those predicted by Wakao et al. (1979). However, there is good agreement between the predictions of equation (5.39) and Wakao et al. (1979) for

Re < 30. As the Reynolds number increases, the discrepancy between equation (5.39) and Wakao et al. (1979) increases. The maximum discrepancy is 14%. The numerical results of Guardo et al. (2005) agree well with the predictions by Eq. (5.39). The comparison shown in Figure 5.10 indicates that Eq. (5.39) can estimate accurately the Nu number for packed beds with porosity 0.4.
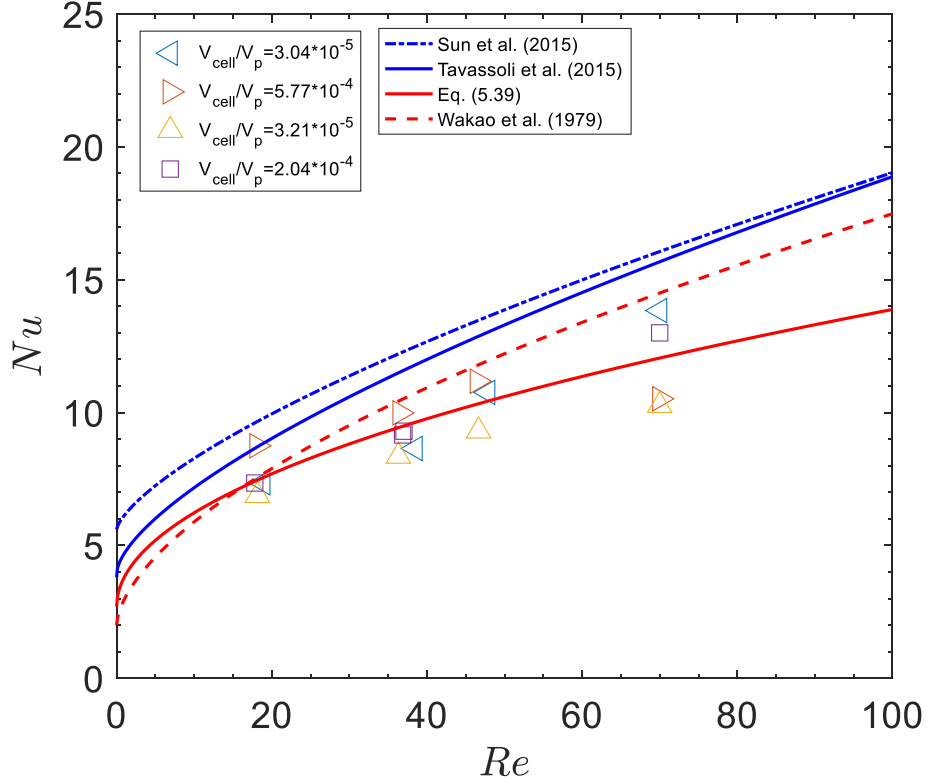
Figure 5.10. Comparison of the different numerically derived Nusselt number correlations with the empirical correlation of Wakao (Wakao et al., 1979). The symbols give the simulation results extracted from Figure 6 of Guardo et al. (2006). V_{cell} and V_p are the grid and particle volumes in the respective simulations.

5.7   Conclusions

In this work, a thermal lattice Boltzmann method using an immersed moving boundary approach was used to compute the average Nu number for assemblies of spheres for a wide range of solid volume fractions and Re ≤ 100. Fully periodic boundary conditions for the fluid velocity and temperature were applied at all domain boundaries for the fluid to generate thermally fully-developed flows, a key difference

to previous attempts.   The newly proposed Nusselt number correlation has been compared to experimentally and numerically derived correlations. The experimentally derived correlations (Gunn, 1978; Wakao et al., 1979) significantly over-predict the average *Nu* number for assemblies of spheres for Re ≤ 100. The reason for this is that the experimentally derived correlations are valid for a wide range of Reynolds numbers (10^4-10^5), the confidence of these correlations (e.g. Gunn, 1978) are low for Re ≤ 100 (Shen et al., 1981). The numerically derived correlations (Tavassoli et al., 2015; Sun et al., 2015) are influenced by the boundary conditions applied. At high solid volume fractions and Reynolds numbers, the flows in Tavassoli et al.'s (2015) simulations are thermally not fully-developed yielding a higher average *Nu* number. In addition, the analogy between a thermally fully-developed pipe flow with isothermal walls and a packed bed (Sun et al., 2015) is probably not valid to determine the heat transfer in random assemblies of spheres. The correlation for the Nusselt number for assemblies of spheres proposed here is based on the simulation data obtained from thermally fully-developed flows. We expect that the new Nusselt number correlation introduced here will improve the accuracy of Euler-Euler and Euler-Lagrangian simulations of non-isothermal gas-solid flows.

6

Heat transfer to gas in random assemblies of cubes: the effect of solid volume fraction on the average Nusselt number for $Re \leq 100$

6.1 Abstract

The thermal lattice Boltzmann method with immersed moving boundary conditions was employed to calculate the particle-to-fluid heat transfer in an assembly comprising super-quadric cubes. The simulations were performed for solid volume fractions 0.1-0.45 for $Re_V \leq 100$ (based on the volume equivalent diameter of the cube). Defining the Reynolds number based on the hydraulic diameter of the packing (Re_h), the Nusselt number correlation (Chapter 5) proposed for assemblies of spheres was transformed into a form that is a function of Re_h. The new Nusselt number correlation can fit the simulation data for assemblies of super-quadric cubes fairly accurately if the Sauter diameter was chosen as the characteristic size of the particle.

6.2 Introduction

Gas solid non-isothermal flows are encountered widely in industrial applications, e.g. catalytic reactors. Understanding the complicated flows and thermal phenomena is essential to design and control the process. Therefore, empirical correlations as a function of Reynolds number, solid volume fraction and Prandtl number have been developed to quantify the heat transfer between particles and surrounding fluids. Gunn (1978) proposed a Nusselt number correlation valid for a single particle, packed beds and fluidized beds for Reynolds numbers up to 10^5 based on the theoretical solution and experimental measurements of the Nusselt number for packed and fluidized beds. Tavassoli et al. (2014) identified that Gunn's equation (1978) was valid for $\phi < 0.3$. Chen et al. (Chapter 5) also showed that Gunn's equation (1978) agreed well with the simulation data for $\phi < 0.3$. At high solid volume fraction, Gunn's equation (1978) significantly over predicts the Nusselt number for packed bed for $Re < 100$ (based on the sphere diameter). Wakao et al. (1979) proposed a Nusselt number correlation based on the experimental data as a function of Reynolds number and Prandtl number for packed bed. The solid volume fraction was not explicitly incorporated into the correlation. Scott et al. (2004) measured the heat

transfer to a single sphere immersed in beds of particles supplied by gas in packed and fluidized beds. Based on the experimental data, a Nusselt number correlation for an immersed sphere was proposed as a function of minimum fluidization velocity and diameter ratio of the immersed sphere to the particles in the bed. However, the empirical correlations rely on the macroscopic experimental measurements which ignore the effect of local flow structure on the heat transfer. Romkes et al. (2003) simulated particle-to-fluid heat transfer in a packed bed with different channel-to-particle diameter ratios using a commercial computational fluid dynamics software and showed that the local packing structure significantly affects the overall heat transfer in a packed bed. Guardo et al. (2005) computed the Nusselt number for packed bed comprising 44 spherical particles and a sphere-to-tube diameters ratio of 3.923 using Reynolds-averaged Navier-Stokes model for $\mathrm{Re} < 1000$. The comparison with Wakao et al. (1979) demonstrated that Wakao's equation over predicts the Nusselt number in the Reynolds number range from 10 to 100. Deen et al. (2012) simulated randomly packed beds comprising 1326 spheres for heat transfer using the immersed boundary method for solid volume fraction 0.3 and Prandtl number 0.8. The results indicated that Gunn's equation (1978) over predicted the heat transfer coefficients for packed beds for $\mathrm{Re} < 100$. The comparisons of Nusselt number with empirical correlations and experiments (Romkes et al., 2003; Guardo et al., 2005; Deen et al., 2012) indicates that computational fluid dynamics is a reliable tool to predict particle-to-fluid heat transfer in packed beds.

Recently, direct numerical simulations have been used to calculate the average Nusselt number for random assemblies of spheres. Tavassoli et al. (2015) proposed a Nusselt number correlation for assemblies of spheres for Reynolds number 0-100 and solid volume fraction 0.1-0.6 based on direct numerical simulations. In the simulations, Tavassoli et al. (2013, 2015) applied uniform velocity and constant temperature to the fluid at the inlet. At the outlet, the normal derivatives of the velocity and temperature were set to zero. Periodic boundary conditions were specified at the other domain boundaries. The particles were homogeneous distributed in the bed. As the gas flowing over the hot particles, the gas is continually heated along the streamwise direction. Such flow includes a thermally developing entrance region and a thermally fully developed region. In the thermally developing entrance region, the heat transfer of particles has a significant contribution to the overall average Nusselt number, which however results in a large overall average Nusselt number especially at high solid volume fractions and Reynolds numbers. The method was then extended to calculate the heat transfer coefficients for assemblies of spherocylinders (Tavassoli et al., 2015). The Nusselt number correlation for assemblies of spheres was shown to be able to predict the average Nusselt number for

assemblies of spherocylinders if the proper effective diameter (diameter of the spherocylinder) was chosen to characterize the particle to fluid heat transfer. However, the diameter of the spherocylinder cannot distinguish the effect of aspect ratio (ratio of the length of the spherocylinder to the diameter of the spherocylinder) on the heat transfer coefficient.

Sun et al. (2015) using particle-resolved direct numerical simulations developed a Nusselt number correlation for Reynolds numbers 1-100 and solid volume fractions 0-0.5 for assemblies of spheres. The critical assumption which was made in their work is that the heat transfer in statistically homogenous gas-solid flow is expected to be analogous to single phase thermally fully-developed flow in pipes with isothermal walls. The difference of predicted Nusselt number using Tavassoli et al. (2015) and Sun et al. (2015) is considerable. Sun et al. (2015) stated that the difference was due to the different boundary conditions applied in the simulations.

Chen et al. (Chapter 5) proposed a Nusselt number correlation based on the direct numerical simulations of gas-solid flows. The domain boundary conditions for fluid velocity and temperature were fully periodic. The comparison of average Nusselt numbers predicted by Tavassoli et al. (2015) and Chen et al. (Chapter 5) is good for $\phi < 0.3$. For high solid volume fraction, the discrepancy between Tavassoli et al. (2015) and Chen et al. (Chapter) increases with increasing Reynolds number which is due to the particle to fluid heat transfer in thermally developing region. The comparison with Sun et al. (2015) shows that the predictions by Sun et al. (2015) are very different from the predictions by Chen et al. (Chapter 5) in the whole range of Reynolds number and solids volume fraction. It is possible that the analogy between thermally fully-developed pipe flow with isothermal walls and packed bed is questionable, and thus the boundary conditions applied in the simulations of Sun et al. (2015) are problematic.

In this work, fully periodic boundary conditions for fluid velocity (Eq. (6.1)) and temperature (Eq. (6.2)) are applied to the domain boundaries for fluid.

$$u_{f,x}(0, y, z) = u_{f,x}(L_x, y, z)$$

$$u_{f,y}(x, 0, z) = u_{f,y}(x, L_y, z)$$

$$u_{f,z}(x, y, 0) = u_{f,z}(x, y, L_z) \tag{6.1}$$

$$T_f(0, y, z) = T_f(L_x, y, z)$$

$$T_f(x,0,z) = T_f(x,L_y,z)$$

$$T_f(x,y,0) = T_f(x,y,L_z) \tag{6.2}$$

where $u_{f,x}$, $u_{f,y}$ and $u_{f,z}$ are the fluid velocity in x, y and z directions, respectively. L_x, L_y and L_z are the domain size in x, y and z directions, respectively. T_f is the temperature of fluid. The periodic boundary conditions can eliminate the effect of the inlet and outlet regions on the average Nusselt number. The goal is to assess whether the Nusselt number correlation for assemblies of spheres can be applied to predict the particle to fluid heat transfer for assemblies of super-quadric cubes.

6.3 Governing equations

The flow is assumed to be incompressible and the viscous heat dissipation is neglected. Therefore, the Navier-Stokes and energy equations are as follows:

$$\rho_f(\frac{\partial \vec{u}_f}{\partial t} + \vec{u}_f \cdot \nabla \vec{u}_f) = -\nabla p + \mu_f \nabla^2 \vec{u}_f \tag{6.3}$$

$$\rho_f c_{pf}(\frac{\partial T_f}{\partial t} + \vec{u}_f \cdot \nabla T_f) = k_f \nabla^2 T_f \tag{6.4}$$

Where ρ_f, μ_f, c_{pf} and k_f are the density, dynamic viscosity, specific heat capacity and thermal conductivity of the fluid, respectively. $\vec{u}_f$ is the fluid velocity. P is the fluid pressure. The continuity equation for impressible flow is:

$$\nabla \cdot \vec{u}_f = 0 \tag{6.5}$$

The flow properties (e.g. fluid density and viscosity) are assumed to be independent of fluid temperature. The particle Reynolds number is calculated based on the volume equivalent sphere diameter ($d_V = \left(\frac{6V_p}{\pi}\right)^{1/3}$, V_p is the volume of the particle) and the fluid superficial velocity ($\vec{u}_s$) which is defined as the fluid velocity averaged over the total volume of the domain:

$$Re_V = \frac{\rho_f \vec{u}_s d_V}{\mu_f} \tag{6.6}$$

The Prandtl number is given by:

$$Pr = \frac{c_{pf}\,\mu_f}{k_f} \tag{6.7}$$

The heat transfer coefficient can be calculated as:

$$h = \frac{\dot{q}}{S_p \Delta T} \tag{6.8}$$

$$\Delta T = \bar{T}_f - T_s \tag{6.9}$$

Where $\dot{q}$, $\bar{T}_f$ and T_s are the heat transfer rate, average temperature of surrounding fluid, and particle temperature, respectively. S_p is the surface area of the particle. In practice, the heat transfer coefficient h is always expressed in terms of Nusselt number:

$$Nu = \frac{hd_p}{k_f} \tag{6.10}$$

d_p is the characteristic length of the particle. In this work, the volume equivalent diameter (d_V) and Sauter diameter (d_s) are used as d_p, viz. $d_V = \left(\frac{6V_p}{\pi}\right)^{1/3}$ and $d_s = \Phi d_V$, Φ is the sphericity. In packed bed, the average Nusselt number is obtained by averaging individual particle Nusselt number. The Nusselt number of the i-th particle is calculated as follows:

$$Nu_i = \frac{\dot{q}_i d_p}{S_p(\bar{T}_f - T_s)k_f} \tag{6.11}$$

Based on the characteristic size of the particle, two different particle Nusselt number are defined:

$$Nu_{i,V} = \frac{\dot{q}_i d_V}{S_p\left(\bar{T}_f - T_s\right)k_f}$$

$$Nu_{i,s} = \frac{\dot{q}_i d_s}{S_p(\bar{T}_f - T_s)k_f} \tag{6.12}$$

In equation (6.11), $\dot{q}_i$ is the heat transfer rate between particle i and surrounding fluid,

$$\dot{q}_i = -\iint\limits_{S_{pi}} k_f \nabla T_f \cdot \vec{n} ds \tag{6.13}$$

$$\bar{T}_f = \frac{\iiint\limits_{V_b} u_{f,x}(x,y,z)T_f(x,y,z)dxdydz}{\iiint\limits_{V_b} u_{f,x}(x,y,z)dxdydz} \tag{6.14}$$

Where S_{pi} is the surface of i-th particle, V_b is a cubic box with centre coinciding with the particle centre. $\vec{n}$ is a unit vector in the normal direction of the particle surface. In this work, the size of the box is $3d_V$. The average Nusselt number of the packed bed is then obtained based on the characteristic size of the particle:

$$Nu_V = \frac{1}{N_p}\sum_{i=1}^{N_p} Nu_{i,V}$$

$$Nu_s = \frac{1}{N_p}\sum_{i=1}^{N_p} Nu_{i,s} \tag{6.15}$$

Except defining the Reynolds number based on the characteristic length of an individual particle, other definitions of Reynolds number are also proposed for developing the Nusselt number correlation for packed beds. Bird et al. (1960), Incropera & Dewitt (1990) and Nsofor & Adebiyi (2001) defined a characteristic length of packed bed, which is the ratio of the volume of the bed to the total surface of the particles:

$$d_b = \frac{V_p}{\phi S_p} \tag{6.16}$$

For the bed comprising equal size spherical particles, Eq. (6.16) is calculated as follows:

$$d_b = \frac{d_V}{6\phi} \tag{6.17}$$

Yang et al. (2010, 2012) defined the Reynolds number based on the hydraulic diameter of packed bed which can be calculated as follows:

$$d_h = \frac{4(1-\phi)V_p}{\phi S_p}$$ (6.18)

Therefore, the Reynolds number is

$$\mathrm{Re}_h = \frac{\rho_f u_s d_h}{\mu_f}$$ (6.19)

With this Reynolds number, Yang et al. (2010, 2012) correlated the experimental or simulation data and formulated Nusselt number correlations for packed beds.

6.4 Numerical Method

The thermal lattice Boltzmann method with immersed boundary conditions for momentum and temperature has been described and used in Chen et al. (Chapter 4). Here we provide a brief description of the method. The evolution equations for the density and energy distribution functions are modified to account for the interaction between solid and fluid phases:

$$f_i(\vec{x}+\vec{e}_i\Delta t, t+\Delta t) = f_i(\vec{x},t) - \frac{\Delta t}{\tau_v}(1-B_v)[f_i(\vec{x},t) - f_i^{eq}(\vec{x},t)] + B_v\Omega_{i,v}^p$$ (6.20)

$$g_i(\vec{x}+\vec{e}_i\Delta t, t+\Delta t) = g_i(\vec{x},t) - \frac{\Delta t}{\tau_c}(1-B_c)[g_i(\vec{x},t) - g_i^{eq}(\vec{x},t)] + B_c\Omega_{i,c}^p$$ (6.21)

Where f_i and g_i are the density and energy distribution functions at time t and position $\vec{x}$ with velocity $\vec{e}_i$. In this work, D3Q19 and D3Q7 models are used for density and energy evolution equations, respectively. τ_v and τ_c are relaxation times related to viscosity and thermal diffusivity, respectively. The superscript 'eq' denotes the equilibrium state. $\Omega_{i,v}^p$ and $\Omega_{i,c}^p$ are additional collision terms that bounce back the non-equilibrium parts of the density and energy distributions, respectively.

$$\Omega_{i,v}^p = f_{-i}(\vec{x},t) - f_i(\vec{x},t) + f_i^{eq}(\rho_f(\vec{x},t),\vec{u}_p(\vec{x},t)) - f_{-i}^{eq}(\rho_f(\vec{x},t),\vec{u}_f(\vec{x},t))$$ (6.22)

$$\Omega_{i,c}^p = -g_{-i}(\vec{x},t) - g_i(\vec{x},t) + g_i^{eq}(\varphi_s,\vec{u}_f(\vec{x},t)) + g_{-i}^{eq}(\varphi(\vec{x},t),\vec{u}_f(\vec{x},t))$$ (6.23)

110

u_p is the particle velocity at position $\vec{x}$. φ_s is the temperature of the particle. B_v and B_c are weighting functions, which can be calculated as follows:

$$B_v(\phi_x, \tau_v) = \frac{\phi_x(\frac{\tau_v}{\Delta t} - \frac{1}{2})}{(1-\phi_x)+(\frac{\tau_v}{\Delta t} - \frac{1}{2})} \tag{6.24}$$

$$B_c(\phi_x, \tau_c) = \frac{\phi_x(\frac{\tau_c}{\Delta t} - \frac{1}{2})}{(1-\phi_x)+(\frac{\tau_c}{\Delta t} - \frac{1}{2})} \tag{6.25}$$

Where ϕ_x is the volume fraction of a lattice that is covered by the solid particles. $B_c = 1$ and $B_v = 1$ are corresponding to pure fluid and solid nodes, respectively. The macroscopic properties for density, momentum and energy can be obtained through the following equations, respectively:

$$\rho_f = \sum_i f_i \tag{6.26}$$

$$\rho_f \vec{u}_f = \sum_i f_i \vec{e}_i \tag{6.27}$$

$$\varphi = \sum_i g_i \tag{6.28}$$

The viscosity and thermal diffusivity are computed via the following equations:

$$v = \frac{1}{3}c^2(\tau_v - \frac{\Delta t}{2}) \tag{6.29}$$

$$D = \frac{1}{4}c^2(\tau_c - \frac{\Delta t}{2}) \tag{6.30}$$

6.5 Simulations and Results

Prior to calculating the heat transfer coefficients for packed beds, a simple validation of the method for use with cubic particles was performed. The thermal lattice Boltzmann method with immersed boundary conditions has been comprehensively validated for isothermal (e.g. drag coefficients of sphere, cube and spheroids; drag force for assemblies of spheres) and non-isothermal (e.g. Nusselt number for a single sphere in uniform flows) flows (Chen et al., 2015; Chapter 3; Chapter 4; Chapter 5). Here we compare the Nusselt numbers of a single perfect cube in uniform flows with

the simulation results reported by Richter et al. (2012). Richter et al. (2012) used a commercial finite volume solver (ANSYS FLUENT) to calculate the Nu_V number for a single cube in a uniform flows. The domain size in current simulations was $240 \times 120 \times 120$ lattice units. At the inlet, uniform fluid velocity and constant temperature are applied. At the outlet, the normal derivative of the velocity and temperature was set to zero. Symmetry boundary conditions for velocity and temperature were assigned to the side domain boundaries. The length of the cube was 15 in lattice units. Figure 6.1 plots the Nusselt number obtained by LBM simulations and simulation results extracted from Richter et al. (2012). The comparison demonstrates that the lattice Boltzmann method can reproduce the results of standard simulations.

For packed bed simulations, $N_p = 54$ equal size super-quadric cubes were randomly distributed in a periodic, cubic domain using standard Monte Carlo method (Frenkel & Smit, 1996) (Figure 6.2). The cubes ($m = 5$) were represented using the super-quadric equation (Eq. (6.31)).

$$\left(\frac{x}{a}\right)^m + \left(\frac{y}{b}\right)^m + \left(\frac{z}{c}\right)^m = 1 \tag{6.31}$$

The volume equivalent diameter (d_V) of the super-quadric cubes used ranged from 22 to 41 in lattice units. The domain size was 150^3 for solid volume fractions 0.1, 0.2 and 0.3. Domain sizes of 155^3 and 160^3 were used for solid volume fraction 0.4 and 0.45, respectively. Fully periodic domain boundaries were employed for the velocity and temperature of the fluid. The particle Reynolds numbers (Re_V) were set to 1, 10, 25, 50 and 100, respectively. The Prandtl number was 0.7. For each given Re_V and solid volume fraction, 6 different packing configurations were modelled and the values obtained were averaged. The method used for assigning a steady state Nusselt number was proposed by Yang et al. (2011) who calculated the heat transfer for a sphere in simple shear flow. If the change of the Nusselt number in the last 20% computational time was less than 1%, the computation was assumed to have reached steady state. Figure 6.3 shows the Nu_V as a function of time (The volume equivalent diameter was taken as the characteristic size of the cube). The high Nu_V at the starting time is due to the large temperature gradient at the particle fluid interface when initiating the heat transfer. Figure 6.4 plots the Nusselt number ($Nu_{i,V}$) for individual super-quadric cubes along the streamwise direction at steady state conditions. It shows that the flow is thermally fully-developed since there is no statistically significant change in Nusselt number for individual particles along the flow direction. Due to the local flow

velocity and temperature gradient, the $Nu_{i,V}$ in a single cross section varies from particle-to-particle.
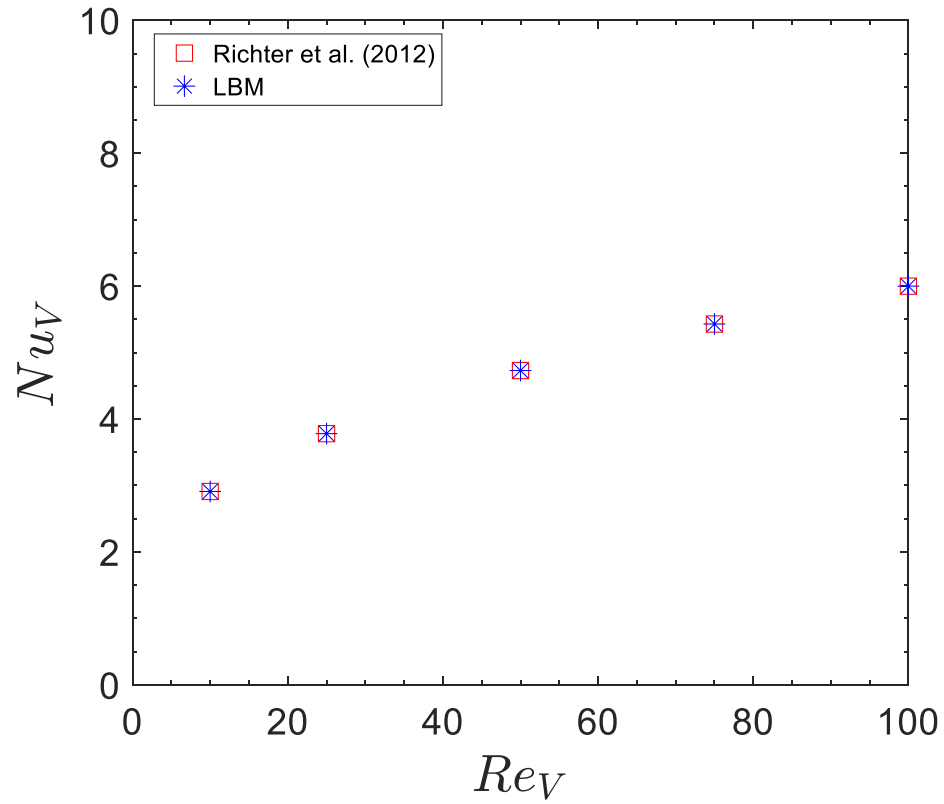

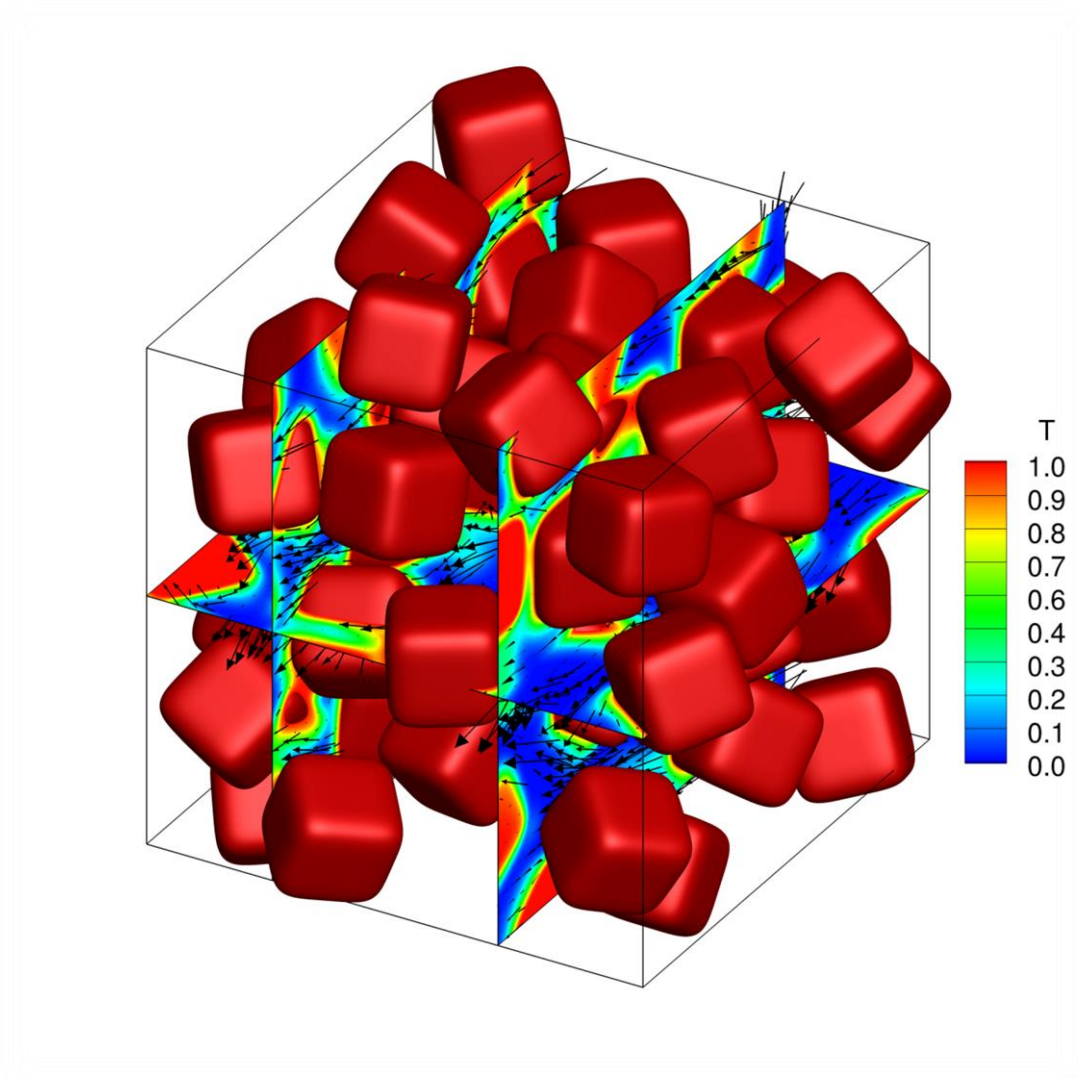Figure 6.1. Nusselt number as a function of Reynolds number for a single perfect cube in a uniform flow.

Figure 6.2. An example particle configuration in a periodic box. Temperature contours are shown in three planes for $Re_V = 50$ and $\phi = 0.4$. The Prandtl number is 0.7.
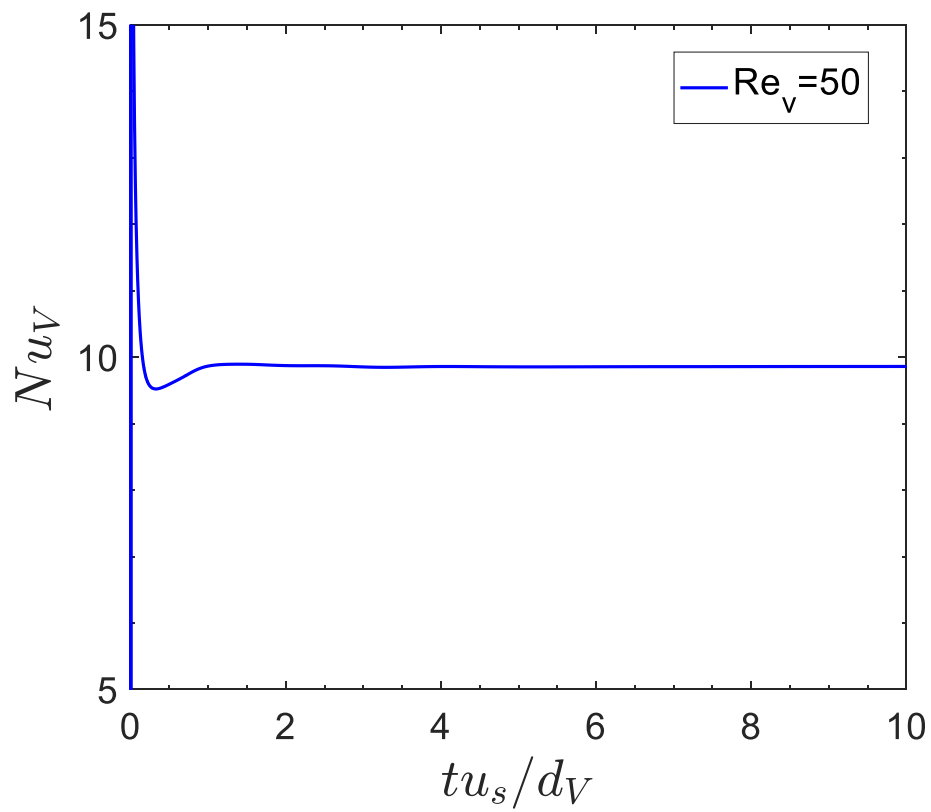
Figure 6.3. Average Nusselt number as a function of time for $\phi = 0.4$ for random assemblies of super-quadric cubes. The Prandtl number is 0.7.
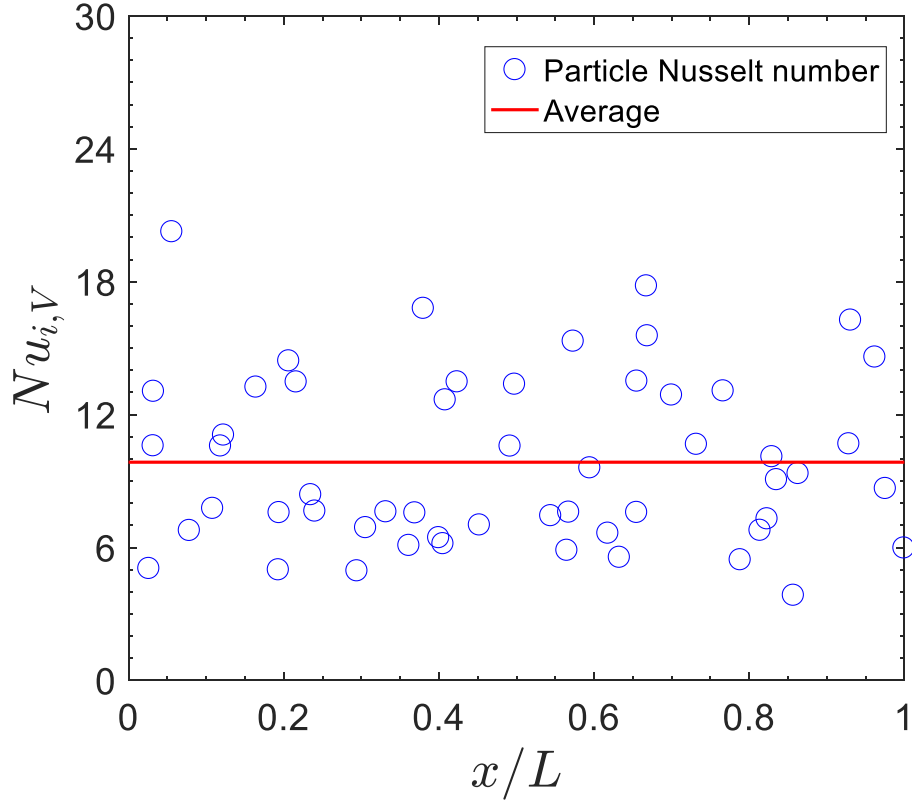
Figure 6.4. Nusselt number of individual particles along the streamwise direction for $Re_V = 50$ and $\phi = 0.4$ at $t u_s/d_V = 10$. The Prandtl number is 0.7.

Based on the simulation data, a Nusselt number correlation for assemblies of spheres was developed in Chapter 5:

$$Nu = 2 + 0.77\phi + 0.64\phi^2 + (0.6 + 1.1\phi) Re_V^{0.5} Pr^{1/3} \qquad (6.32)$$

Figure 6.5 plots the simulation results (the volume equivalent diameter was taken as the characteristic size of the cube) for assemblies of super-quadric cubes and the prediction of Eq. (6.32), respectively. At low solid volume fraction ($\phi < 0.3$), the prediction of Nusselt number by Eq. (6.32) agrees well with the simulation data. At high solid volume fraction, Eq. (6.32) significantly under predicts the Nusselt number for assemblies of super-quadric cubes. Therefore, the Eq. (6.32) cannot be applied to predict the particle to fluid heat transfer for assemblies of super-quadric cubes using volume equivalent diameter of the cube.

To characterize the shape of the super-quadric cube, the surface area equivalent diameter and sphericity are defined as follows:

$$d_N = \sqrt{\frac{S_p}{\pi}} \;;\;\; \Phi = \frac{d_V^2}{d_N^2}$$

(6.33)

Inserting Eq. (6.33) into Eq. (6.18), the hydraulic diameter of the packing comprising equal size super-quadric cubes is as follows:

$$d_h = \frac{2(1-\phi)d_V\Phi}{3\phi}$$

(6.34)

According to Eq. (6.19), the Re_h (based on the hydraulic diameter) is calculated as follows:

$$\mathrm{Re}_h = \frac{\rho_f u_s d_V}{\mu_f} \cdot \frac{2(1-\phi)\Phi}{3\phi}$$

(6.35)

Inserting Eq. (6.6) into Eq. (6.35), we obtain

$$\mathrm{Re}_h = \frac{2(1-\phi)}{3\phi}\Phi\,\mathrm{Re}_V$$

(6.36)

Inserting Eq. (6.36) into Eq. (6.32), we find

$$Nu = 2 + 0.77\phi + 0.64\phi^2 + (0.6+1.1\phi)\,\mathrm{Re}_h^{0.5}\,\mathrm{Pr}^{1/3}(\frac{3\phi}{2(1-\phi)\Phi})^{0.5}$$

(6.37)

Figure 6.6 plots the simulation data (Nu_V) for assemblies of super-quadric cubes as a function of Re_h and the predictions by Eq. (6.37), respectively. The Reynolds numbers (Re_V) for the simulation data are transformed to Re_h according to Eq. (6.36). The simulation data agree well with Eq. (6.37) for low solid volume fractions ($\phi \le 0.3$). At high solid volume fraction, Eq. (6.37) slightly under predicts the Nu_V for assemblies of super-quadric cubes. Finally, the Sauter diameter (d_s) is used to characterize the particle to fluid heat transfer in random assemblies of super-quadric cubes. As a result, the Nusselt numbers (Nu_V) obtained from the simulations (based on the volume equivalent diameter) were transformed to the values for Sauter diameter (Nu_s, viz. $Nu_s = \Phi Nu_V$). The simulation data (Nu_s) and the predictions of Nusselt number by Eq. (6.37) are shown in Figure 6.7. The comparison demonstrates that Eq. (6.37) can accurately estimate the particle to fluid heat transfer for assemblies

of super-quadric cubes if the Sauter diameter was used to characterize the particle to fluid heat transfer in the assembly.
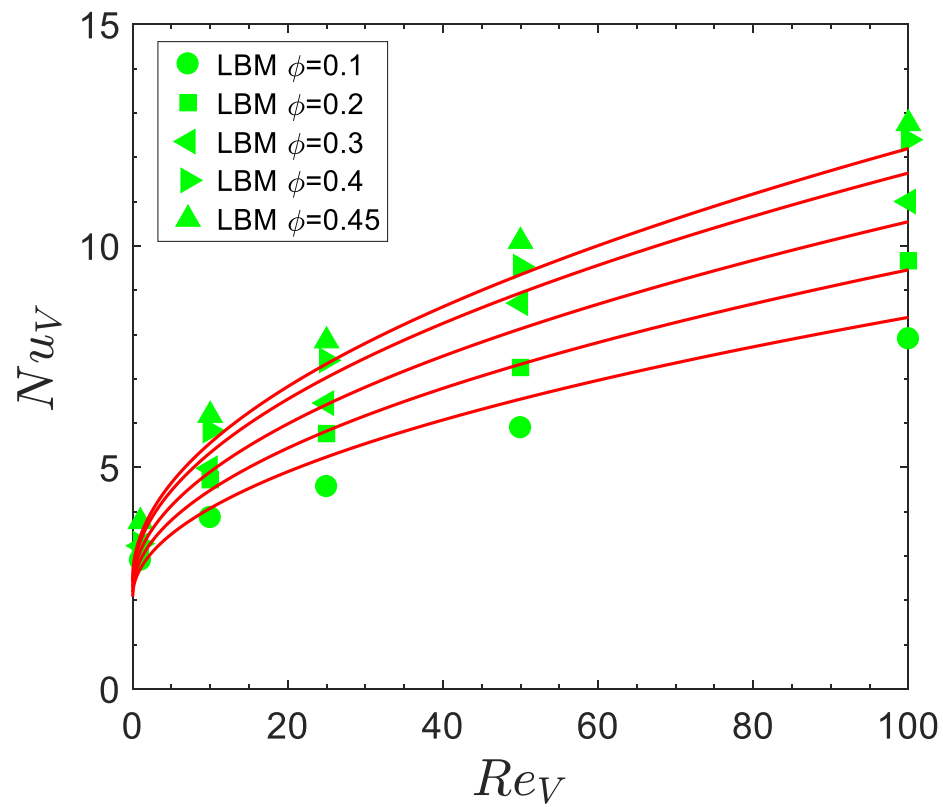

Figure 6.5. Nusselt numbers as a function of Re_V for assemblies of super-quadric cubes. The lines plot Eq. (6.32). The Prandtl number is 0.7.
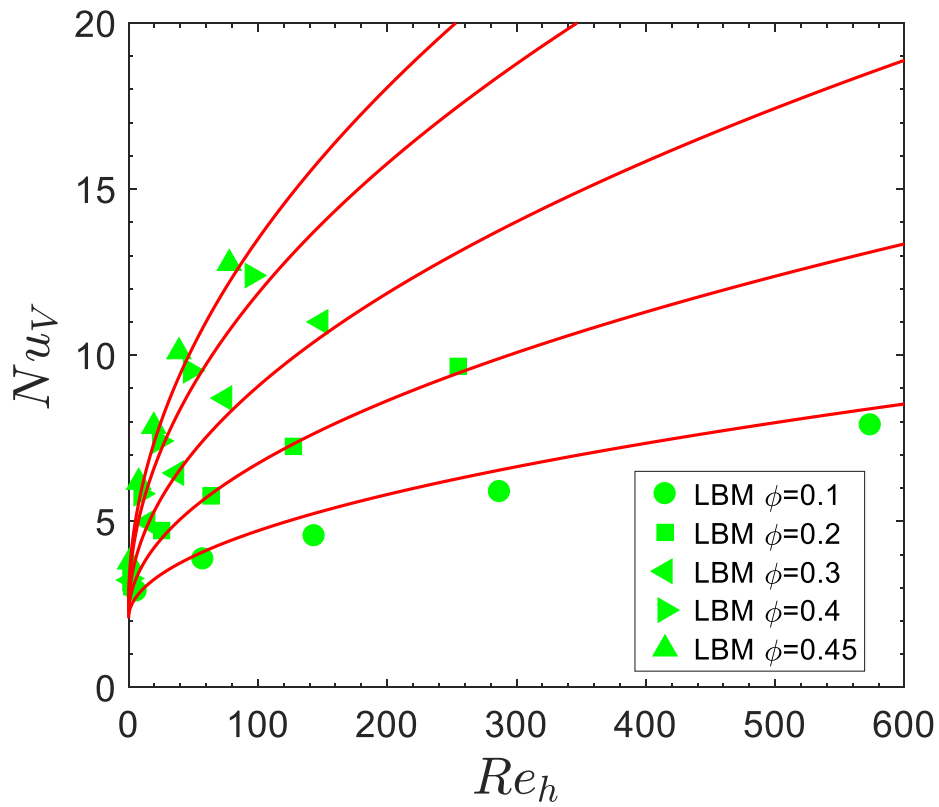
Figure 6.6. Nusselt numbers based on volume equivalent diameter for assemblies of super-quadric cubes as a function of Re_h. The lines plot Eq. (6.37). The Prandtl number is 0.7.
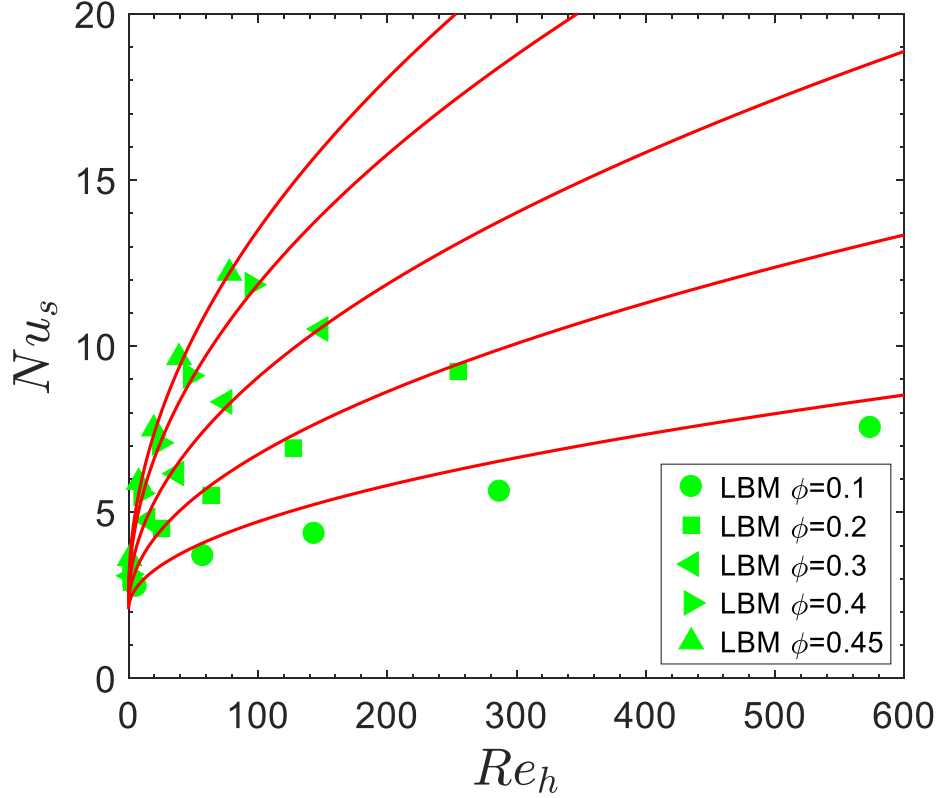
Figure 6.7. Nusselt number based on the Sauter diameter for assemblies of super-quadric cubes as a function of Re_h. The lines plot Eq. (6.37). The Prandtl number is 0.7.

6.6 Conclusions

In this work, the thermal lattice Boltzmann method with immersed moving boundary conditions was used to compute the average Nusselt number acting on assemblies of super-quadric cubes for a wide range of solid volume fraction for $Re_V \leq 100$ in cubic, periodic domains. The comparison between the simulation data for assemblies of super-quadric cubes and the predictions by Nusselt number correlation for assemblies of spheres (Chapter 5) indicates that only substituting volume equivalent diameter (d_V) is not sufficient to characterize heat transfer for cubic particles using Nusselt number correlations for assemblies of spheres if the Reynolds number was defined based on the volume equivalent diameter of the cube. Defining the Reynolds number based on the hydraulic diameter of the packing (Re_h), the Nusselt number correlation proposed for assemblies of spheres (Chapter 5) was transformed into a form that is a function of Re_h. The new Nusselt number correlation can be applied to

predict the heat transfer of cubic particles in an assembly if the Sauter diameter was chosen as the characteristic size of the cube.

7 Conclusions and Outlook

7.1 Conclusions

Particulate two phase, non-isothermal flows are encountered widely in industrial applications. Understanding the complicated interaction between fluid mechanics and thermal effects are essential to improve the design of reactors that are commonly applied in the chemical industry and hence their efficiency. Due to the lack of drag force and Nusselt number correlations for assemblies of non-spherical particles, the simulations of gas-fluidized beds are restricted to beds containing spherical particles. In practical applications, the particles in gas-fluidized beds are, however, often non-spherical. Therefore, developing momentum exchange and heat transfer correlations for gas-solid flows comprising non-spherical particles based on the direct numerical simulation of such systems is critical to predict accurately and hence improve the design of such systems.

In this work, drag force and Nusselt number correlations for assemblies of cubes were developed. The cubes were represented by two different methdods: (1) Construction from several, identical spheres, that are unbreakable and undeformable; (2) Representation by a continuous function, i.e. the super-quadric equation.

In chapter 2, the drag force acting on assemblies of approximately cubic particles that were constructed from eight identical spheres was calculated using a lattice Boltzmann method for $Re \leq 200$ and $\phi \leq 0.45$. The simulation data were compared with predictions that have been derived numerically (Beetstra et al., 2001). The comparison indicates that Beetstra's correlation under-predicts the drag force acting on assemblies of approximately cubic particles in particular for high solid volume fractions and Reynolds numbers. Subsequently, the method was extended to compute the drag force acting on assemblies of super-quadric cubes (Chapter 3). The simulation data were compared with the predictions of Ergun-based correlations, Hilton et al. (2010), Tang et al. (2015) and Chen et al. (2015). It was found that the Ergun-based correlations and the correlation for assemblies of approximately cubic particles cannot predict the drag force for assemblies of super-quadric cubes. The correlation proposed by Hilton et al. (2010) significantly under-predicted the drag force for super-quadric cubes, although the correlation has been employed previously to simulate gas-fluidized beds comprising cubic particles (Hilton et al., 2010, 2011; Oschmann et al., 2014). In addition, the comparison with Tang' correlation demonstrated that only for relatively small Reynolds numbers ($Re \leq 10$) super-quadric cubes can be approximated by volume equivalent spheres. At higher Reynolds numbers, this approximation would induce a large error (up to 56%) in estimating the gas-solid interaction and lead, in turn, to large errors in modelling the dynamics of e.g. gas-solid fluidized bed. Hence, based on the simulation data, we proposed a new drag force correlation for assemblies of super-quadric cube.

Secondly, Nusselt number correlations for assemblies of spheres and super-quadric cubes were developed. To this end, we propose a new Dirichlet boundary condition for thermal lattice Boltzmann methods (Chapter 4). The thermal boundary condition was second order accurate and suitable for boundary-dominated problems, e.g. porous medium. The thermal lattice Boltzmann method was used to calculate the Nusselt number for assemblies of spheres. The simulation data were compared with experimentally and numerically derived correlations. The experimentally derived correlations (Gunn, 1978; Wakao et al., 1979) significantly over-predicted the Nusselt number for assemblies of spheres since these correlations are valid for a wide range of Reynolds numbers (10^4-10^5). The numerically derived correlations have inherent shortcomings since the data used to correlate the correlations were affected by the domain boundary conditions applied (Chapter 5). The comparison with Tavassoli et al. (2015) showed that the agreement was good if the data were obtained from the simulations of thermally fully-developed flows. Otherwise, a large difference between the LBM data and Tavassoli et al. (2015) was observed. In Sun's simulations (Sun et al., 2015), the heat transfer in a statistically homogenous, gas-solid flow was assumed to be analogous to a single phase thermally fully-developed flow in pipes with isothermal walls. However, the results of Sun et al. (2015) showed some difference to the data of Tavassoli et al. (2015) and the LBM. Hence, based on the LBM data, a new Nusselt number correlation was proposed for assemblies of spheres for Re ≤ 100 and φ ≤ 0.5 which is expected to be more accurate than previous numerically derived correlations. Finally, the LBM method was extended to simulate the heat transfer for assemblies of super-quadric cubes. By defining the Reynolds number based on the hydraulic diameter of the packing (Re_h), the Nusselt number correlation proposed for assemblies of sphere (Chapter 5) was transformed to a modifed form that is a function of Re_h. The new Nusselt number correlation can be applied to predict the Nusselt number for assemblies of super-quadric cubes if the Sauter diameter is chosen as the characteristic size of the particle. We expect that the new correlations proposed in this thesis can improve the accuracy of Euler-Euler and Euler-Lagrangian simulations of gas-solid non-isothermal flows in packed and fluidized beds comprising cubic particles.

7.2   Future work

7.2.1   Effect of particle orientation on the drag force

In this work, we have developed a drag force correlation for assemblies of super-quadric cubes. The effect of solid volume fraction on the drag force was taken into account. However, it is well-known that the orientation of a cube with respect to the flow direction has also a significant effect on the drag force which is not considered in Eq. (3.28). In future, DNS simulations of cubic particles with preferential orientations with respect to the flow direction (e.g. 0, $\frac{\pi}{4}$) shall be

performed. This will be a first step to investigate the influence of particle orientation on the drag force. Hölzer and Sommerfeld (2008) proposed a correlation for the drag coefficient of single, non-spherical particles as a function of crosswise sphericity ($\Phi_\perp$), sphericity (Φ) and Reynolds number. To apply this correlation to the modelling of gas-fluidized beds containing cubic particles, a "correction" for the effect of solid volume fraction on the drag force has to be developed. Based on Eq. (3.13) (Hilton et al., 2010), DNS simulations of assemblies of cubic particles can be used to propose a term to incorporate the voidage dependence in Eq. (3.13).

7.2.2   Wet granular flows

Wet particles behave completely different to dry particles. The collision between wet particles is complicated due to the presence of a liquid film/layer of varying thickness. During particle motion and/or collision a film can form, deform or rupture. A fundamental understanding of the contact mechanics of collisions in "wet" particle systems will be essential to model wet granular flows. Several experimental studies concerning the interaction between wetted particles have been reported, however, in these works typically the particles are immersed in a liquid to mimic wet particle collisions. On the other hand, DNS approaches may provide the required insight to formulate simplified, yet appropriate, collision models for such systems. Jain et al. (2012) simulated the collision between a particle and a liquid film using an immersed boundary method (IBM) in a volume of fluid (VOF) framework. The simulation results agreed well with the experimental data obtained by Antonyuk et al. (2009). In the future, a combined lattice Boltzmann method-volume of fluid approach may be used to model the liquid between interacting particles. To model the liquid spreading on the particle surface, a contact angle boundary condition (Brackbill et al., 1992, Patel et al., 2017) is required at the contact lines (gas-solid-liquid interface). Subsequently, the DNS simulations can be used to propose improved models to determine the effective (wet) restitution coefficient.

References

Aidun, C. K., Lu, Y., Ding, E. J. (1998). Direct analysis of particulate suspensions with inertia using the discrete Boltzmann equation. Journal of Fluid Mechanics, 373, 287-311.

Alexander, F. J., Chen, S., Sterling, J. D. (1993). Lattice Boltzmann thermohydrodynamics. Physical Review E, 47(4), R2249.

Antonyuk, S., Heinrich, S., Deen, N., Kuipers, H. (2009). Influence of liquid layers on energy absorption during particle impact. Particuology, 7(4), 245-259.

Batchelor, G.K. (1967). An Introduction to Fluid Dynamics. Cambridge University Press. ISBN 0-521-66396-2.

Beetstra, R., Van der Hoef, M. A., Kuipers, J. A. M. (2006). A lattice-Boltzmann simulation study of the drag coefficient of clusters of spheres. Computers & fluids, 35(8), 966-970.

Beetstra, R., Van der Hoef, M. A., Kuipers, J. A. M. (2007). Drag force of intermediate Reynolds number flow past mono- and bi-disperse arrays of spheres. AIChE Journal, 53(2), 489-501.

Bartoloni, A., Battista, C., Cabasino, S., Paolucci, P. S., Pech, J., Sarno, R., Benzi, R. (1993). LBE simulations of Rayleigh-Bénard convection on the APE100 parallel processor. International Journal of Modern Physics C, 4(05), 993-1006.

Brady, J. F., Bossis, G. (1988). Stokesian dynamics. Annual review of fluid mechanics, 20, 111-157.

Bokkers, G. A., van Sint Annaland, M., Kuipers, J. A. M. (2004). Mixing and segregation in a bidisperse gas-solid fluidised bed: a numerical and experimental study. Powder Technology, 140(3), 176-186.

Bird, R. B., Stewart, W. E., Lightfoot, E. N. (2007). Transport phenomena, 2nd edition London: John Wiley and Sons.

Balachandar, S., Ha, M. Y. (2001). Unsteady heat transfer from a sphere in a uniform cross-flow. Physics of Fluids, 13(12), 3714-3728.

Brackbill, J. U., Kothe, D. B., Zemach, C. (1992). A continuum method for modeling surface tension. Journal of computational physics, 100(2), 335-354.

Carman, P. C. (1937). Fluid flow through granular beds. Transactions-Institution of Chemical Engineeres, 15, 150-166.

Clift, R., Grace, J. R., Weber, M. E. (1978). Bubbles, Drops and Particles, Academic Press, New York.

Chen, Y., Third, J. R., Müller, C. R. (2015). A drag force correlation for approximately cubic particles constructed from identical spheres. Chemical Engineering Science, 123, 146-154.

Chen, S., Doolen, G. D. (1998). Lattice Boltzmann method for fluid flows. Annual review of fluid mechanics, 30(1), 329-364.

Crowe, C. T. (ED.), (2010). Multiphase flow handbook. Taylor & Francis, London.

Di Felice, R. (1995). Hydrodynamics of liquid fluidisation. Chemical Engineering Science, 50(8), 1213-1245.

Dash, S. M., Lee, T. S., Huang, H. (2014). Natural convection from an eccentric square cylinder using a novel flexible forcing IB-LBM method. Numerical Heat Transfer, Part A: Applications, 65(6), 531-555.

Dan, C., Wachs, A. (2010). Direct numerical simulation of particulate flow with heat transfer. International Journal of Heat and Fluid Flow, 31(6), 1050-1057.

Ergun, S. (1952). Fluid flow through packed columns. Chemical Engineering Progress, 48, 89-94.

Frenkel, D., Smit, B. (1996). Understanding molecular simulation: From algorithms to applications. San Diego: Academic.

Fand, R. M., Kim, B. Y. K., Lam, A. C. C., Phan, R. T. (1987). Resistance to the flow of fluids through simple and complex porous media whose matrices are composed of randomly packed spheres. Journal of Fluids Engineering, 109(3), 268-274.

Freund, H., Zeiser, T., Huber, F., Klemm, E., Brenner, G., Durst, F., Emig, G. (2003). Numerical simulations of single phase reacting flows in randomly packed fixed-bed reactors and experimental validation. Chemical Engineering Science, 58(3), 903-910.

Froessling, N. (1938). Über die verdunstung fallender tropfen. Gerlands Beiträge zur Geophysik, 52, 170-215.

Feng, Z. G., Michaelides, E. E. (2004). The immersed boundary-lattice Boltzmann method for solving fluid–particles interaction problems. Journal of Computational Physics, 195(2), 602-628.

Feng, Z. G., Michaelides, E. E. (2008). Inclusion of heat transfer computations for particle laden flows. Physics of Fluids, 20(4), 040604.

Feng, Z. G., Musong, S. G. (2014). Direct numerical simulation of heat and mass transfer of spheres in a fluidized bed. Powder Technology, 262, 62-70.

Ganser, G. H. (1993). A rational approach to drag prediction of spherical and non-spherical particles. Powder Technology, 77(2), 143-152.

Guo, Z., Shi, B., Zheng, C. (2002). A coupled lattice BGK model for the Boussinesq equations. International Journal for Numerical Methods in Fluids, 39(4), 325-342.

Ginzburg, I. (2005). Generic boundary conditions for lattice Boltzmann models and their application to advection and anisotropic dispersion equations. Advances in Water Resources, 28(11), 1196-1216.

Gunn, D. J. (1978). Transfer of heat or mass to particles in fixed and fluidised beds. International Journal of Heat and Mass Transfer, 21(4), 467-476.

Guardo, A., Coussirat, M., Recasens, F., Larrayoz, M. A., Escaler, X. (2006). CFD study on particle-to-fluid heat transfer in fixed bed reactors: Convective heat transfer at low and high pressure. Chemical Engineering Science, 61(13), 4341-4353.

Hinch, E. J. (1977). An averaged-equation approach to particle interactions in a fluid suspension. Journal of Fluid Mechanics, 83(04), 695-720.

Hill, R. J., Koch, D. L., Ladd, A. J. C. (2001a). The first effects of fluid inertia on flows in ordered and random arrays of spheres. Journal of Fluid Mechanics, 448(2), 213-241.

Hill, R. J., Koch, D. L., Ladd, A. J. C. (2001b). Moderate-Reynolds-number flows in ordered and random arrays of spheres. Journal of Fluid Mechanics, 448(2), 243-278.

Hölzer, A., Sommerfeld, M. (2008). New simple correlation formula for the drag coefficient of non-spherical particles. Powder Technology, 184(3), 361-365.

He, X., Luo, L. S. (1997). A priori derivation of the lattice Boltzmann equation. Physical Review E, 55(6), 6333-6336.

Hasimoto, H. (1959). On the periodic fundamental solutions of the Stokes equations and their application to viscous flow past a cubic array of spheres. Journal of Fluid Mechanics, 5(02), 317-328.

Holland, D. J., Müller, C. R., Dennis, J. S., Gladden, L. F., Sederman, A. J. (2008). Spatially resolved measurement of anisotropic granular temperature in gas-fluidized beds. Powder Technology, 182(2), 171-181.

Hilton, J. E., Mason, L. R., Cleary, P. W. (2010). Dynamics of gas-solid fluidised beds with non-spherical particle geometry. Chemical Engineering Science, 65(5), 1584-1596.

Hilton, J. E., Cleary, P. W. (2011). The influence of particle shape on flow modes in pneumatic conveying. Chemical Engineering Science, 66(3), 231-240.

He, X., Chen, S., Doolen, G. D. (1998). A novel thermal model for the lattice Boltzmann method in incompressible limit. Journal of Computational Physics, 146(1), 282-300.

Incropera, F.P., DeWitt, D.P. (1990). Introduction to Heat Transfer (second ed.), Wiley, New York.

Jain, D., Deen, N. G., Kuipers, J. A. M., Antonyuk, S., Heinrich, S. (2012). Direct numerical simulation of particle impact on thin liquid films using a combined volume

of fluid and immersed boundary method. Chemical engineering science, 69(1), 530-540.

Koch, D. L., Sangani, A. S. (1999). Particle pressure and marginal stability limits for a homogeneous monodisperse gas-fluidized bed: kinetic theory and numerical simulations. Journal of Fluid Mechanics, 400(1), 229-263.

Kim, S., Russel, W. B. (1985). Modelling of porous media by renormalization of the Stokes equations. Journal of Fluid Mechanics, 154, 269-286.

Kriebitzsch, S. H. L., Hoef, M. A., Kuipers, J. A. M. (2013). Drag force in discrete particle models? Continuum scale or single particle scale? AIChE Journal, 59(1), 316-324.

Ladd, A. J. C. (1994a). Numerical simulations of particulate suspensions via a discretized Boltzmann equation. Part 1. Theoretical foundation. Journal of Fluid Mechanics, 271, 285-309.

Ladd, A. J. C. (1994b). Numerical simulations of particulate suspensions via a discretized Boltzmann equation. Part 2. Numerical results. Journal of Fluid Mechanics, 271(1), 311-339.

Leith, D. (1987). Drag on non-spherical objects. Aerosol science and technology, 6(2), 153-161.

Lebon, L., Oger, L., Leblond, J., Hulin, J. P., Martys, N. S., Schwartz, L. M. (1996). Pulsed gradient NMR measurements and numerical simulation of flow velocity distribution in sphere packings. Physics of Fluids, 8(2), 293-301.

Li, J., Kuipers, J. A. M. (2003). Gas-particle interactions in dense gas-fluidized beds. Chemical Engineering Science, 58(3), 711-718.

Liang, S. C., Hong, T., Fan, L. S. (1996). Effects of particle arrangements on the drag force of a particle in the intermediate flow regime. International journal of multiphase flow, 22(2), 285-306.

Li, L., Ma, W. (2011). Experimental study on the effective particle diameter of a packed bed with non-spherical particles. Transport in porous media, 89(1), 35-48.

Liu, S., Afacan, A., Masliyah, J. (1994). Steady incompressible laminar flow in porous media. Chemical engineering science, 49(21), 3565-3586.

Liu, L. F., Zhang, Z. P., Yu, A. B. (1999). Dynamic simulation of the centripetal packing of mono-sized spheres. Physica A: Statistical Mechanics and its Applications, 268(3), 433-453.

Lu, G., Third, J. R., Müller, C. R. (2012). Critical assessment of two approaches for evaluating contacts between super-quadric shaped particles in DEM simulations. Chemical Engineering Science, 78, 226-235.

Lu, G., Third, J. R., Müller, C. R. (2014). Effect of wall rougheners on cross-sectional flow characteristics for non-spherical particles in a horizontal rotating cylinder. Particuology, 12, 44-53.

Lu, G., Third, J.R., Müller, C.R., 2015. Discrete element models for non-spherical particle systems: From theoretical developments to applications. Chemical Engineering Science, 127, 425-465.

Lu, G., Third, J. R., Müller, C. R. (2017). The parameters governing the coefficient of dispersion of cubes in rotating cylinders. Granular Matter, 19(1), 12.

Li, L., Mei, R., Klausner, J. F. (2013). Boundary conditions for thermal lattice Boltzmann equation method. Journal of Computational Physics, 237, 366-395.

Müller, C. R., Holland, D. J., Sederman, A. J., Scott, S. A., Dennis, J. S., Gladden, L. F. (2008). Granular temperature: comparison of magnetic resonance measurements with discrete element model simulations. Powder Technology, 184(2), 241-253.

Müller, C. R., Scott, S. A., Holland, D. J., Clarke, B. C., Sederman, A. J., Dennis, J. S., Gladden, L. F. (2009). Validation of a discrete element model using magnetic resonance measurements. Particuology, 7(4), 297-306.

Müller, C. R., Davidson, J. F., Dennis, J. S., Fennell, P. S., Gladden, L. F., Hayhurst, A. N., Sederman, A. J. (2006). Real-time measurement of bubbling phenomena in a three-dimensional gas-fluidized bed using ultrafast magnetic resonance imaging. Physical review letters, 96(15), 154504.

Müller, C. R., Holland, D. J., Third, J. R., Sederman, A. J., Dennis, J. S., Gladden, L. F. (2011). Multi-scale magnetic resonance measurements and validation of Discrete Element Model simulations. Particuology, 9(4), 330-341.

McNamara, G. R., Garcia, A. L., Alder, B. J. (1995). Stabilization of thermal lattice Boltzmann models. Journal of Statistical Physics, 81(1), 395-408.

Noble, D. R., Torczynski, J. R. (1998). A lattice-Boltzmann method for partially

saturated computational cells. International Journal of Modern Physics C, 9(08), 1189-1201.

Nemec, D., Levec, J. (2005). Flow through packed bed reactors: 1. Single-phase flow. Chemical Engineering Science, 60(24), 6947-6957.

Deen, N. G., Kriebitzsch, S. H., van der Hoef, M. A., Kuipers, J. A. M. (2012). Direct numerical simulation of flow and heat transfer in dense fluid–particle systems. Chemical Engineering Science, 81, 329-344.

Deen, N. G., Peters, E. A. J. F., Padding, J. T., Kuipers, J. A. M. (2014). Review of direct numerical simulation of fluid–particle mass, momentum and heat transfer in dense gas–solid flows. Chemical Engineering Science, 116, 710-724.

Nsofor, E. C., Adebiyi, G. A. (2001). Measurements of the gas-particle convective heat transfer coefficient in a packed bed for high-temperature energy storage. Experimental Thermal and Fluid Science, 24(1), 1-9.

Pettyjohn, E. S., Christiansen, E. B. (1948). Effect of particle shape on free settling rates of isometric particles. Chemical Engineering Progress, 44, 157-172.

Pareschi, G., Frapolli, N., Chikatamarla, S. S., Karlin, I. V. (2016). Conjugate heat transfer with the entropic lattice Boltzmann method. Physical Review E, 94(1), 013305.

Peng, Y., Shu, C., Chew, Y. T. (2003). Simplified thermal lattice Boltzmann model for incompressible thermal flows. Physical Review E, 68(2), 026701.

Patel, H. V., Das, S., Kuipers, J. A. M., Padding, J. T., Peters, E. A. J. F. (2017). A coupled Volume of Fluid and Immersed Boundary Method for simulating 3D multiphase flows with contact line dynamics in complex geometries. Chemical Engineering Science, 166, 28-41.

Ren, B., Zhong, W., Jin, B., Lu, Y., Chen, X., Xiao, R. (2011). Study on the drag of a cylinder-shaped particle in steady upward gas flow. Industrial & Engineering Chemistry Research, 50(12), 7593-7600.

Ren, B., Zhong, W., Jiang, X., Jin, B., Yuan, Z. (2014). Numerical simulation of spouting of cylindroid particles in a spouted bed. The Canadian Journal of Chemical Engineering, 92(5), 928-934.

Rong, L. W., Dong, K. J., Yu, A. B. (2013). Lattice-Boltzmann simulation of fluid flow through packed beds of uniform spheres: Effect of porosity. Chemical Engineering Science, 99, 44-58.

Richter, A., Nikrityuk, P. A. (2012). Drag forces and heat transfer coefficients for spherical, cuboidal and ellipsoidal particles in cross flow at sub-critical Reynolds numbers. International Journal of Heat and Mass Transfer, 55(4), 1343-1354.

Ramachandran, R. S., Kleinstreuer, C., Wang, T. Y. (1989). Forced convection heat transfer of interacting spheres. Numerical heat transfer, 15(4), 471-487.

Romkes, S. J. P., Dautzenberg, F. M., Van den Bleek, C. M., Calis, H. P. A. (2003). CFD modelling and experimental validation of particle-to-fluid mass and heat transfer in a packed bed at very low channel to particle diameter ratio. Chemical Engineering Journal, 96(1), 3-13.

Succi, S. (2001). The lattice Boltzmann equation: for fluid dynamics and beyond. Oxford university press.

Shan, X. (1997). Simulation of Rayleigh-Bénard convection using a lattice Boltzmann method. Physical Review E, 55(3), 2780.

Shao, X., Shi, Y., Yu, Z. (2012). Combination of the fictitious domain method and the sharp interface method for direct numerical simulation of particulate flows with heat transfer. International Journal of Heat and Mass Transfer, 55(23), 6775-6785.

Sun, B., Tenneti, S., Subramaniam, S. (2015). Modeling average gas–solid heat transfer using particle-resolved direct numerical simulation. International Journal of Heat and Mass Transfer, 86, 898-913.

Shen, J., Kaguei, S., Wakao, N. (1981). Measurements of particle-to-gas heat transfer coefficients from one-shot thermal responses in packed beds. Chemical Engineering Science, 36(8), 1283-1286.

Scott, S. A., Davidson, J. F., Dennis, J. S., Hayhurst, A. N. (2004). Heat transfer to a single sphere immersed in beds of particles supplied by gas at rates above and below minimum fluidization. Industrial & engineering chemistry research, 43(18), 5632-5644.

Tran-Cong, S., Gay, M., Michaelides, E. E. (2004). Drag coefficients of irregularly shaped particles. Powder Technology, 139(1), 21-32.

Torobin, L. B., Gauvin, W. H. (1960). Fundamental aspects of solids-gas flow: Part IV: The effects of particle rotation, roughness and shape. Canadian Journal of Chemical Engineering, 38(5), 142-153.

Tenneti, S., Garg, R., Subramaniam, S. (2011). Drag law for monodisperse gas-solid systems using particle-resolved direct numerical simulation of flow past fixed assemblies of spheres. International journal of multiphase flow, 37(9), 1072-1092.

Tenneti, S., Sun, B., Garg, R., Subramaniam, S. (2013). Role of fluid heating in dense gas–solid flow as revealed by particle-resolved direct numerical simulation. International Journal of Heat and Mass Transfer, 58(1), 471-479.

Tang, Y., Kriebitzsch, S. H. L., Peters, E. A. J. F., van der Hoef, M. A., Kuipers, J. A. M. (2014). A methodology for highly accurate results of direct numerical simulations: drag force in dense gas–solid flows at intermediate Reynolds number. International journal of multiphase flow, 62, 73-86.

Tang, Y., Peters, E. A. J. F., Kuipers, J. A. M., Kriebitzsch, S. H. L., van der Hoef, M. A. (2015). A new drag correlation from fully resolved simulations of flow past monodisperse static arrays of spheres. AIChE Journal, 61(2), 688-698.

Tang, Y., Peters, E. A. J. F., Kuipers, J. A. M. (2016). Direct numerical simulations of dynamic gas-solid suspensions. AIChE Journal, 62(6), 1958-1969.

Tavassoli, H., Kriebitzsch, S. H. L., van der Hoef, M. A., Peters, E. A. J. F., Kuipers, J. A. M. (2013). Direct numerical simulation of particulate flow with heat transfer. International Journal of Multiphase Flow, 57, 29-37.

Tavassoli, H., Peters, E. A. J. F., Kuipers, J. A. M. (2015). Direct numerical simulation of fluid–particle heat transfer in fixed random arrays of non-spherical particles. Chemical Engineering Science, 129, 42-48.

Tavassoli, H., 2014. Direct numerical simulation of dense gas-solids non-isothermal flows (PhD thesis). Eindhoven University of Technology.

Ten Cate, A., Nieuwstad, C. H., Derksen, J. J., Van den Akker, H. E. A. (2002). Particle imaging velocimetry experiments and lattice-Boltzmann simulations on a single sphere settling under gravity. Physics of Fluids, 14(11), 4012-4025.

Van der Hoef, M. A., Beetstra, R., Kuipers, J. A. M. (2005). Lattice-Boltzmann simulations of low-Reynolds-number flow past mono-and bi-disperse arrays of spheres: results for the permeability and drag force. Journal of Fluid Mechanics, 528, 233-254.

Van der Hoef, M. A., van Sint Annaland, M., Deen, N. G., Kuipers, J. A. M. (2008). Numerical simulation of dense gas-solid fluidized beds: a multiscale modeling strategy. Annual Review Fluid Mechanics, 40, 47-70.

Wen, C. Y., Yu, Y. H. (1966). Mechanics of fluidization. Chemical Engineering Progress Series, 62, 100-111.

Wadell, H. (1933). Sphericity and roundness of rock particles. Journal of Geology, 41(3), 310-331.

Wang, L., Mi, J., Guo, Z. (2016). A modified lattice Bhatnagar–Gross–Krook model for convection heat transfer in porous media. International Journal of Heat and Mass Transfer, 94, 269-291.

Wakao, N., Kaguei, S., Funazkri, T. (1979). Effect of fluid dispersion coefficients on particle-to-fluid heat transfer coefficients in packed beds: correlation of Nusselt numbers. Chemical engineering science, 34(3), 325-336.

Whitaker, S. (1972). Forced convection heat transfer correlations for flow in pipes, past flat plates, single cylinders, single spheres, and for flow in packed beds and tube bundles. AIChE Journal, 18(2), 361-371.

Yoshida, H., Nagaoka, M. (2010). Multiple-relaxation-time lattice Boltzmann model for the convection and anisotropic diffusion equation. Journal of Computational Physics, 229(20), 7774-7795.

Yang, J., Wang, Q., Zeng, M., Nakayama, A. (2010). Computational study of forced convective heat transfer in structured packed beds with spherical or ellipsoidal particles. Chemical Engineering Science, 65(2), 726-738.

Yang, C., Zhang, J., Koch, D. L., Yin, X. (2011). Mass/heat transfer from a neutrally buoyant sphere in simple shear flow at finite Reynolds and Peclet numbers. AIChE Journal, 57(6), 1419-1433.

Zhong, W. Q., Zhang, Y., Jin, B. S., Zhang, M. Y. (2009). Discrete Element Method Simulation of Cylinder-Shaped Particle Flow in a Gas-Solid Fluidized Bed. Chemical engineering & technology, 32(3), 386-391.

Zhou, Z. Y., Pinson, D., Zou, R. P., Yu, A. B. (2011). Discrete particle simulation of gas fluidization of ellipsoidal particles. Chemical Engineering Science, 66(23), 6128-6145.

Zou, Q., He, X. (1997). On pressure and velocity boundary conditions for the lattice Boltzmann BGK model. Physics of fluids, 9(6), 1591-1598.

Curriculum Vitae

Personal information

Name   Yong Chen

Address   Leonhardstrasse 21, 8092 Zürich, Switzerland

Email   yonchen@student.ethz.ch

Education

2011-present   PhD candidate, Institute of Energy technology, ETH Zürich

2008-2011   Master of Engineering, Fluid Mechanics, Zhejiang University, China

2004-2008   Bachelor of Engineering, Mechanical Engineering, Huazhong University of Science and Technology, China

Journal Publications

Chen, Y., Third, J. R., Müller, C. R. (2015). A drag force correlation for approximately cubic particles constructed from identical spheres. Chemical Engineering Science, 123, 146-154. (Chapter 2)

Third, J. R., Chen, Y., Müller, C. R. (2016). Comparison between finite volume and lattice-Boltzmann method simulations of gas-fluidised beds: bed expansion and particle–fluid interaction force. Computational Particle Mechanics, 3(3), 373-381.

Papers in preparation

Chen, Y., Müller, C. R. The effect of solid volume fraction and Reynolds number on the drag force acting on assemblies of cubic particles. (Chapter 3)

Chen, Y., Müller, C. R. A Dirichlet boundary condition for thermal lattice Boltzmann method. (Chapter 4)

Chen, Y., Müller, C. R. Lattice Boltzmann simulation of gas-solid heat transfer in random assemblies of spheres: The effect of solids volume fraction on the average Nusselt number for $Re \leq 100$. (Chapter 5)

Chen, Y., Müller, C. R. Heat transfer to gas in random assemblies of cubes: the effect of solid volume fraction on the average Nusselt number for $Re \leq 100$. (Chapter 6)

Conference proceedings

Chen, Y., Third, J.R., Müller, C.R. Drag force correlations for non-spherical particles in gas solid flows, AIChE 2014 Annual Meeting, AICHE 2014 Annual

Meeting, November 16-21, 2014, Atlanta, GA, USA.

Chen, Y., Third, J.R., Müller, C.R. Drag force correlation for non-spherical particle assemblies in gas-solid flows, PARTEC 2013, April 23-25, 2013, Nuremberg, Germany.

Poster exhibitions

Chen, Y., Third, J.R., Müller, C.R. Drag force correlation for assemblies of non-spherical particles in gas-fluidized bed, AICHE 2013 Annual Meeting, November 3-8, 2013, San Francisco, CA, USA.

Lu, G., Chen, Y., Third, J.R., Müller, C.R. Multi-scale modelling of gas-solid reactors, ETH Industry Day 2013, September 12, 2013, Zurich, Switzerland.

Chen, Y., Third, J.R., Müller, C.R. Lattice Boltzmann simulation of gas-solid fluidized bed containing non-spherical particles, Fluidization XIV, May 26-31, 2013, Noordwijkerhout, The Netherlands.

Chen, Y., Third, J.R., Müller, C.R. Lattice Boltzmann method (LBM) simulations of gas-solid flows containing non-spherical particles, AIChE 2012 Annual Meeting, October 28 – November 2, 2012, Pittsburgh, PA, USA.

Lu, G., Chen, Y., Third, J.R., Müller, C.R. Multi-scale modeling of single- and two-phase particulate systems, ETH Industry Day 2012, September 7, 2012, Zurich, Switzerland.

Acknowledgements